A STATE ESTIMATION FRAMEWORK FOR ULTRASONIC STRUCTURAL HEALTH MONITORING OF FASTENER HOLE FATIGUE CRACKS

A Thesis
Presented to
The Academic Faculty

by

Adam Cobb

In Partial Fulfillment
of the Requirements for the Degree
Doctor of Philosophy in the
School of Electrical and Computer Engineering

Georgia Institute of Technology
April 2008

A STATE ESTIMATION FRAMEWORK FOR ULTRASONIC STRUCTURAL HEALTH MONITORING OF FASTENER HOLE FATIGUE CRACKS

Aprroved by:

Professor Jennifer E. Michaels,
Committee Chair
School of Electrical and Computer Engineering
Georgia Institute of Technology

Professor George Vachtsevanos
School of Electrical and Computer Engineering
Georgia Institute of Technology

Professor Thomas E. Michaels
School of Electrical and Computer Engineering
Georgia Institute of Technology

Professor Thomas G. Habetler
School of Electrical and Computer Engineering
Georgia Institute of Technology

Professor Laurence J. Jacobs
School of Civil and Environmental Engineering
Georgia Institute of Technology

Date Approved: 5 March 2008

To my parents, for their unyielding support, even when I called and said I was thinking about becoming a history major.

And to my wife, Anne, my love, my life, my best friend.

ACKNOWLEDGEMENTS

First and foremost I offer my sincerest gratitude to my advisor, Dr. Jennifer E. Michaels, who has supported me throughout my time at Georgia Tech. She provided not only a perfect research environment with her technical expertise and unyielding pursuit of knowledge, but also provided a genuinely personal experience. Any contributions made by me during the creation of this thesis can only be a reflection of her attention to detail and her personal involvement. Without her help, none of this would have been possible.

My most sincere thanks also go to Dr. Thomas E. Michaels, for not only his supreme technical understanding of the areas of NDE and SHM, but also a willingness to work through my ideas no matter how crazy they were. His instruction and coaching in the underlying physics of metal fatigue and wave propagation was instrumental in the development of this thesis. Further, his unrestricted support throughout the entire process was incredibly important to my thesis' development.

I also would like to thank the dissertation committee members, Dr. Laurence J. Jacobs, Dr. George Vachtsevanos, and Dr. Thomas G. Habetler. I cannot imagine the effort required in reviewing several years worth of work in such a short time period.

I would also like to express my appreciation to the faculty and personnel of the Georgia Institute of Technology, especially the School of Electrical and Computer Engineering, for providing the facilities necessary for all phases of my graduate education.

I also appreciate the support of the project for which my graduate studies were funded. My work was sponsored by the Defense Advanced Research Projects Agency (DARPA), Defense Sciences Office, ŞStructural Integrity Prognosis SystemŤ Program, contract No. HR0011-04-0003, to Northrop Grumman, Integrated Systems, and is approved for public release, unlimited distribution. Particular thanks goes to Dr. Bob Silberstein and Mr. Jerry

Nardiello for their support regarding the fatigue experimentation.

I would like to thank Dr. Joseph “Joebob” Havlicek at the University of Oklahoma. He taught me through his bearing and knowledge what it meant to be a professor and encouraged my application to graduate school. Without his help, I would never have taken this path in my life.

I also want to express my sincerest appreciation of the current and past members of the Quantitative Ultrasonic Evaluation, Sensing and Testing (QUEST) Laboratory at Georgia Tech. The members whose assistance was particularly valuable were Dr. Yinghui Lu, Mr. David Stobbe, and Mr. David Muir. Also, the two post-doctoral researchers involved with our group, Dr. Bao Mi and Dr. Pranaam Haldipur, were instrumental in everything related to my research.

Finally, I want to express my most profound appreciation of my friends and family. In particular, I want to thank my friends from IRC, Brian Lawson, Jason Brezinski, and Joe deMauro, for always keeping my head on straight. I would have never been able to attend Georgia Tech without both their support and prodding. Special commendation goes to my wife, Annette, who endured the rigors of my own education along with the demands of her own career. She is a saint who dealt with the worst of it while never failing to be there for me. She made the doctoral program bearable when it should not have been and enjoyable when it had no right to be.

There are many others that I would thank, whom without their support I would have been hard-pressed to persevere during my graduate studies. It is with supreme humility I recognize that this thesis is not solely my work, but the combined efforts of many individuals. I thank all of you from the bottom of my heart.

TABLE OF CONTENTS

LIST OF TABLES

LIST OF FIGURES

SUMMARY

The development of new monitoring systems is a critical research area because of the age and sustainment costs associated with many of the aircraft structures in use today. Specifically, integrated structural health monitoring (SHM) systems are advantageous because they allow for automated, near real-time feedback of the state of the structure, where the automation improves both the accuracy of the measurements and allows for more frequent system interrogation than possible with traditional nondestructive evaluation. Ultrasonic SHM is particularly suited for these *in situ* systems because of its potential to provide repeatable, robust, and relatively inexpensive detection of damage well before structural failure.

The research problem considered in this thesis is detection and tracking of fatigue cracks emanating from fastener holes in metallic structural components. The sensing method utilizes attached ultrasonic transducers, and tracking of damage is achieved by employing a state estimation framework that incorporates a well-known empirical model for crack growth and a model relating the ultrasonic response to crack size. The state estimation process is preceded by an automated crack detection algorithm, and can be followed by a prediction of remaining life assuming future usage. The state estimation framework provides a better estimate of crack size than either the ultrasonic measurement model or crack growth model alone. Although the example application is fastener hole fatigue, the general approach is applicable to a variety of SHM problems.

The principal contributions of the research presented in this thesis are the following:

- An automated method for detecting fatigue cracks emanating from fastener holes using permanently mounted ultrasonic sensors.

- An ultrasonic measurement model for both correlating received ultrasonic energy

changes to crack dimensions and quantifying the uncertainty of the resulting crack size estimates.

- Generation of probability of detection (POD) curves for *in situ* detection of fastener hole fatigue cracks.
- Formulation and implementation of a state estimation framework for near real-time estimation of fatigue crack sizes emanating from fastener holes and prediction of the remaining fatigue life.
- A generic framework for combining ultrasonic measurements and crack propagation models with state estimation, which can be applied to similar SHM problems.

CHAPTER 1

INTRODUCTION

1.1 Problem Description

The research problem considered in this thesis is *in situ* monitoring of fastener holes in metallic components for small fatigue cracks using ultrasonic methods. This problem is of interest because of several factors. First, fastener holes are a common source of critical cracks because the holes produce stress concentrations in metallic structures. Thus, often the most likely locations of crack initiation and growth are near fastener hole sites. Second, ultrasonic methods are suitable for interrogating holes from a distance, where the sensors themselves do not need to be inside the hole. Third, ultrasonic methods are sensitive to small cracks and can detect damage well before catastrophic failure.

The specific application of this research is aircraft structures because of the ever-increasing need for intelligent real-time monitoring of aerospace structural components. Current inspection approaches for aircraft structures are based on periodic inspection using traditional nondestructive evaluation (NDE) techniques. These inspections can require the disassembly of the structure, a difficult and time-consuming procedure. Structural health monitoring (SHM) approaches, where the monitoring system is integrated within the structure being inspected, have the capability to provide for frequent examination of critical components without disassembly, resulting in an improvement in the safety of the structure and the potential for a reduction in maintenance costs. As stated by Achenbach and Kulkarni [1], the purpose of an SHM system is to provide information about the state of a structure so that the integrity can be assessed at any time. Additionally, an SHM system provides the ability to interrogate portions of the structure that are either difficult or impossible to inspect without disassembly.

The support and technical focus of this research is provided by the Northrop Grumman Corporation and the Defense Advanced Research Projects Agency (DARPA), Defense Sciences Office, Structural Integrity Prognosis System (SIPS) program. As stated in [2] about the SIPS program,

> "The program objective is to design a system to provide prompt, informed predictions of the structural viability of individual assets based on tracking of their actual use and modeling of anticipated usage."

The prognosis system is founded on a collaboration between sensor systems, advanced reasoning methods for data fusion and signal interpretation, and modeling and simulation systems. The premise of the program is that combining the current knowledge of fatigue processes in the material with knowledge of the current state of an aircraft and an intelligent reasoning system will be of utility in providing a quantitative prediction of future vehicle viability.

The work presented in this thesis falls within the sensor thrust of the SIPS program, using *in situ* ultrasonic techniques to form accurate estimates of the current state of the structure. The long term goal would be to integrate the estimates from the SHM framework described by this thesis with the SIPS program computational models and reasoning systems to form a final prognosis system for the use of ultrasonics for SHM.

The type of material, fatigue process, and target geometries for monitoring were provided by the SIPS program. Additionally, a broad series of experiments were performed during the course of the project, with several transducer configurations and fastener hole geometries. The experiments ranged from simple 2-hole coupon tests to full aircraft wing tests with several holes monitored. Only a subset of these experiments are reported in this thesis.

1.2 SHM Approach Overview

The SHM framework presented here provides as output a real-time estimate of the degree of damage near fastener holes. The approach is to divide the problem into modular elements that can be updated or replaced individually, with each of the modules developed to address specific aspects of fastener hole monitoring. This modular approach ensures that the presented framework can be readily modified for different SHM applications that may incorporate different senors and structural geometries.

The approach is divided into three modules based on the severity of the fatigue damage. As shown in Figure 1, initially the specimen has no detectible damage using the ultrasonic measurement method, necessitating the use of a detection strategy. The approach for defect detection is a trend analysis relating an energy-based feature of the ultrasonic waveforms to the presence of fatigue damage. This empirically derived process can be performed automatically in real-time after each ultrasonic measurement.

After defect detection, the SHM framework tracks the fatigue damage as it grows during the fatigue process. A state estimation approach is utilized to update the degree of damage after each ultrasonic measurement. The approach integrates a measurement model with a model of the fatigue damage propagation so that the estimate of damage incorporates both the measurement and the expected damage growth.

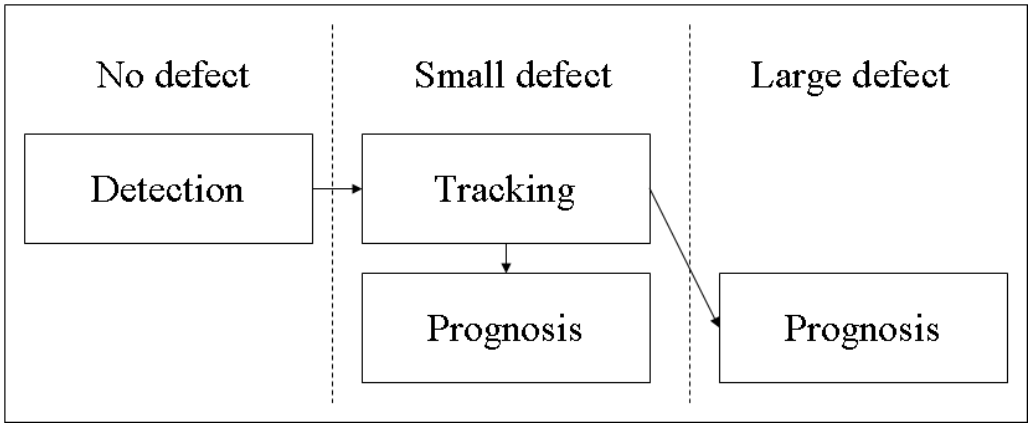

Figure 1: Overview of the implementation approach for the SHM framework

An ultrasonic measurement model is developed for quantifying the effect of different crack geometries on the same energy-based feature. A Monte Carlo method captures the wave propagation statistics for the ultrasonic energy density between the two transducers. An estimate of the energy-based feature as a function of crack dimensions is generated using a second Monte Carlo process; this function serves as the measurement model for state estimation. Additionally, probability of detection (POD) curves are created from the statistics of the Monte Carlo processes.

The system evolution model is based on established fracture mechanics theory for fatigue growth of macrocracks. The crack growth relationship developed by Paris relates material constants to the stress intensity to calculate the expected crack growth rate [3]. Additionally, a statistical treatment of Paris's crack growth equation approximates the statistical variations between fatigue experiments. Not considered in this study is the initiation and growth of microcracks as this regime is not detectible with the employed ultrasonic sensing methodology.

In parallel to defect tracking, the SHM framework can also provide an estimate of the remaining fatigue life of the structure. This prognosis uses the state estimation output and an assumed fatigue usage to provide a probability density function (pdf) of the remaining cycles until failure. As with the state estimation-based tracking, a new prognosis estimate can be provided after each additional ultrasonic measurement.

Finally, there is a physical limit to the maximum defect size the ultrasonic measurements can characterize effectively. Once a crack grows beyond a saturation limit, it is not possible to reliably quantify the relative crack growth using the described approach. As such, once the defect size exceeds this limit, the ultrasonic measurements are no longer useful and final estimates of the expected crack growth and remaining fatigue life are generated. This prognosis is the final output of the SHM framework.

1.3 Principal Contributions

The principal contributions of the research presented in this thesis are the following:

- An automated method for detecting fatigue cracks emanating from fastener holes using permanently mounted ultrasonic sensors.
- An ultrasonic measurement model for both correlating received ultrasonic energy changes to crack dimensions and quantifying the uncertainty of the resulting crack size estimates.
- Generation of POD curves for *in situ* detection of fastener hole fatigue cracks.
- Formulation and implementation of a state estimation framework for near real-time estimation of fatigue crack sizes emanating from fastener holes and prediction of the remaining fatigue life.
- A generic framework for combining ultrasonic measurements and crack propagation models with state estimation, which can be applied to similar SHM problems.

1.4 Organization of the Thesis

There are four parts of this thesis, as summarized in Figure 2. The first part, comprising Chapters 1 - 3, covers the introduction of the problem of fastener hole fatigue cracks and a broad outline of the presented methodology. A brief history of SHM for aircraft, including a description of related ultrasonic techniques, is presented in Chapter 2. The experimental approach for generating fatigue cracks and the ultrasonic sensing methodology employed are given in Chapter 3.

The second part of the thesis, given in Chapter 4, summarizes the detection strategy for monitoring fastener holes for the presence of damage. A filter bank approach is discussed for early crack detection along with an automated crack detection algorithm. Experimental results are provided for this technique.

The third part of the thesis, presented in Chapters 5 - 7, discusses defect tracking and prognosis. Chapter 5 outlines the state estimation framework, Chapter 6 develops the model for relating ultrasonic measurements to crack dimensions, and Chapter 7 discusses the crack propagation model. In addition, Chapter 7 describes the approach for damage prognosis, which is based upon the crack propagation model.

The fourth and final part of the thesis is contained in Chapters 8 - 9, where the results from the SHM framework are presented along with conclusions and recommendations for future work.

Appendix A provides a summary of all completed and pending work generated during the creation of this thesis.

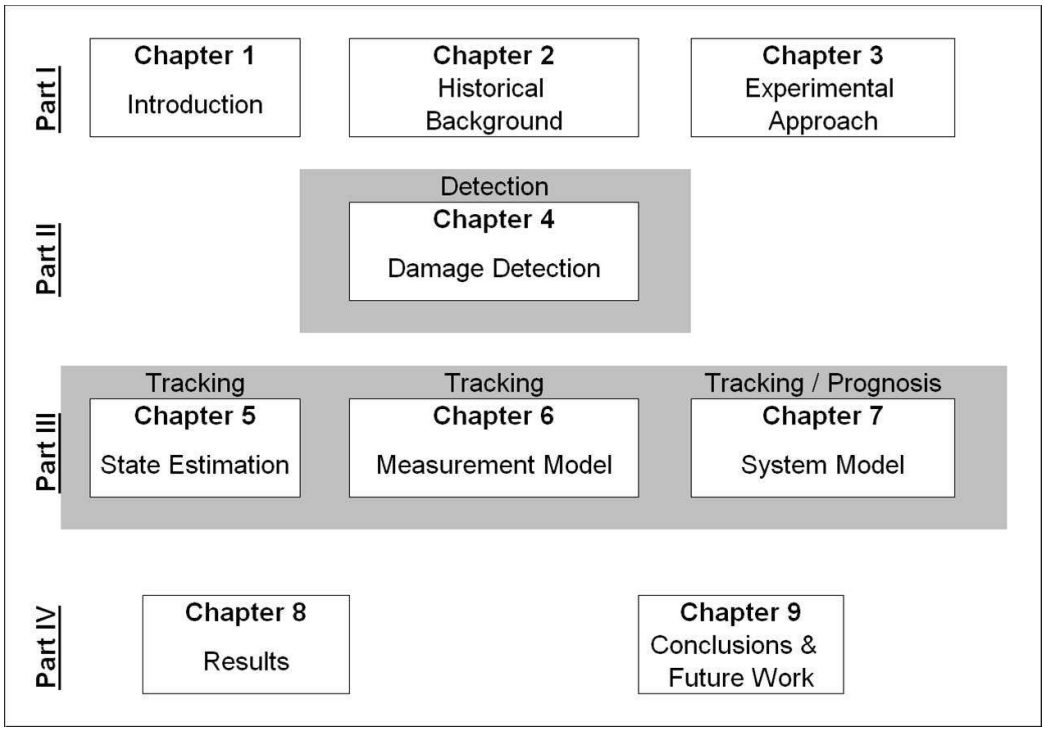

Figure 2: Organization of thesis

CHAPTER 2

BACKGROUND

2.1 Scope and Objective of the Chapter

The purpose of this chapter is to provide a brief overview of the technical topics utilized during the development of this thesis. This multidisciplinary subject can be roughly divided into four areas: structural health monitoring, ultrasonics, signal processing, and statistical life prediction.

Section 2.2 outlines the background and motivation for employing SHM. In particular, the common aspects of any SHM system are discussed, where these aspects are used in the development of the SHM framework outlined in this thesis. Motivating examples are provided that are related to aircraft structures.

Section 2.3 provides a brief outline of the use of ultrasonics for material characterization and defect sensing. Particular attention is given to surface wave and bulk wave sensing of cracks as these two approaches are utilized here.

Section 2.4 of this chapter describes the signal processing practices related to ultrasonic data analysis, focusing on basic signal processing, time-frequency representations and data fusion techniques

Finally, Section 2.5 summarizes statistical life prediction. Rather than using a strictly measurement-based approach, statistical approaches involving damage propagation statistics are described. The statistical methodologies outlined are current state-of-the-art for aircraft life estimation.

2.2 Importance of SHM

SHM is an emerging field with contributions from a broad range of disciplines, such as electrical, mechanical, aerospace, and civil engineering, physics, and material science. SHM can be thought of as an extension of the well established field of NDE, where the goal for both methodologies is to estimate a characteristic of the material being interrogated, such as the presence of corrosion or fatigue cracking, without damaging the structure. The key difference between SHM and NDE is that the monitoring system utilized with SHM is integrated in the structure. Because of this sensor integration, real-time interrogation during structural use is possible, taking advantage of the time history of the sensor responses. This integration provides the ability to "track" damage progression. Also, SHM systems provide the capability to monitor areas within the structure that are difficult or impossible to inspect with traditional NDE without structure disassembly. Several recent books have been published related to SHM [4, 5] and several international conferences meet regularly, most notably the International Workshop on Structural Health Monitoring and the European Workshop on Structural Health Monitoring. These books and conferences are a reflection of the growing importance on-line sensing of the state of structures.

The specific application of this research is monitoring fastener holes in aircraft structures using an SHM framework, as discussed in Section 1.1. SHM systems integrate sensors attached to or embedded in the structure to provide real-time estimates of the state of the structure. The most obvious potential advantage of utilizing SHM is an improvement in the safety of the structure; more frequent monitoring of critical areas compared to traditional NDE approaches increases the likelihood of detecting damage before catastrophic failures occur. More and more, airframes are utilized beyond their originally intended life span and take on new mission profiles, requiring more frequent inspections of the structural components to maintain integrity. In addition to the safety considerations of SHM, the cost savings possible with automated sensing between maintenance cycles are another important potential contribution. Approximately 60% of the total life costs associated with

an airframe are used for sustainment, where these costs increase with the age of the aircraft [6]. Further, the costs associated with unscheduled maintenance are one the largest maintenance costs possible for an aircraft in terms of both man-hours and lack of availability. Ascertaining problem areas before they become critical allows for the aircraft to be serviced at a planned date, phased into the flight schedule of the aircraft. Earlier repairs also tend to be less extensive and expensive, further reducing the cost for the sustainment of the system [6].

The requirements for an SHM system are detailed by Achenbach and Kulkarni [1]. The authors state that the four "absolute requirements for any SHM system" are as follows:

1. Simple but accurate sensors.
2. Incorporation of the mechanisms for the progression of damage being detected.
3. Clear correlation between damage detected and the response from the sensors.
4. Statistical methods employed given that the data is not deterministic in nature.

An SHM system can be either global, which estimates the overall state of large portions of the structure, or local, which monitors critical areas within a structure. There is a trade-off between global and local SHM, where local SHM provides higher accuracy of damage detection in a small area, but is unable to characterize damage outside its small region of interest. Local SHM is advantageous because in many cases, it is known *a priori* where the damage is most likely to occur, defining structural hot spots that local SHM can exploit.

2.3 Ultrasonic Sensing

Ultrasonics is one of the most widely utilized sensing methodologies because of the relative simplicity of the sensors combined with the ability of the energy to propagate long distances into the interior of structures while maintaining sensitivity to defects [7]. The

basic ultrasonic sensing approach was developed during the 1940s and remains largely unchanged today beyond improvements in transducer fabrication, analysis procedures, and electronic components [7].

The basic ultrasonic testing scenario involves generating repetitive bursts of elastic wave energy that propagate into a part. The frequency can range from 50 kHz to even hundreds of megahertz, where most applications are confined to 1 - 10 MHz [7]. The frequency range employed directly relates to the desired detectible flaw size by the wavelength interaction relationship. The energy propagated interacts with the structure, and is received in either a pulse-echo (same transducer for transmission and reception) or a through-transmission (two transducers for transmission and reception) configuration, where the received wave shapes are examined. The transducers themselves are generally manufactured using piezoelectrics to generate a mechanical wave given an input voltage, but there are a variety other approaches.

Ultrasonic methods can be based upon either bulk waves or guided waves depending upon the specimen geometry and expected flaw locations. Bulk wave methods utilize waves propagating in the bulk material where there are few interactions with boundaries, whereas guided waves rely upon specimen boundaries for propagation. Surface waves, a form of guided wave, travel along a single free surface, and are the guided waves of interest for the work described here.

2.3.1 Bulk Waves

Ultrasonic bulk waves propagate in the bulk of the material as either longitudinal or shear waves with limited interaction with the surfaces of the material [8]. Longitudinal waves occur when the direction of particle motion is parallel to the direction of wave motion. On the other hand, for shear waves, the direction of wave propagation is perpendicular to the direction of particle motion. Further, shear waves can be polarized in any angle orthogonal to the direction of wave motion. For the case of a shear wave propagating

relative to a free surface, polarizations are referred to as shear vertical (SV) and shear horizontal (SH). SH waves have particle motion parallel to the boundary, and SV waves are polarized perpendicular to the SH waves. Regardless of polarization, the wavespeed of the longitudinal wave is always greater than the wavespeed of the shear wave, with

$$c_L = \sqrt{\frac{2\lambda + \mu}{\rho}}, \tag{1}$$

$$c_T = \sqrt{\frac{\mu}{\rho}}, \tag{2}$$

where λ and μ are Lamé constants, ρ is the material density, and c_L and c_T are the longitudinal and shear wavespeeds, respectively.

2.3.2 Surface Waves

As opposed to bulk waves, surface waves occur when the energy propagates along a structural boundary, or interface, because of interference patterns developing from body waves [8]. The result is that the interface acts as a waveguide. All surface waves share common features based on the concentration of the wave motion near the surface of propagation. Surface waves travel in a limited portion of the material confined to the vicinity of the interface; all surface waves have an exponential decay in the energy away from the interface of propagation based on the frequency of the wave.

A variety of surface waves exist depending on the nature of the propagation surface, such as Stoneley waves (the surface is the interface between two semi-solids) and Love waves (the surface is the interface between thin layer and a semi-infinite solid) [8]. The most commonly discussed surface wave and the one of interest in this study, however, is a Rayleigh wave, which is a surface wave that propagates along a solid surface in a vacuum of which air is a good approximation. The governing equation of the Rayleigh wave is given by the Rayleigh-Lamb equation,

$$(c_R/c_T)^6 - 8(c_R/c_T)^4 + 8(3 - 2(c_T/c_L)^2)(c_R/c_T)^2 - 16(1 - (c_R/c_T)^2) = 0, \tag{3}$$

where c_R, c_T, and c_L are the wavespeeds for the Rayleigh, shear and longitudinal waves, respectively. The Rayleigh wavespeed, combined with the relationship between frequency and velocity, defines the rate of energy decay away from the propagation surface. Also, since the energy is not being lost in the bulk material, Rayleigh waves are able to propagate very long distances compared to bulk waves [9].

2.3.3 Sensing Applications

There are numerous NDE and SHM examples of using both surface and bulk waves to inspect a structure for the presence of defects. Provided here are examples related to the ultrasonic sensing method described in this thesis, where these examples are not intended to be a comprehensive review of using ultrasonics for flaw detection and characterization. Each of these examples demonstrates an important challenge or approach for monitoring fastener holes. The first two examples demonstrate the use of bulk waves mode converting into surface waves for localizing and sizing defects. The third example illustrates the effect of the depth of a defect for inspection with Rayleigh waves. The fourth and fifth examples describe the advantages of using load modulation for accentuating surface wave inspection. The sixth and final example examines the effect of ultrasonic frequency on ultrasonic defect detection and sizing in combination with load effects. For a broad overview of using ultrasonics for NDE applications, refer to [7] and [9].

Nagy et al. consider the problem of inspecting fuel weep holes [10]. These circular holes are larger than traditional aircraft fastener joints, but several analogies can be made between weep hole inspection and fastener hole monitoring. For this weep hole problem, ultrasonic energy is propagated into the bulk of the material. The energy is aimed at the edge of the weep hole and the interface interaction produces a pseudo-Rayleigh wave that propagates along the surface of the hole. This wave is not a classical Rayleigh wave because it is propagating around a cylindrical surface instead of a flat surface. Without cracking, the energy propagates around the hole and re-radiates back to the receive transducer as

bulk waves, which is aligned to receive energy from the opposite side of the weep hole. The cracks that form along the surface of the weep hole block this energy, and also produce a reflection that re-radiates back to original transmitting transducer. This bulk wave configuration, combined with signal processing, allows for accurate determination of the presence and location of defects.

An ultrasonic inspection technique for characterizing embedded cracks in steel is described by Baby et al. [11]. They focus on detecting vertical cracks with shear wave ultrasonics using the times of arrivals to characterize the crack length. This approach is an NDE technique in that the angle beam transducer is articulated so that it is focused on the top of the crack, maximizing the recorded energy arrival. The method to determine the crack length depends on the mode conversion of the input shear wave along the crack surface. A portion of the energy from the incident shear wave is diffracted back from the crack tip to the transducer, producing the initial arrival. At the same time, a portion of the remaining energy is mode converted along the crack interface into a surface wave that travels along the length of the crack. Once the energy returns to the top of the crack, some of the energy is reconverted into a shear wave that propagates back to the transducer, producing a second arrival. The difference in time of the two arrivals is directly related to the crack length given the known wave speeds. The limitation of this technique is it depends on the orientation of the defect. Without a near-vertical defect, the positioning of the transducer is more difficult given the much reduced signal arrival amplitudes.

An experimental study of the inspection of surface breaking cracking is given by Yew et al. [12]. For this study, a 3 cm thick aluminum plate is inspected using Rayleigh waves. A notch of varying depths is cut on one side of the plate to simulate a crack. The method of generating the Rayleigh wave is to drop a metal ball onto the 3 cm width plate edge on one side of the notch and record the resulting waveform with a transducer located on the opposite side of notch. When the notch is not present, the shear, longitudinal and Rayleigh wave components propagate directly to the receive transducer. As the notch is lengthened

past the wavelength of the Rayleigh wave, however, the surface wave energy is blocked. For surface wave energy to reach the receive transducer, the longitudinal and shear waves must diffract from the notch tip. The shear and longitudinal waves incident on the notch tip are diffracted back to the surface of the specimen and this energy is mode converted into Rayleigh waves at the surface. For very small notches, where the depth is below the Rayleigh wavelength, there is a rapid decrease in received surface wave energy as the depth is increased. Beyond this small depth change, however, almost the entirety of the original Rayleigh wave is reflected back, leaving the crack tip refraction as the only method for generating the surface wave.

A ultrasonic technique is documented by Yan and Nagy [13] and Kim et al. [14, 15], where a surface wave is used to track fatigue crack growth from known points of likely crack formation. Both approaches use pulse-echo surface wave techniques, where a transducer excites ultrasonic energy that propagates along the sample surface, and the energy reflects back to the transducer from the crack. Each technique attempts to examine the crack opening effects; without loading, the residual stresses around fatigue cracks compress the crack faces, allowing the ultrasonic energy to be largely unaffected by the defect. The lack of ultrasonic interaction results in the unopened cracks being almost transparent to ultrasonic waves [14]. The approach used by Kim et al. is to externally apply loading, thus opening the crack for ultrasonic inspection [14]. The approach by Yan and Nagy is to augment the surface wave inspection by laser-based thermal excitation to modulate the opening and closing of fatigue cracks [13]. This approach is unique in that a laser is used to input thermal energy around the crack, improving the capabilities of surface wave techniques to detect fatigue cracks. For both cases, once the crack opening is modulated, changes in the ultrasonic arrival amplitudes are used to quantify the presence of damage.

Another surface wave technique is detailed by Harri [16], where a through-transmission configuration of transducers is mounted on the surface of a smooth aluminum sample. The uniqueness of this approach is the excitation of the transmitter. Instead of a simple tone

burst of one frequency or a spike excitation of all frequencies, the researchers use a "multi-sine" approach, where sine waves of all integer multiples of MHz frequencies between 1 and 10 MHz are added. The transducers are continuously excited during the fatigue process. The received waveforms are filtered to isolate individual frequency components, and the variability of measured amplitudes is computed. Since the sample is interrogated during the fatigue process, the waveforms are taken when the crack is both open and closed. As such, when there is no crack, the variability of the amplitudes recorded is small, whereas when a crack is present, the variability will increase as a function of crack size. The size of the crack is further characterized through the use of different frequency components, with the higher frequencies more sensitive to smaller cracks, but becoming saturated as the cracks grow.

2.4 Signal Processing Techniques Related to Ultrasonic Sensing

The analysis of ultrasonic waveforms, as with most signal processing approaches, focuses on creating some feature or combination of features that are useful for determining a characteristic of the material being interrogated. Signal analysis is key to ensuring that the best available information of the ultrasonic waveform is employed for determining the state of the structure. For example, the information extracted from waveforms such as energies and arrival times is often directly related to the presence and degree of damage within the structure.

An important consideration for the development of signal processing algorithms is to ensure that the analysis relates to actual physical processes within the structure. Without an understanding of the underlying physical significance of features being calculated, the ability for the associated methodology to work with real world problems will be severely limited. In other words, to quantify the damage accumulation within a component, it is necessary that there be a physically meaningful connection between the damage and computed features [1].

A broad overview of techniques related to the ultrasonic signal processing performed in this thesis are discussed. These are basic techniques, split-spectrum processing, time-frequency analysis and data fusion approaches.

2.4.1 Basic Ultrasonic Signal Processing

Conventional signal processing approaches for ultrasonic sensing relate simple features of the waveforms, such as amplitude, energy, and time of arrival, to damage or material properties. The elegance of these waveform features is in the relative simplicity of relating the feature to some aspect of the material interrogated, such as defect size or location. The direct correspondence between the signal processing and the quantity of interest allows for a relatively straight forward evaluation of their efficacy and subsequent acceptance by the NDE and SHM communities.

One common ultrasonic NDE approach involves maximizing the pulse-echo amplitude response from a defect. Using the received time and amplitude, combined with calibration curves for the material being inspected, an estimated defect size and location can be estimated [17]. An alternative method is to use only the time of arrival of various echoes from a defect. These approaches, known collectively as time-of-flight methods, relate crack sizes to the time taken for the wave to travel around a defect [18, 19]. The sizing and localization capabilities of these approaches, however, is limited to defect sizes on the order of the ultrasonic wavelength. Lee and Tsuda [20] present a surface wave monitoring method using piezoelectric fiber wave guides placed at varying distances from a fastener hole surface for sizing surface breaking defects. This ultrasonic approach, as described by Lee and Tsuda, monitors the wave guides to determine if they are broken by a growing surface crack. Nagy et al. [10], as discussed previously, consider the problem of defect detection of cracks originating from weep holes in fuel tanks using circumferential surface waves generated by an incident shear wave. Their approach is to localize and size the defects using both the received amplitude and the time of the arrivals, providing defect localization and sizing.

2.4.2 Split-Spectrum Processing

A classical technique for ultrasonic waveform processing is called split-spectrum processing (SSP). The technique is based on the physical interactions of the ultrasonic waves and scatterers within the structure [21]. The basis of SSP is that there is grain noise that affects the received ultrasonic waveforms both spatially and in frequency. The SSP method considers the frequency dependence of the received signals to discriminate defect echoes from grain noise.

The received ultrasonic waveform, $x(t)$, can be divided into two parts,

$$x(t) = w(t) + d(t), \tag{4}$$

where $w(t)$ is the signal from the coherent grain noise scatterers and $d(t)$ represents the arrivals from the defects. For SSP, $x(t)$ is split into N separate waveforms through filtering, as shown in Figure 3. The filters are generally narrow band with uniform bandwidth and overlap. The filtered waveforms are

$$x_n(t) = w_n(t) + d_n(t), \tag{5}$$

with $n \in [1, ..., N]$. The narrow band grain noise waveforms, $w_n(t)$, have spatially and spectrally variable properties because of the random nature of the scatters. On the other hand, the wide band defect signals, $d_n(t)$, contain some invariable properties since they

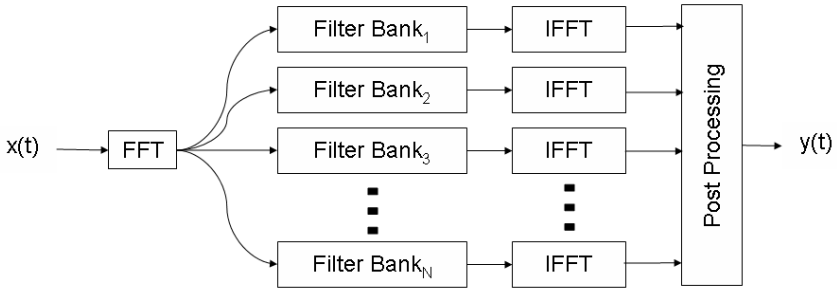

Figure 3: Split-Spectrum Processing.

come from the same defect within the sample [22]. This difference is accentuated with post processing techniques, where a variety of options exist, such as absolute minimization [23, 24], polarity thresholding [23] and variable bandwidth processing [25, 26].

One such post-processing approach is to minimize the split signals, $x_n(t)$, to remove features that are not common to all of the signals [23, 24]. At each timestep t, the minimum amplitude of each of the $|x_n(t)|$ waveforms is determined, with the sign determined from that of the selected $x_n(t)$. Algorithmically, this is defined as

$$y(t) = \text{sign}(x_i(t)) \cdot \min_n(|x_n(t)|), \quad \text{where} \quad i = \text{argmin}_n(|x_n(t)|). \tag{6}$$

The minimization allows for improved defect detection because the grain noise contained in $w_n(t)$ varies as a function frequency [23]. The $d_n(t)$ defect signals are generally invariant across frequencies, meaning the echo is visible at all frequency ranges in question. The result is that $y(t)$ is small when only grain noise is present while becoming large when a defect signal is present.

For the implementation of traditional SSP, the determination of the filters requires *a priori* knowledge of the transmitted ultrasonic energy. In [25, 26], Cudel et al. propose a modification to the filtering strategy for the SSP. First, they propose to automatically select the bandwidth based on the upper and lower frequency regions from a smoothed reference waveform. A more significant modification of conventional SSP is the use of variable bandwidth filters. Similar to SSP, their approach divides waveforms into equal bandwidth subsections of spectrum of spectral width B. Each subsection is then processed with conventional SSP with N filters, producing a $y_i(t)$ minimization result for that subsection. The results from each subsection are combined as

$$z(t) = \max(y_1(t), y_2(t), ..., y_M(t)), \tag{7}$$

where M is the number of B width subsections. The determination of B and N is generally trial-and-error. Their approach is essentially a two-stage SSP technique, providing superior defect echo resolution compared to classical SSP for the cases they considered.

2.4.3 Time-Frequency Representations

Various time-frequency analysis techniques, such as the short time Fourier transform, wavelet decomposition, and system modeling, have been used to characterize defects from ultrasonic waveforms. SSP, as described earlier, takes advantage of the characteristics of the grain noise to isolate echoes from defects. Because of its implementation, however, it is not possible to easily identify time-frequency dependence in the waveforms. The variable nature of the flaw dimensions and location, however, suggests the use of these time-frequency relationships for determining more information about the characteristics of the flaws.

The classical Fourier transform,

$$X_{FT}(\omega) = \int_{-\infty}^{\infty} x(\tau) e^{-j\omega\tau} d\tau, \tag{8}$$

allows for the transformation of a time waveform, $x(t)$, to an equivalent representation in the frequency domain. This transform, however, does not allow for determining the time dependence of the frequency information directly. In response to this limitation, the short time Fourier transform (STFT) is used. The STFT is a time dependent modification of the classical Fourier transform. The processed signal, $x(t)$, is windowed such that it is possible to localize the time dependence of the frequency information. Algorithmically, the STFT is

$$X_{STFT}(\omega, t) = \int_{-\infty}^{\infty} w(\tau - t) x(\tau) e^{-j\omega\tau} d\tau, \tag{9}$$

where $w(t)$ is an appropriate window function such as a Hamming window or a simple "boxcar" function, and the Fourier transform is repeated sequentially over equal duration time windows. The resulting function, $X_{STFT}(\omega, t)$, allows for identifying time-frequency dependencies within the processed signal. The choice of the windowing determines the resolution in both time and frequency, where it is not possible to simultaneously increase the resolution in both domains. Further, the window function is identical for both lower and higher frequencies, resulting in the time-frequency resolution remaining constant.

To overcome the limitations of fixed resolution, a generalization of the Fourier analysis known as the wavelet transform is used [27]. The original Fourier transform, $X_{FT}(\omega)$, is the projection of the signal onto a set of infinite duration, orthonormal basis functions, $e^{-j\omega t}$. The wavelet transform employs a different set of basis functions in the form of a mother wavelet that is scaled and shifted, allowing for time-frequency localization. The wavelet is a finite time-frequency pulse. This localization is given by the wavelet transform

$$X_{WT}(t,\omega) = \int_{-\infty}^{\infty} x(\tau) g\left(\frac{\tau - t}{\omega}\right) d\tau, \tag{10}$$

where $g(t)$ is the wavelet. The time-frequency properties can be better characterized than with the STFT since as ω increases, the wavelet projection is scaled to be narrower in time and higher and frequency. This transform is known as the continuous wavelet transform (CWT) and allows a continuous sampling of the time-frequency plane.

The application of wavelet analysis to ultrasonics has been documented in the literature as a successful technique for flaw identification. These wavelet-based approaches are given as alternatives to existing techniques, such as SSP. Several authors demonstrate the use of the standard discrete wavelet transform (DWT), which is a discrete version of the CWT, for denoising techniques [27, 28, 29]. As an example of denoising, Oruklu et al. document the use of the DWT for flaw arrival detection in noisy signals [29]. The authors note that for their experiments, the higher frequency information has very little information pertaining to the flaw arrivals, while the lower frequency information produces a low-pass filtered version of the flaw signals. The middle frequencies contain the dominate flaw information. The proposed approach is to create "windows" in frequency using the DWT and reconstruct the signal from this windowed set. The reconstruction is accomplished by picking the wavelet scales that best capture the flaw arrival information and setting the remainder of the frequency information to zero, then using the associated inverse wavelet transform to create a cleaner version of the original signal. It is shown that even with a negative signal-to-noise-ratio (SNR) (-0.1 dB to -4.2 dB SNR for the original waveforms), it is possible to

reconstruct the signals with an average improvement of over 8 dB, peaking at a 10.5 dB improvement. These studies demonstrate the viability of using reduced frequency content to produce ultrasonic waveforms for analysis. Further, these applications attempt to capture the relevant information pertaining to flaws, thus optimizing defect detection.

Bettayeb et al. [30] document the use of wavelet decomposition for resolving flaw signals in the presence of noise. A wavelet decomposition is similar to the wavelet transform. The difference between the DWT and a wavelet decomposition is the decomposition methodology filters both the low- and high-pass results of each filtering step, allowing for variable resolution at every frequency level. In [30], the authors implement a wavelet decompositions in an effort to reduce the noise present within the received ultrasonic signals. The signals are decomposed to three scale levels and reconstructed from the eight coefficients. The effect of this decomposition and reconstruction is the removal of the majority of the undesired noise, resulting in a reported improvement in SNR of 6-11 dB. As with the techniques discussed in [27, 28, 29], this approach demonstrates the usability of time-frequency approaches for improving signal quality by reconstructing the waveforms after removing the portions that contain mostly noise.

Related to the time-frequency approaches is the use of system models to ultrasonically determine the presence of damage within a structure. These models, while not employing the Fourier or wavelet approaches discussed above, attempt to capture the dynamics of the system in the form of an FIR or IIR filter. For the IIR case, the resulting model is generally in the form of an autoregressive-moving average (ARMA) filter,

$$F(z) = \frac{b_0 + b_1 z^{-1} + ... + b_M z^{-M}}{a_0 + a_1 z^{-1} + ...a_N z^{-N}}, \tag{11}$$

where M and N define the number of zeroes and poles of the system, respectively, and the coefficients a_i and b_i define their locations. The generalized approach for determining these parameters are numerous, such as the Padé approximation, the Prony method, and the Yule-Walker equations [31]. Regardless of the method used, however, the resulting models strive to both efficiently represent the system dynamics and use computationally efficient

procedures for deriving the parameters [31].

An example of using a system modeling approach for ultrasonic waveform analysis is given by Lynch, where the objective is to detect structural cracking using piezoelectric sensors [32]. For his approach, two piezoelectric transducers in a through-transmission configuration are mounted on either end of a thin aluminum plate and white noise is used to excite a response in the specimen. The resulting received waveform is fit to an ARMA model with $M = 4$ and $N = 21$, where these values were found experimentally to capture the system dynamics. The method for determining the damage within the structure is to track the location of the poles of the system, given by the polynomial $a_0 + a_1 z^{-1} + ...a_N z^{-N}$ of the model. Since a random process is used as the excitation function, several waveforms are recorded before and after a notch is cut into the specimen and the resulting models' poles are examined statistically. It is found that the centroids of the poles shift as a function of the degree of damage. Further, the shifts are more pronounced for larger defects, giving an indication of not only the presence of damage, but also the degree. The movement of these poles directly relates to the frequency content of the ultrasonic waveforms, and has been shown to correlate to changes in the plate's stiffness and damping.

2.4.4 Data Fusion Techniques

The preceding techniques of SSP and time-frequency representations dealt with waveform enhancement, noise removal and arrival characterization; there was limited discussion on attempting to correlate characteristics of the waveforms to the presence of damage within the specimen. Additional processing techniques, many times related to the signal enhancement techniques based on time-frequency representations, are used to produce signal features for correlation with the presence and degree of damage. There is frequently no known single feature for flaw characterization, necessitating the use of data fusion techniques such as voting schemes, neural networks, and support vector machines to produce a "fused" indicator of damage.

Voting schemes are one of the simplest data fusion strategies available for combining multiple features. The overall goal is to combine these features for classifying a system as a member of one of two or more classes. Each feature casts a "vote" and if a certain percentage of the votes agree, the system is classified as being a member of the agreed upon class. The logic behind a voting scheme is that there is always the possibility of false classification, but the likelihood is reduced by ensuring that a certain percentage of the features agree. For example, Lu and Michaels used a two-stage voting scheme to discriminate damage from surface variations using features from ultrasonic reverberating guided waves [33].

Another data fusion strategy is the use of artificial neural networks (ANNs) for feature-based classification. ANNs, as the name implies, are an attempt to reproduce the biological process of neural networks in organisms. ANNs are a software tool designed to estimate relationships in data through a series of weighted combinations of the input features. The weights are determined from a variety of learning algorithms, where a set of "training" data with known system states is used to determine the weights. Of particular note is that different ANNs can be created using the same training data; an ANN is not the optimal solution, but a possible solution for classifying a system based on the training features. The resulting ANN is essentially a mapping, or a function, relating raw data to a state of the system (e.g., presence, location or size of a flaw).

An example of using an ANN for ultrasonic waveform classification is given by Michaels et al. [34]. For this study, diffuse ultrasonic signals are received from sensors mounted on a rectangular aluminum sample. The waveforms are captured in the presence of both environmental and structural changes, where the intent is to determine the presence of structural changes in the presence of environmental conditions. A single-layer ANN is used with multiple features as inputs to address the problem of determining if a structural change has actually occurred. Results show that an ANN is reasonably successful in discriminating between environmental and structural changes. Furthermore, a classifier developed for one

particular structure was successfully applied to a second structure.

The use of support vector machines in conjunction with the time-frequency approaches is a well documented approach for SHM applications [35, 36]. At the most basic level, a support vector machine (SVM) is a machine learning tool that attempts to map features onto a higher dimensional plane for classification. Once the mapping is complete, which involves the use of a kernel function, a linear separator is calculated that optimally divides the feature space for classification. The optimality of this linear separator is important, as it implies that the SVM developed from the original data will be best able to generalize for classification of new data. This linear separator is subsequently transformed back to the original feature space through the associated inverse functions, completing the classification process. A more complete description of kernel learning methods can be found in [37], where the specifics of how the linear separator is determined and the associated kernel function are described.

The use of SVMs for feature-based damage detection and characterization methods is documented by several authors [35, 36]. Hagiwara and Mita [35] use SVMs and modal frequencies to characterize fatigue damage within a 5-story building. The feature vectors chosen are derived from the natural frequencies of each floor, where there is a feature vector for each of the floors. A polynomial-kernel based SVM is developed for every floor and each SVM acts as a classifier for the presence of damage on that individual floor. A similar approach is employed by Worden and Lane [36], where the Fourier transform of vibration information recorded from a ball bearing rotating under differing states of damage is input into a SVM [36]. A nonlinear, radial basis function is used for the kernel to best separate the data. For both cases, the SVMs were developed using simulated data first, then applied to experimental data. In both scenarios, the SVMs were able to differentiate between the different types of damage. Further, in [35], the SVMs trained on the assumption of a single floor exhibiting damage were able to generalize to the more complex situation of more than one floor damaged. This generalization ability, a result from the optimality

conditions imposed, is one of the most important advantages of SVMs over other data fusion techniques such as ANNs.

Another fusion-based example is found in [38], where Case and Waag described a many feature-based approach for defect detection. A series of ultrasonic pulse-echo waveforms are obtained from regions of a pipe near welds, including weld roots and counter-bores with and without flaws. Their approach considered 69 time and frequency domain features of ultrasonic waveforms for damage detection of weld joints in pipes. Unlike the previously described approaches, where the feature vector is comprised of related features of the waveform such as natural frequency shifts, this technique demonstrates considers wholly different features of the ultrasonic data to determine the presence of damage. The database of features considered are a variety of signal parameters, such as measured bandwidth, the variance of the normalized power spectrum, and the mean of the input signal. These features of the training data set were reduced to a maximum of 10 features using a *k*-nearest neighbor classifier to separate the different waveforms into defect and non-defect classes. Once perfect classification was reached using the *k*-nearest neighbor approach for the training set, the resulting feature set was used to evaluate a set of new waveforms. Using this approach, it was possible for the authors to differentiate accurately between defect and no defect cases with a success rate of approximately 85%. The authors noted, however, that the performance of the approach was very sensitive to the training waveforms used to pick the features. Also, the approach considered did not generalize to different experimental setups.

2.5 Statistical Life Prediction Methodologies

Complementary approaches to the sensor-based SHM techniques are damage estimation and life prediction methodologies based on the stochastic nature of fatigue. For aerospace structures, the industrial standard for damage estimation is based not on active monitoring of the structure but rather on making inferences about the presence of damage based on

the statistics of fatigue damage propagation combined with any NDE inspection data available. An example is the structural appraisal of fatigue effects (SAFE) methodology, which attempts to combine a known stress history with full-scale fatigue tests to generate an estimate of the amount of fatigue life expended (FLE) for a particular aircraft [39]. Once the FLE exceeds 100%, the aircraft (or critical component) is removed from service, regardless of the extent of damage. In other words, the idea is to ensure that significant damage will not develop during the life of a component. This approach is based on military aircraft usage during the Cold War, where performance obsolescence, rather than structural damage, was the primary factor in determining when to retire an aircraft from use. The maintainers of the current aircraft inventory, however, do not have this luxury since airframes are pushed well beyond their originally intended service life.

Given the need to keep an aging aircraft inventory flying, several authors have proposed statistical approaches for quantifying the inherent risk for operating aircraft beyond 100% FLE. As an example for a US Navy P-3 [39, 40], a Bayesian approach is presented to combine the distribution of damage at 100% FLE with damage propagation equations to estimate the distribution of damage at later FLE values. Their approach is to first assume a prior distribution for the crack length at a critical location of the airframe at 100% FLE. Next, a conditional distribution of the crack lengths given the % FLE is created assuming a relationship between FLE and crack length. Several assumptions, captured with three random parameters, are made regarding the correspondence of the % FLE and the crack length distribution.

A two-stage Bayesian updating procedure is used to update this conditional distribution by refining the estimates of the parameters relating FLE to the crack length distribution. The first stage uses Monte Carlo iterations of a crack growth model to estimate the distribution of cracks at a future % FLE. Through Bayes' theory, the distribution of the parameters relating % FLE to crack length are updating using the new knowledge gained from the

crack growth model. The second Bayesian stage is generated by updating these new distributions with any inspection data present. This approach is shown capable of estimating the extent of damage at FLE values greater than 100%.

Another approach to stochastic life approximation is known as a "Fail Safe" design, which is a damage tolerant strategy. This methodology attempts to ensure that while some damage may exist in the structure, it is tolerated if models and testing indicate that cracks will not propagate past a safe limit before the next inspection. A key contribution of this approach is the optimizing of the inspection interval to ensure the safety of the structure. Grooteman [41] presents a strategy for estimating the size of defects using a Fail Safe methodology. His approach is based on using the distribution of total service life of a series of aircraft, defined by a crack reaching a critical length. Using this information, combined with crack growth models and probability of detection curves for an NDE inspection technique, he back-propagated the growth of the crack until it reached the minimum detectible size. This methodology provides a pdf of the service life when the aircraft has a detectable crack size. The initial inspection time is defined based on a probability threshold for the distribution. Finally, for each subsequent inspection, the expected service life distribution is updated by forward propagating the distribution with crack growth models, assuming no detected defects. This approach creates a distribution of expected service life, which is updated after each inspection.

CHAPTER 3

EXPERIMENTAL APPROACH

The experimental approach focuses on generating fatigue cracks near fastener holes and monitoring their growth via ultrasonic sensing techniques. A series of aluminum alloy fatigue coupons with fastener holes were manufactured and fatigued to generate cracks typical of what might be expected to form under field conditions. Ultrasonic waveforms were recorded throughout the fatiguing process and analyzed using an energy-based algorithm to detect and size any cracking generated. Details are described in this chapter, including details of the fatigue tests, the ultrasonic monitoring method, and the effect of transducer position. Also, a list of all experiments used during the development of this thesis is provided.

3.1 Fatigue Tests

3.1.1 Specimen Geometry

The geometry of the specimen is a rectangular aluminum coupon with two fastener holes in the center of the sample. The specimens are manufactured from aluminum alloys used in aircraft structures. The dimensions of the samples fatigued are a thickness of 5.72 mm, length of 304 mm and width of 47 mm with the two 4.82 mm diameter holes in the center of the sample spaced 22.1 mm apart, as shown in Figure 4. The holes represent fastener holes on aircrafts and provide stress risers for crack formation. The hole and sample geometries are such that stresses on either side of the hole are approximately equal, and the hole separation is sufficient so that each of the two holes can be considered to be independent with respect to crack initiation and growth.

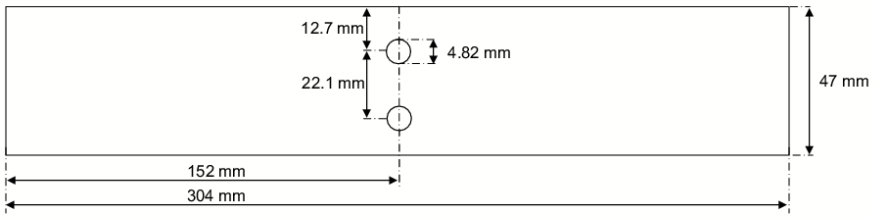

Figure 4: Drawing of two-hole fatigue coupon.

3.1.2 Material Properties

The specimens are manufactured from a variety of aluminum alloys, including 7075-T651 and 7050-T7351, with the majority being made of 7075-T651. Several material properties are of interest for the work presented here. Specifically, the fatigue properties, elastic moduli, and acoustoelastic constants are necessary for the development of the required SHM modules, summarized in Table 1. A variety of sources are used to obtain the material properties [42, 43, 44]. For the two crack growth constants listed in Table 1, 7075-T6 Al values are provided, with the assumption that the difference in temper would result in similar crack growth curves; both -T6 and -T651 treatments are produced by first heat-treating and then artificially aging the specimen, with -T651 receiving additional stretching for stress-relief [45].

3.1.3 Fatigue Process

All samples are fatigued at 5 Hz with a purely tension spectrum of repeated 2640 cycle blocks using an MTS fatigue machine [46]. The TestStar-II software package is utilized to implement the load control fatigue process. The fatigue spectrum is intended to replicate the aperiodic loading experienced by a outer wing panel fastener hole during service of a military aircraft [2]. An illustrative portion of the spectrum is provided in Figure 5.

The spectrum is divided into high and low stress packets, with approximately 70% of the cycles considered low stress. The peak loading of the spectrum is approximately

Table 1:

Material properties for 7075-T651 aluminum.

E	ν	c_L	c_T
67.56 GPa	0.345	3128 m/s	6321 m/s

Lamé Constants		Murnaghan Constants		
λ	μ	m	n	l
54.9 GPa	26.5 GPa	-252.2 GPa	-325 GPa	-351.2 GPa

Crack Growth Constants	
C	m
$2.71X10^{-8}$ MPa $\sqrt{\text{mm}}$	3.70

17,500 lbf (77,840 N), which corresponds to a stress of 284 MPa away from the hole, approximately 60% of the yield stress. Each sample was fatigued to different points of remaining life to generate a range of crack geometries and sizes. Once the fatigue process was completed, the samples were fractured and the visible crack surfaces were recorded using digital photography.

3.2 Ultrasonic Monitoring Methodology

The method for ultrasonically monitoring the fastener holes is to bond a pair of angle beam transducers using epoxy in a pitch-catch configuration on opposite sides of the hole with the direction of propagation parallel to the loading axis [43, 47, 48, 49]. The transducers used in this research are Panametrics A5054 70 ° shear wave (in steel), 10 MHz transducers. The predominant direction of crack growth is perpendicular to the loading direction at the 3 and 9 o'clock positions because of stress concentrations caused by the fastener hole, resulting

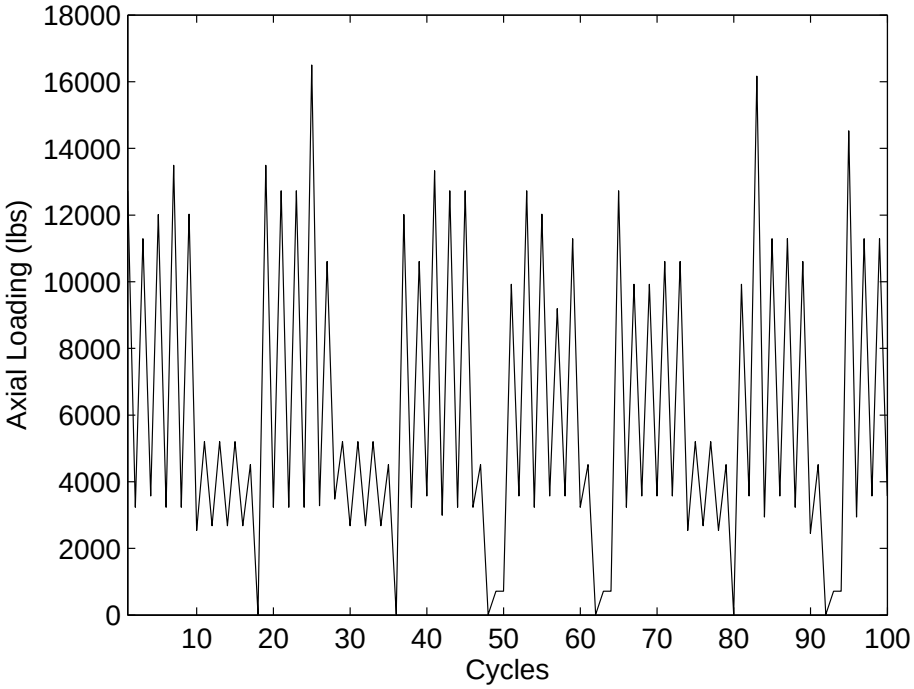

Figure 5: Portion of the fatigue spectrum.

in this transducer configuration maximizing the effect of the cracks on the recorded signals. Figure 6 illustrates how the fastener hole creates a shadow on the opposite side of the hole, effectively blocking any direct arrivals.

3.2.1 Waveform Analysis

The ultrasonic waveform feature used for data analysis is a ratio of signal energies from samples under tensile loading to their unloaded counterparts normalized by the ratio from the undamaged specimen. It is thus a measure of the ultrasonic response because of load, primarily caused by cracks opening [48]. The energy in a specified time window for a given

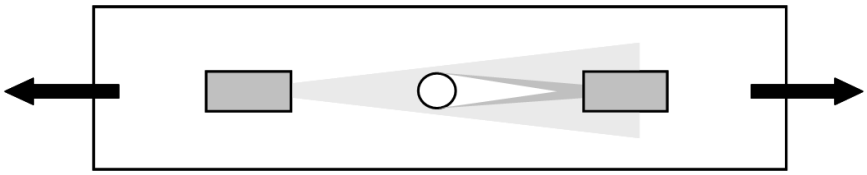

Figure 6: Transducer arrangement on sample.

number of fatigue cycles and load level is calculated as

$$E(n, L) = \int_{t_{min}}^{t_{max}} x^2(t; n, L)dt, \tag{12}$$

where this equation is given in continuous time for clarity. Here $x(t; n, L)$ is the waveform recorded during n^{th} ultrasonic measurement set and with an applied load of L, and the total time window considered is from t_{min} to t_{max}.

A reference load is selected to be large enough to fully open any cracks that are present. Figure 7 is a typical plot of energy versus load showing the effect of cracking on the received energy. Note that as the loading increases from zero to about 7,000 lbs (115 MPa), the energy reaching the receive transducer decreases when the crack is present. The energy is essentially constant as the loading increases past this point, indicating that the crack is fully opened. On the other hand, when no cracking is present, there is a reduced effect on the ultrasonic energy versus load. Thus, a reference load of 10,000 lbs (164 MPa) is more than sufficient to open this crack; prior experience has shown that this loading is effective for fully opening cracks of various sizes and locations [43].

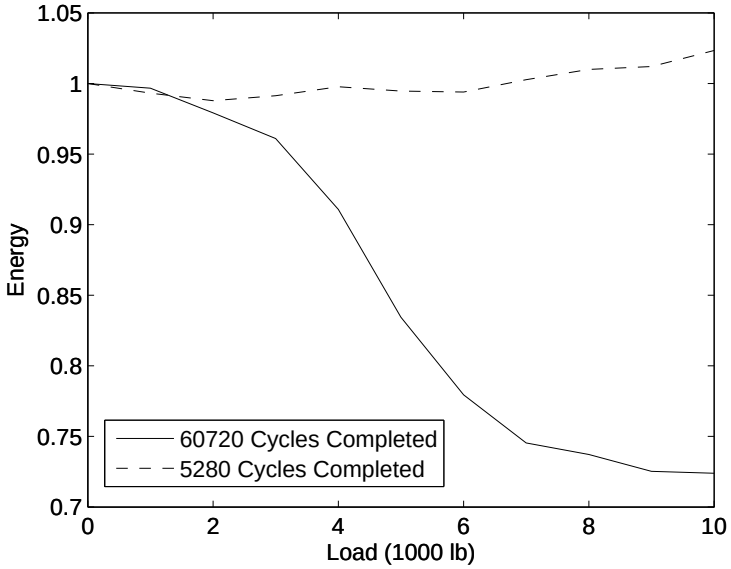

Figure 7: Example of an energy versus load curve for a hole with and without cracks.

The raw energy ratio is calculated as the ratio of the signal energy recorded at the reference load to the signal energy at zero load,

$$R'(n) = \frac{E(n, L_{ref})}{E(n, 0)}. \tag{13}$$

The resulting raw energy ratio, $R'(n)$, is normalized by the initial value from the undamaged specimen during measurement set n_0,

$$R(n) = \frac{R'(n)}{R'(n_0)}. \tag{14}$$

This normalized energy ratio is examined as a function of fatigue cycles, where the indication of cracking is a drop in the curve. Figure 8 illustrates an example energy ratio curve.

3.2.2 Ultrasonic Monitoring Hardware and Software

The data acquisition hardware is a mixture of commercially available components and custom built devices. Figure 9 illustrates the hardware used for instrumenting the ultrasonic transducers. Specific instrumentation items are described as follows:

1. A custom-built 16 channel multiplexer was developed for use with the SIPS program. The multiplexer serves as a bridge between the transducers and the pulser-receiver hardware. The multiplexer allows interfacing with 16 individual transducers, where

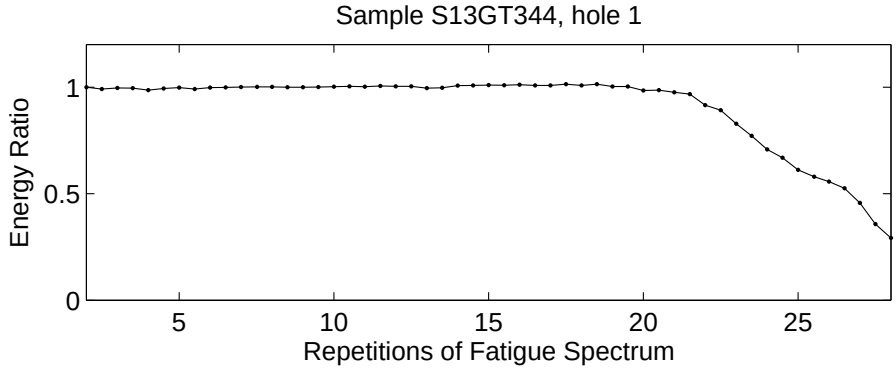

Figure 8: Example energy ratio curve.

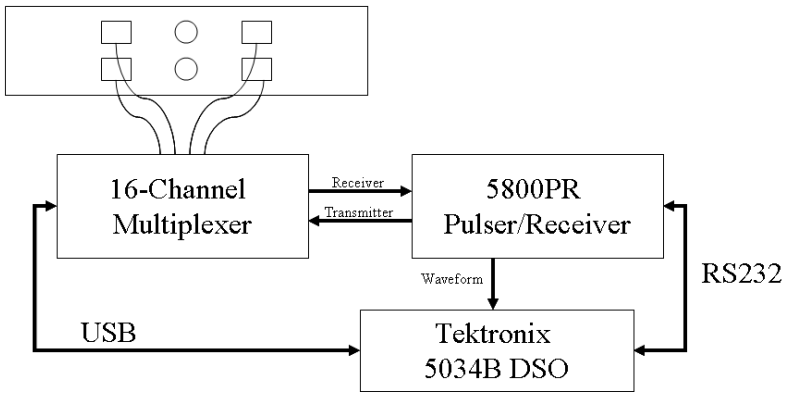

Figure 9: Block diagram of the instruments and the interconnections between them.

each can be used as either transmitter or receiver. The interfacing to the multiplexer is through a standard USB interface with a commercially available USB controller hardware from ActiveWire, Inc. [50].

2. A Panametrics 5800PR computer controlled pulser-receiver is used to generate the excitation signal for the transmitter and amplify the received ultrasonic waveforms. The excitation signal is an impulse, resulting in a broad-band received signal. The standard configuration of the 5800PR is the following:

   (a) Gain: 40 dB

   (b) Pulser Repetition Frequency: 100 Hz

   (c) Pulse Energy: 50 μJs

   (d) Damping: 50 Ohms

   (e) Low Pass Filter: 35 MHz

   (f) High Pass Filter: 1 MHz

   Additionally, the attenuation levels are set such that the received waveforms are approximately 180 mV peak-to-peak. The control of the 5800PR is through the RS232 serial port interface using the control codes provided in the device interface manual.

3. A Tektronix 5034/5034B Digital Storage Oscilloscope (DSO) is used as the data acquisition hardware. Additionally, the DSO has a built-in Windows 2000 platform. The DSO settings for waveform capture are the following:

   (a) 40 μs capture window, beginning 8 μs after transmitter excitation

   (b) 5000 sample point waveforms utilizing a 125 MHz sampling frequency to ensure a well-sampled signal with no aliasing artifacts

   (c) 200 mV peak-to-peak waveform capture

   (d) 50 averages of each waveform for electronic noise removal

A custom designed data acquisition software suite was developed using the National Instruments LabVIEW environment. The software allows for automatic acquisition of the ultrasonic waveforms with computer control of the each of the three components (DSO, 5800PR, and multiplexer). The software runs on the Windows 2000 environment on the DSO using the device drivers provided by the hardware developers to interface with each of the instrumentation components.

3.2.3 Data Collection Methodology

The measurement schedule for the ultrasonic signals was to record waveforms after every 1320 to 2640 cycles of fatigue by interrupting the fatigue process. The waveforms were captured at several static load levels, specifically no load to 10,000 lbs. (44,482 N) in 1000 lb. (4,448 N) increments. This process was repeated until fatiguing is terminated.

3.3 Ultrasonic Transducer Configuration

The angle beam configuration described in Section 3.2 allows the ultrasonic energy to propagate between the transmitter and receiver via boundary reflections on the top and bottom surfaces of the sample. Two different configurations for the transducers are considered during the development of this thesis. For both configurations, the transmitter is mounted such

that the ray path of peak ultrasonic energy passes through the through-thickness midpoint of the hole. The first configuration places the receiver where the first two received arrivals are balanced in amplitude. Multiple arrivals at one location are a result of the beam spread of the transmitting transducer. The second configuration places the receiver where a single ultrasonic arrival has maximum amplitude. This section details the beam paths for each approach, demonstrating how the second option is preferred for defect detection.

3.3.1 Balanced Arrivals Configuration

The first mounting configuration considered for monitoring the fastener hole is to place the receiver so that the first two arrivals are balanced. The intent of this mount location is to insonify the entire height of the hole, ensure symmetric transmitter and receiver positioning, and receive multiple echoes for signal analysis. The beam paths for this configuration are shown in Figure 10. The mounting procedure is summarized as follows:

1. Determine the transmitter position that maximizes the half and full V pulse-echo signals when aimed at the apex of the hole;

2. Move the transmitter half the hole diameter toward the hole and fix with epoxy. The net effect is that the ray-path of peak ultrasonic energy passes through the approximate center of the height of the hole;

3. Adjust the receive transducer axially so it is located where the first and second arrivals of the through-transmission signal are balanced in amplitude, and adjust it

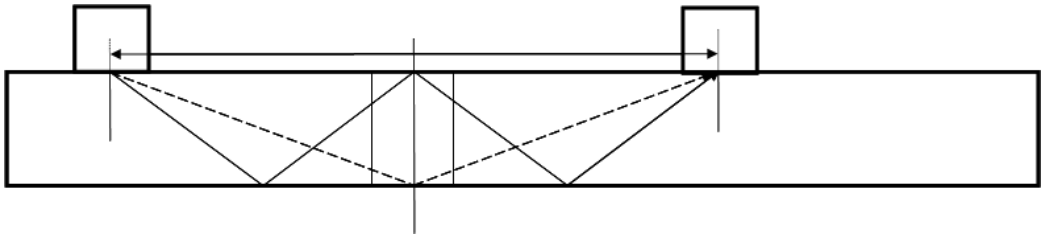

Figure 10: Beam paths for the “Balanced Arrivals” transducer configuration.

transversely to minimize the amplitude, ensuring equal energy on both sides of the hole (3 and 9 o'clock positions).

3.3.2 Center Peaked Configuration

The second transducer configuration places the receiver such that a single arrival maximized, which provides an increased sensitivity toward the center of the hole height. An illustration of the beam path associated with this configuration is shown in Figure 11.

The mounting procedure for this configuration is distance-based to ensure that the center of the hole surface is monitored. As before, the transmitter is positioned such that the highest energy beam path, along refracted angle θ_{trans}, passes through the center of the hole after a boundary reflection on the bottom surface of the sample. Therefore, the distance from the center of the hole to the transmission point on the surface of the sample is

$$x_1 = 1.5h/\tan(\theta_{trans}), \tag{15}$$

where h is the sample thickness.

The mounting location for the receiver is similar to that of the transmitter. Three boundary reflections are assumed between the two transducers along the same refracted angle. The total distance between the two transducers is given by

$$x_{tot} = 4h/\tan(\theta_{trans}). \tag{16}$$

The x_1 distance is subtracted from this value to obtain the mounting distance from the

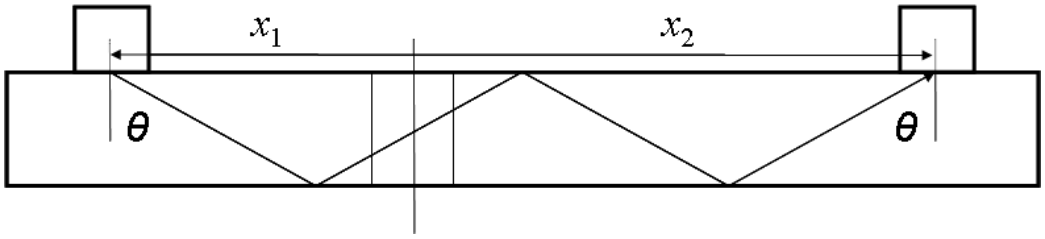

Figure 11: Beam paths for the "Center Peaked" transducer configuration.

center of the hole for the receiver,

$$x_2 = x_{tot} - x_1. \tag{17}$$

3.3.3 Configuration Comparison

Research was performed to compare the two transducer configurations to determine which one is best suited for monitoring fatigue cracks. For direct comparison experiments, the "Center Peaked" mounting was modified to place the receive transducer on the opposite surface of the sample. An additional receiver was placed on the top surface, balancing the first and second arrivals for the "Balanced Arrivals" configuration. Thus, two transducers act as receivers, one for each of the two transducer configurations. The beam paths for both receivers is shown in Figure 12. It should be noted that it was not possible to mount both receivers on the same sample surface due to the physical transducer dimensions.

A series of fatigue experiments were performed and the ultrasonic data was analyzed using the energy ratio algorithm. A total of seven experiments were performed with an ultrasonic measurement interval of 1320 cycles. Since both transducer configurations were employed on the specimen, their energy ratio responses can be directly compared. One set of energy ratio curves is shown in Figure 13. As can be seen, there is an approximate 5280 cycle (4 measurements) improvement for this hole using the "Center Peaked" mounting configuration, indicated by the earlier drop in the energy ratio response. Table 2 summarizes the point of defect detection, measured in fatigue cycles, for the "Balanced Arrival" and "Center Peaked" mountings from all seven experiments. As this table shows, out of

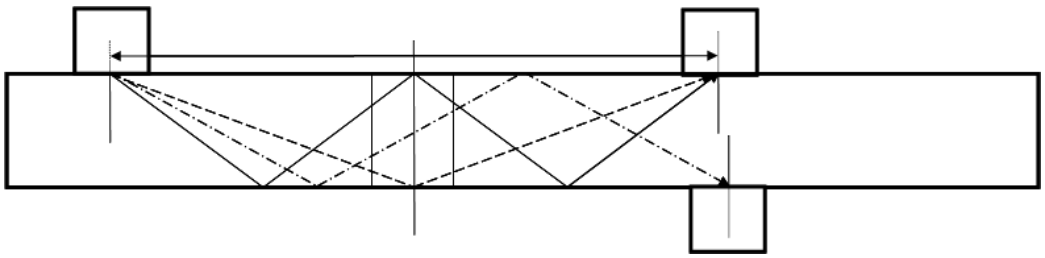

Figure 12: Beam paths for the transducer configuration used for comparing mounting strategies .

seven total holes, six of the experiments show improved crack detection using the "Center Peaked" mounting. Thus, the "Center Peaked" configuration is the preferred approach for the specimen geometry considered here.

3.4 Experiment Summary

In support of SIPS program outlined in Section 1.1, several different fatigue coupon configurations were used for the experimental approach described in this chapter. For this thesis, however, only a subset of these experiments is used for the development of the SHM framework. The experiments utilized both transducers configuration described in Figures 10 and 11. The "Balanced Arrivals" configuration results are used during the development of the detection strategy for initially ascertaining the presence of fatigue damage within the structure. The "Center Peaked" configuration results are used for the development of the remaining SHM framework, where the detection strategy from the prior configuration is modified for integration into the overall methodology.

A summary of the experiments used during the development of the thesis is provided in Table 3. An experiment is defined as a single hole being monitored with the ultrasonic sensing methodology. The two fastener holes are labeled 1 and 2, with hole 1 located on the near side of the fatigue machine. Only one of the holes is useful for the development

Table 2:

Summary of detection times (cycles) using two mounting configurations.

Sample	Balanced Arrival Mounting	Center Peaked Mounting
S13GT344 Hole 1	72600	54120
S13GT346 Hole 2	71280	77880
S13GT366 Hole 1	59400	56760
S13GT366 Hole 2	54120	51480
S13-0316 Hole 2	47520	46200
S13-0331 Hole 2	64680	59400
S13-0355 Hole 1	No Detection	62040

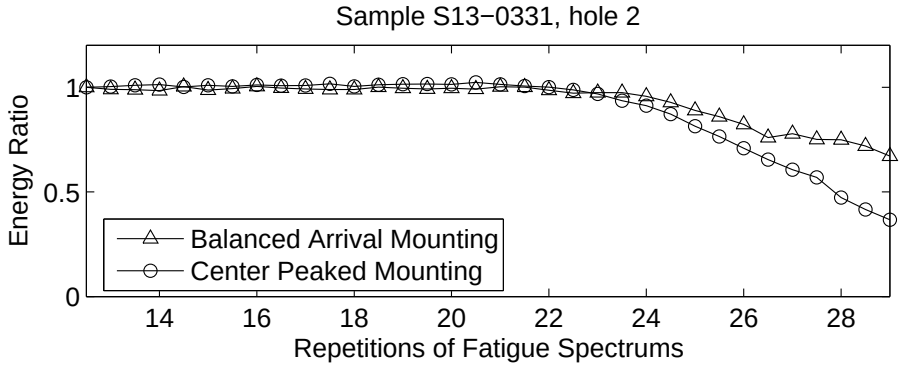

Figure 13: Energy ratio comparison between the two transducer configurations.

of the thesis for most experiments; because of experimental and manufacturing variations, generally only one hole had noticeable fatigue damage when the tests were stopped. Also, some additional experiments are unusable because of errors in the experimental process, such as a transducer disbond.

Finally, for each of the experiments used in the thesis development, data were acquired with a regular acquisition interval of either 1320 or 2640 cycles to simplify the data acquisition procedure. However, a variable acquisition interval could have been used with no change to the presented SHM framework.

Table 3:

Summary of experiments performed during thesis development

Sample Name	Hole #	Alloy	Configuration	Where used	Acquisition Interval
S13-0316	2	7050	Both	Chapt. 3	1320 Cycles
S13-0331	2	7050	Both	Chapt. 3	1320 Cycles
S13-0355	1	7050	Both	Chapt. 3	1320 Cycles
S13GT344	1	7050	Both	Chapt. 3	1320 Cycles
S13GT346	2	7050	Both	Chapt. 3	1320 Cycles
S13GT366	1	7050	Both	Chapt. 3	1320 Cycles
S13GT366	2	7050	Both	Chapt. 3	1320 Cycles
S3-0001	2	7075	Balanced	Chapt. 4	2640 Cycles
S4-0025	2	7075	Balanced	Chapt. 4	2640 Cycles
S4-0026	2	7075	Balanced	Chapt. 4	2640 Cycles
S4-0030	1	7075	Balanced	Chapt. 4	2640 Cycles
S4-0031	1	7075	Balanced	Chapt. 4	2640 Cycles
S4-0466	1	7075	Balanced	Chapt. 4	2640 Cycles
S4-0466	2	7075	Balanced	Chapt. 4	2640 Cycles
S4-0560	1	7075	Balanced	Chapt. 4	2640 Cycles
S4-0560	2	7075	Balanced	Chapt. 4	2640 Cycles
S4-0188	1	7075	Peaked	Chapt. 6/8	1320 Cycles
S4-0373	1	7075	Peaked	Chapt. 6/8	1320 Cycles
S4-0428	1	7075	Peaked	Chapt. 6/8	1320 Cycles
S4-0486	1	7075	Peaked	Chapt. 6/8	1320 Cycles
S4-0438	1	7075	Peaked	Chapt. 6/8	1320 Cycles
S4-0468	1	7075	Peaked	Chapt. 6/8	1320 Cycles
S4-0504	1	7075	Peaked	Chapt. 6/8	1320 Cycles
S4-0553	1	7075	Peaked	Chapt. 6/8	1320 Cycles

CHAPTER 4

DETECTION STRATEGY

The focus of this chapter is to describe the methodology for detecting the first indication of defects growing from the fastener holes. This detection strategy is used before attempting to size the defects and estimate the remaining life of the structure. The arrangement of the chapter is to first provide a brief overview of the presented methodology along with a discussion of related approaches to defect detection using ultrasonics in Section 4.1. Section 4.2 provides the details of the proposed crack detection algorithm. Section 4.3 outlines the approach for improving the detection performance using time and frequency waveform features, and Section 4.4 describes an automated enhancement procedure using these features. Experimental results are shown in Section 4.5.

4.1 Strategy Overview

The approach for detecting defects near fastener holes is to take advantage of different time and frequency regions of the received ultrasonic waveforms combined with an empirical detection algorithm. The overriding assumption is that some time and frequency windows of the received ultrasonic signal may be more sensitive to cracking than others because of the complex interaction of the incident ultrasound with any cracks that may be present. The use of time-and-frequency dependent information is well-established for ultrasonic nondestructive testing. For Rayleigh waves, the skin depth is proportional to the wavelength with lower frequencies able to penetrate deeper into the material. Such behavior has been used to deduce crack depth [12, 51] and depth-dependent material properties [52]. For conventional bulk wave testing, the minimum detectable defect size is approximately

inversely proportional to frequency, but depth of penetration decreases with increasing frequency [53]. For coarse-grained materials, unlike fine-grained aluminum alloys, scattering from cracks has been observed to be more broadband than scattering from grains, and split-spectrum processing methods have been developed based on this behavior for detecting crack echoes that are buried in coherent noise [21, 23]. Feature-based approaches have been developed where various features are calculated in the time and frequency domains, and those features are used to facilitate the flaw detection and characterization process [38]. Other time-frequency representations, such as the short time Fourier transform and wavelet transforms, have also been used to obtain time-frequency features that can be correlated to the presence of defects [54, 55].

These approaches, however, are not directly applicable to the monitoring of fastener hole cracks using the employed angle beam configuration. The reason is because the temporal locations of interest in the ultrasonic waveform are well defined. Further, the frequency-dependent behavior is complex given the wide range of possibilities in terms of number of cracks present, crack depth(s) and specific crack location(s) through the thickness. The work presented in this chapter considers an extension of the energy ratio technique where information from specific time and frequency windows is incorporated into an automated crack detection strategy. By considering energy ratios computed from a large number of time-frequency combinations, the ones that are most effective for early detection of cracks can be automatically determined. Integral to the processing is the development of an automated crack detection algorithm, which permits objective and efficient analysis of multiple energy ratio curves determined from the various time-frequency windows.

4.2 Crack Detection Algorithm

An automated crack detection algorithm is implemented to determine the ultrasonic measurement set when cracking is detected, referred to as the detection point, based on the energy ratio curve. Analysis of the energy ratio curve is based upon dividing it into separate

sections. The initial, or pre-crack, portion of the curve is typically close to horizontal, indicating that the ultrasonic response is not varying with load and that a crack is not present. The start of the second portion of the curve is defined as when this horizontal portion ends and the energy ratio begins to decrease, and is considered to be when the crack is detected.

The basis of this crack detection algorithm is to compare the current energy ratio to its predicted value based upon a set of past values. This procedure is illustrated in Figure 14. Let n_c denote the current measurement set and let N be the number of measurements sets that are used for the prediction, hereafter referred to as the prediction set. The prediction set is assumed to be representative of the sample without damage. Additionally, there is a gap of S measurements between the prediction set and the current measurement to allow any small cracks to have S measurements in which to propagate prior to detection. In Figure 14, values of $N = 6$ and $S = 2$ are used.

Consider the local linear fit of the energy ratio curve using the N points in the prediction set,

$$\hat{R}(n) = kn + b_0, \tag{18}$$

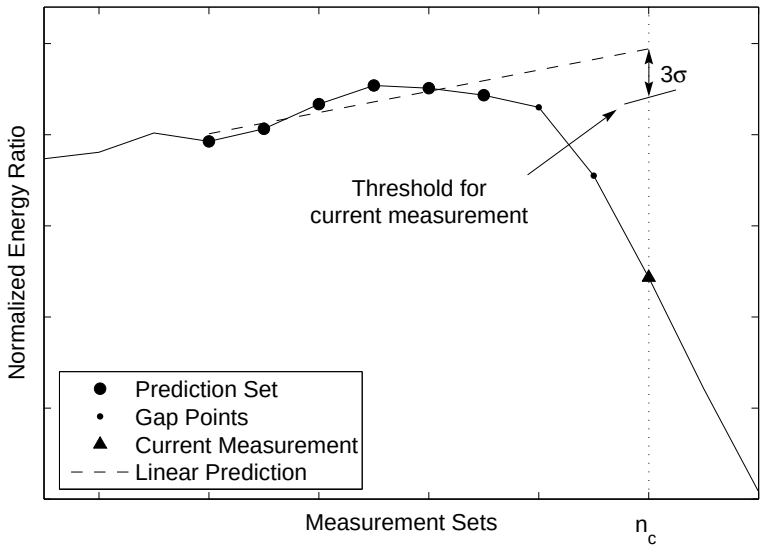

Figure 14: Illustration of the crack detection algorithm with $N = 6$ and $S = 2$.

where $\hat{R}$ is the linear fit, and k and b_0 are the slope and intercept, respectively, and n is the measurement set. Then the difference, or error, between the actual energy ratio and the linear fit is

$$e(n) = R(n) - \hat{R}(n) = R(n) - (kn + b_0). \tag{19}$$

The standard deviation, σ, of the error is then calculated for the points comprising the prediction set. A defect is said to be found if the actual energy ratio at the current measurement, n_c, drops three standard deviations (3σ) below the linear prediction (i.e., $e(n_c) < -3\sigma$). The range $\pm 3\sigma$ from the linear prediction represents 99% of the random uncertainty in a single measurement of R, and thus there is a 0.5% chance that the next measurement of R will fall below the lower 3σ threshold if there is no crack (and a corresponding 0.5% chance that it will fall above the upper 3σ threshold). If there is a crack, then at some point the energy ratio will fall below the -3σ level and thus cross the detection threshold. An example of how the linear prediction and threshold for defect detection are updated for each measurement is shown in Figure 15.

The intent of the prediction set is to characterize the behavior of the ultrasonic energy ratio before cracks are detected. Initially, the prediction set is the first N points at the start of the energy ratio curve, where the assumption is necessarily made that no cracking has occurred within this set. Points from $N + 1$ through $N + S$ are analyzed using this initial prediction set, where the gap varies from 0 to $S - 1$ points. As the energy ratio curve is analyzed past the point $N + S$, the prediction set of N points slides forward in time, maintaining a gap of S points, as long as each subsequent point is within 3σ of the linear prediction. However, if $R(n_c)$ is outside of the 3σ window because of either noise or cracking, the prediction set remains fixed while the current measurement set moves forward in time. Also, the prediction set does not necessarily consist of consecutive points. If a measurement set is classified as a defect because of noise in the measurement, later sets that indicate no defects are still used for the prediction set but the misclassified measurement set is excluded, thus making the detection algorithm less sensitive to noise and also more

conservative with respect to false alarms. The point of crack detection is defined to be the measurement in which it and all the following sets are classified as defective.

The crack detection algorithm examines all values after N measurements until either the final measurement or the stop condition is reached. The stop condition is added because the energy ratio is not meaningful during the final 5-10% of the fatigue life. Specifically, the cracks are very large at this point and are not fully closed by compressive residual stresses at zero applied load. Furthermore, the ultrasonic signals are much reduced in amplitude and very distorted in shape compared to signals from the undamaged sample. This situation is recognized by simply monitoring the energy of the entire digitized record from the unloaded specimen. Once it drops below 50% of the original no load energy, the crack is affecting the through-transmission signal with no loading, unambiguously indicating the presence of a defect, and the current and all subsequent measurements are classified as defective. This additional test also ensures eventual detection of cracks that remain partially open when the load is removed, such as could occur with an interference-fit fastener.

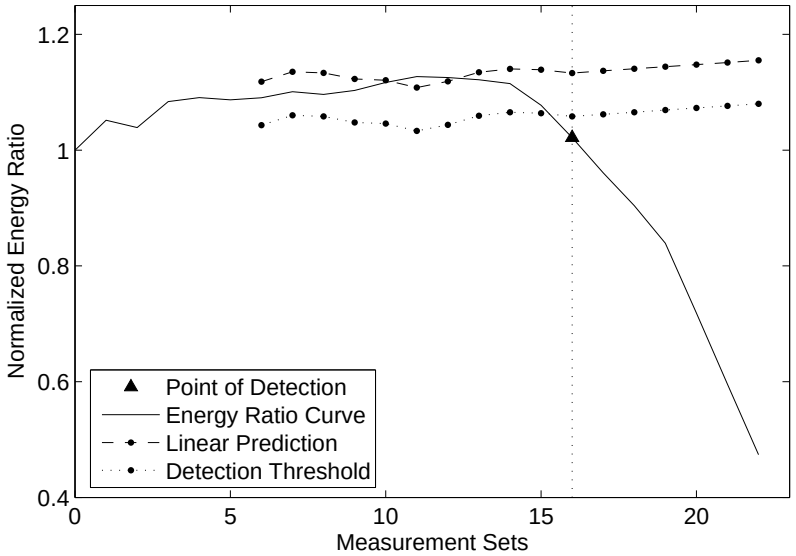

Figure 15: Example of how the crack detection algorithm is updated. The solid line is the energy ratio curve, the dashed line is the linear prediction for each point analyzed, and the dotted line is the moving threshold for flaw detection.

4.3 Energy Ratio Curves from Time-Frequency Windows

Utilization of multiple time-frequency windows is motivated by considering the propagation of ultrasonic waves from the transmitter to the receiver. A consequence of using angle beam transducers in the configuration described is that there is no direct path for the ultrasonic energy to propagate to the receive transducer; the hole is located directly between the transducers. When the transmitted wave hits the hole, it is mode converted into an evanescent pseudo-Rayleigh wave, referred to as a creeping wave [10, 56]. Because the surface is curved, this creeping wave is leaky, meaning that it radiates energy in the form of shear waves propagating tangentially from the surface of the hole. Also, the depth of penetration from the hole surface of this creeping wave varies as a function of frequency because of the frequency-dependent exponential decay constant [10]. Thus, as cracks grow from the surface, the higher frequencies will be affected more strongly than the lower frequencies as more of the ultrasonic energy is blocked by the crack.

As shown in Table 3, the "Balanced Arrival" transducer configuration is used for the development of the defect detection strategy. Referring to Figure 16, it can be seen that different time windows correspond to interrogation of different positions through the thickness; that is, the first and second arrivals would be expected to be more sensitive to cracks near the bottom and top surfaces, respectively. Thus, considering multiple frequency windows of the two arrivals could provide improvements over the single window analysis approach because of the potential for increased sensitivity of a specific window to different crack locations and depths.

Multiple time-frequency windows are implemented by windowing the waveforms in time and frequency before calculating the energy ratio curves. Because of the transducer configuration, two separate beam paths reach the receive transducer, resulting in two arrival packets for consideration, as shown in Figure 16(a). The method for implementing the time windowing is to create four separate windows for each waveform. The four time windows considered are (1) original 40 μs full-time window, (2) first arrival window, (3)

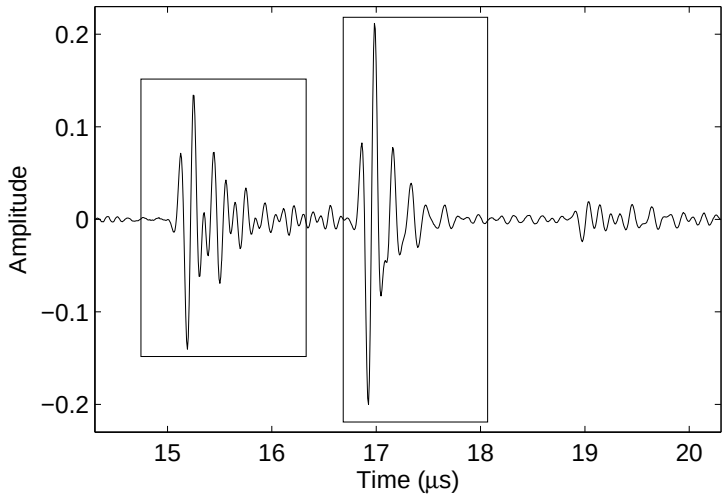

(a)

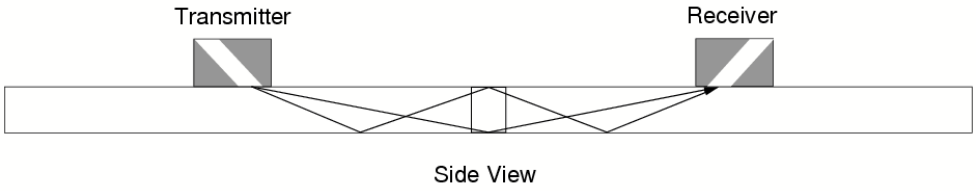

(b)

Figure 16: Relationship between different (a) arrivals in the ultrasonic waveform, and (b) wave propagation paths. The first arrival in (a) corresponds to the single V path in (b), whereas the second arrival in (a) corresponds to the double V path in (b).

second arrival window, and (4) a two peak window that encompasses the first two arrivals. The limits of the arrival windows are defined based upon visual inspection of the first measurements taken for each sample. Due to transducer movement and loading induced changes in both ultrasonic velocity and specimen dimensions [43], recorded waveforms are slightly shifted in time compared to those from the undamaged and unloaded sample. Signals are cross-correlated to obtain the time shift and windows are adjusted accordingly. The resulting time-windowed signals as a function of measurement set, n, and load, L, are

$$x_i(t; n, L) = x(t; n, L)w(t; t_1^i, t_2^i), \tag{20}$$

where x_i is the i^{th} windowed signal ($i = 1, 2, 3, 4$) and $w(t; t_1^i, t_2^i)$ is the windowing function. The times t_1^i and t_2^i define the shifted time window as determined from the cross correlation. The windowing function $w(t; t_1, t_2)$ is given as

$$w(t; t_1, t_2) = \begin{cases} 0 & t < t_1 - \Delta t, \\ \frac{1}{2}(1 - \cos[\frac{\pi(t - t_1 + \Delta t)}{\Delta t}]) & t_1 - \Delta t < t < t_1, \\ 1 & t_1 < t < t_2, \\ \frac{1}{2}(1 + \cos[\frac{\pi(t - t_2)}{\Delta t}]) & t_2 < t < t_2 + \Delta t, \\ 0 & t > t_2 + \Delta t, \end{cases} \tag{21}$$

where Δt is a windowing parameter equal to 15% of the window width (i.e., $\Delta t = 0.15(t_2 - t_1)$). The purpose of Δt is to smooth both edges of the rectangular window. Figure 17 illustrates the window function with $t_1 = 16\ \mu$s and $t_2 = 24\ \mu$s.

The frequency windowing is accomplished by transforming the time windowed waveforms into the frequency domain via the fast Fourier transform (FFT), and calculating the energy in the frequency domain for each frequency range of interest (e.g., from f_1 to f_2).

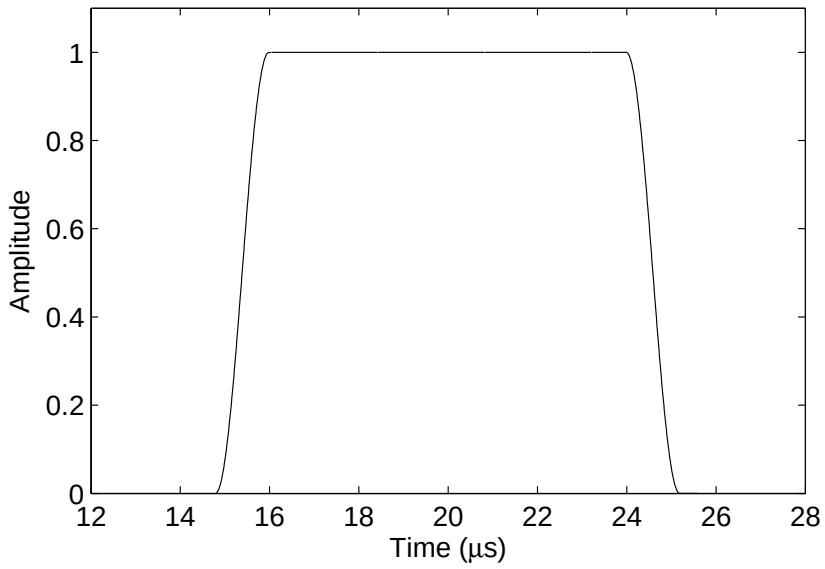

Figure 17: The time windowing function with $t_1 = 16\ \mu$s and $t_2 = 24\ \mu$s.

The energy ratio is then calculated as per Eqs. (13) and (14). Frequency regions are defined by ten integer MHz values of f_1 ranging from 5 MHz to 14 MHz, and integer values of f_2 ranging from f_1 + 1 to 15 MHz for each value of f_1, resulting in 55 possible regions ($10 \times 11/2$). Combining of time and frequency windows results in 220 (4×55) energy ratio curves where previously there was only one. The approach of first windowing in time and then taking the FFT is used rather than the STFT because of the limited time resolution of the STFT.

4.4 Automatic Window Selection

While the use of the 4 time windows and 55 frequency windows should result in at least some energy ratio curves that provide earlier crack detection using the crack detection algorithm, many of these windows do not provide any improvement as compared to the original energy ratio curve, and others may be worse. It is desirable to determine a subset of specific time-frequency window combinations that provide the most improvement, and it is beneficial for these windows to perform well for many different crack geometries. The method for determining the best performing windows is to evaluate two attributes for each of the energy ratio curves: (1) improvement in detection time, and (2) reduction in energy ratio at the time of detection. The two functions G_1 and G_2 represent these attributes for evaluating the performance of an energy ratio curve corresponding to a particular hole (experiment), n_h, and window, n_w.

The first metric, $G_1(n_h, n_w)$, quantifies the improvement in detection point,

$$G_1(n_h, n_w) = \frac{n_d^{ref}(n_h) - n_d(n_h, n_w)}{\max_{n_w} | n_d^{ref}(n_h) - n_d(n_h, n_w)|}, \tag{22}$$

where $n_d^{ref}(n_h)$ is the baseline detection time for hole n_h using the crack detection algorithm for the waveform without time or frequency windowing, and $n_d(n_h, n_w)$ is the detection time using the crack detection algorithm for hole n_h and window n_w. The denominator acts as a normalization parameter for each hole so that values of G_1 range from -1 to 1. This

metric gives the improvement in detection, where a bigger positive number means earlier detection.

The second function, G_2, is an attempt to quantify the likelihood of a false positive. When examining an energy ratio curve, the point of detection is when the curve starts to fall below the initial horizontal region. Curves that drop rapidly are preferred because there is a greater margin between the detection threshold and the curve value, which should reduce the probability of a false positive. This desired drop is quantified by the residual between the prediction and the actual energy ratio value at the detection point, n_d, computed during the crack detection algorithm,

$$G_2(n_h, n_w) = \hat{R}(n_d; n_h, n_w) - R(n_d; n_h, n_w). \tag{23}$$

The smaller this difference, the greater the chance of a false alarm. An illustration of determining G_1 and G_2 for a particular energy ratio curve is shown in Figure 18.

A cost function is used to combine these individual metrics into a single value for each

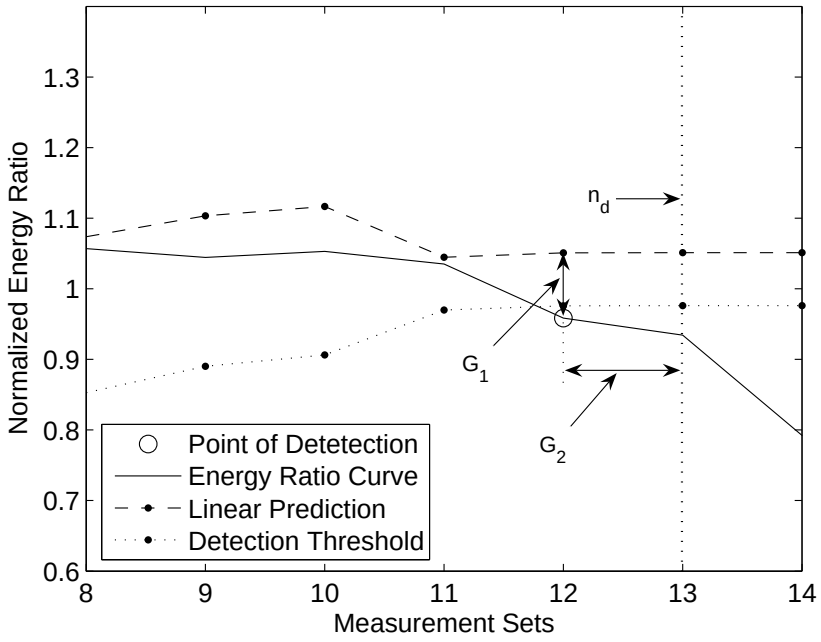

Figure 18: Example of the metrics $G_1(n_h, n_w)$ and $G_2(n_h, n_w)$ for evaluating energy ratio curves.

hole and window. This cost function is defined as

$$J(n_h, n_w) = c_1 G_1(n_h, n_w) + c_2 G_2(n_h, n_w), \tag{24}$$

where c_1 and c_2 are weighting factors. These constants are set to be equal, giving equal importance to earliest possible detection and detection margin. The cost function is evaluated for each energy ratio curve for all windows and holes.

4.5 Detection Results

The performance of the crack detection algorithm described in Section 4.2 is evaluated by comparison to visual observations. A series of eight experiments were performed to evaluate the detection strategy, summarized in Table 3. The energy ratio curves from the unwindowed signals are plotted and the detection point is determined visually. Three individuals familiar with the visual analysis of the energy ratio curves quantify the point of detection visually for each of the eight experiments. The consensus detection time was taken as either (1) the time determined by all three individuals if all are in agreement, or (2) the time determined by two of the three if two are in agreement (at least two of the three are in agreement for all cases). The automated detection point is determined by the crack detection algorithm, where the parameters N and S are set to 6 and 2 measurement sets, respectively, to provide reasonable agreement with the manual results. The manual and automated detection points are summarized in Table 4, where the number of the measurement sets at detection is reported with 2640 cycles between sets. In all cases, the automated result is within three measurement sets of the consensus manual result and is either the same or earlier as compared to the visual analysis.

Detection points for all holes were next automatically determined using energy ratio curves derived from the 220 time-frequency windows. There are four possible outcomes for each curve (1) a false positive where the curve falsely detects a crack too early in the fatiguing process, (2) an improvement in detection where the crack is detected earlier than with the full-window energy ratio curve, (3) no improvement with the crack being detected

Table 4:

Comparison of manual and automated crack detection

Hole	Manual 1	Manual 2	Manual 3	Consensus	Automated
1	10	11	10	10	10
2	14	14	14	14	13
3	11	12	12	12	11
4	13	14	14	14	11
5	15	17	17	17	15
6	19	19	19	19	18
7	16	18	18	18	17
8	14	17	17	17	14

at the same time as with the full-window curve, and (4) later (or no) detection where there is no improvement over the full-window curve. Figure 19 shows a selection of time-frequency choices where the point of detection is worse than the baseline. For comparison, Figures 20(a) and 20(b) illustrate a selection of time and frequency window combinations where there is improvement compared to the baseline. For each figure, the output of the crack

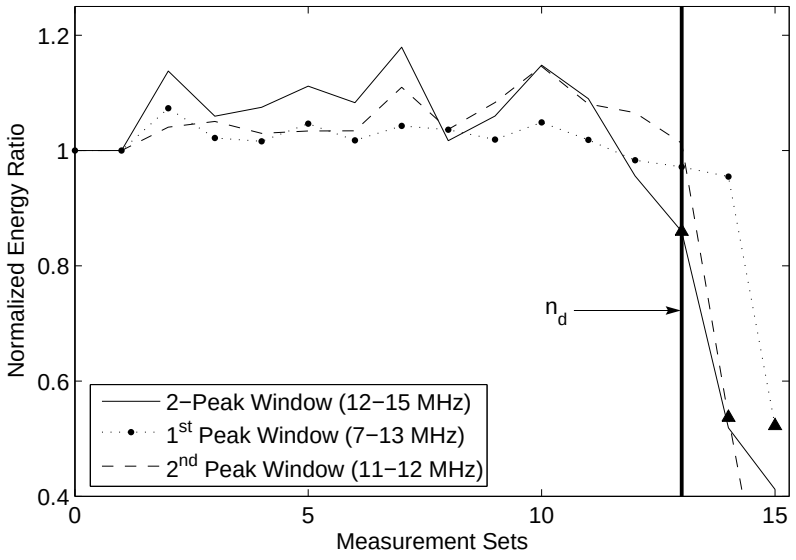

Figure 19: Examples of windowed energy ratio curves where no improvement in detection was found.

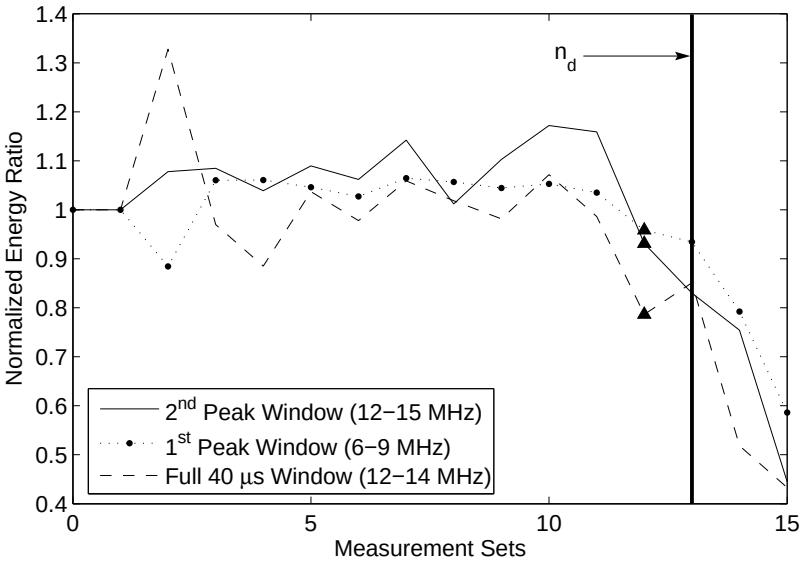

(a)

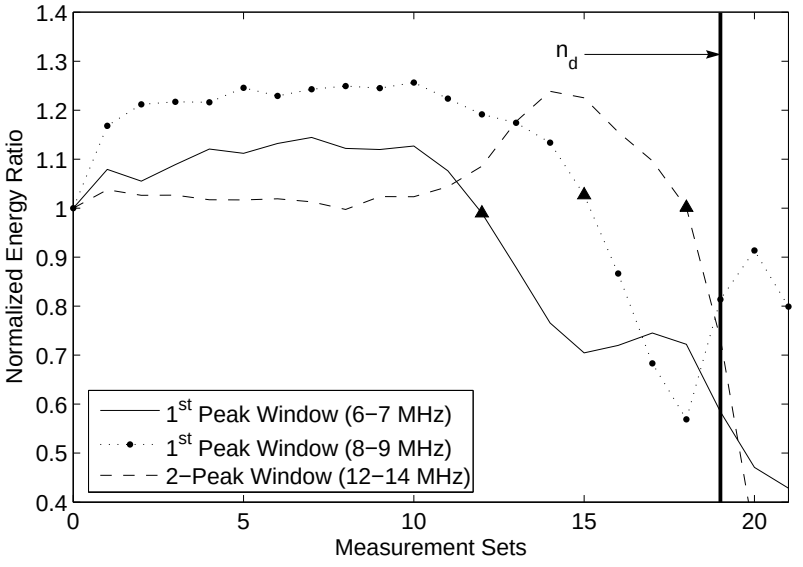

(b)

Figure 20: Examples of windowed energy ratio curves where the results provide an improvement over the original detection. (a) Hole 4 and (b) hole 6.

detection algorithm is indicated by a black triangle. Note that the second curve of Figure 20(b) attains its lowest point at measurement set 18 and then increases. This behavior is because the energy of the filtered signal is so small that the normalized energy ratio is not meaningul, as previously discussed in Section 4.2.

Results from all of the time-frequency windows are combined using a voting scheme. The logic behind this approach is that there is always the possibility of false positives, but the likelihood is reduced by ensuring that a certain percentage of the time-frequency windows indicate the presence of cracking. The percentage of windows required to detect the crack before the sample is considered damaged is set to 10%, where this value is empirically determined to minimize false positives. It should be noted that late or missed detection by some of the time-frequency windows is not a problem because of this voting scheme; as long as more than 10% of the curves indicate cracking, the defect will be detected.

Table 5 compares detection results for the baseline full window curve (column two) to time-frequency windowing with all 220 windows (column three), where the results are generated using this voting scheme. Again, the measurement set number at detection is reported. There is an average performance increase of approximately 0.5 measurement sets (1320 cycles), but for several holes, there is no improvement over the baseline results. Overall, the improvement from this implementation is not substantial, but there are no false

Table 5:

Summary of crack detection results using time-frequency windows.

Hole	Number of Windows						
	1	220	20	30	40	50	60
1	10	9	9	9	9	9	10
2	13	9	6	9	9	9	9
3	11	11	11	11	11	11	11
4	11	13	13	13	13	13	13
5	15	16	6	15	16	16	16
6	18	19	12	12	12	12	13
7	17	17	11	11	16	16	17
8	14	14	14	14	14	14	14

alarms.

A reduced number of time-frequency windows is identified by using the cost function, $J(n_h, n_w)$, to favor curves as per the values quantified by the two G functions. The methodology is to sort the 1760 cost function values at detection (220 time-frequency windows $\times$ 8 experiments) in order of decreasing $J(n_h, n_w)$ and pick the windows corresponding to the largest values for the reduced set. The same voting scheme is used as previously described, with a 10% threshold for the voting. Five different numbers of windows are considered (20, 30, 40, 50 and 60), and results are summarized in columns four through eight of Table 5 along with the full window and 220 window results. An interesting side effect of the cost function approach is the avoidance of false positives as a result of the G_2 contribution; by ensuring that only defect detections where the biggest difference between expected and actual values are used, misclassifications where the energy ratio is close to the threshold for detection are not considered. This exclusion of false positives results in the reduced set of time-frequency windows being able to outperform the full 220 windows.

Table 6 lists the best ten time-frequency windows determined by the cost function, showing that the best choices are distributed over the time windows and frequency bands.

Table 6:

Ten best performing time-frequency windows

Time Window	Start Frequency	Stop Frequency
First Arrival	12 MHz	13 MHz
First Arrival	12 MHz	15 MHz
First Arrival	12 MHz	14 MHz
Second Arrival	9 MHz	11 MHz
Second Arrival	9 MHz	10 MHz
Second Arrival	11 MHz	12 MHz
Full Window	11 MHz	12 MHz
First Arrival	6 MHz	7 MHz
First Arrival	9 MHz	10 MHz
First Arrival	8 MHz	10 MHz

Figure 21 summarizes all time-frequency windows for that the average cost function is positive over all eight holes. It is interesting to note that in general both low and high frequency narrow band windows performed better than broadband windows, as evidenced by the absence of any flagged windows in the lower left corner. However, the importance of overall frequency diversity cannot be discounted. Although not shown here, every possible time-frequency window resulted in a positive cost function for at least two holes, with the exception of the three frequency bands starting at 13 MHz and higher. These high frequency, narrow band windows are most likely ineffective because of the limited energy in this frequency range.

An important observation is that the number of windows used in the analysis has a significant effect on the results. Referring to Table 5, the 30 window combination yields the best results in terms of earliest detection with no false alarms. For fewer than 30 windows, there is a high probability of false alarms because of the dominance of a few marginal windows that work extremely well for one hole but are unable to be extended to other holes. Too many windows leads to later detection because the voting scheme requires a

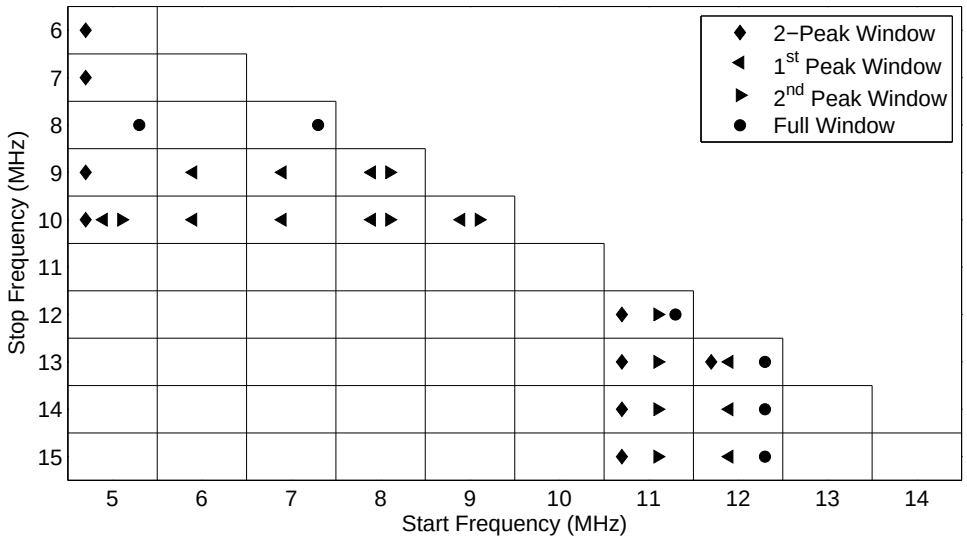

Figure 21: Summary of all time-frequency windows with the average cost function positive over all eight holes.

larger number of windows overall for detection. The average improvement using 30 time-frequency windows compared to using only the 40 μs, full bandwidth window (with the crack detection algorithm) is 1.875 measurement sets (4950 cycles), or approximately 10% of the total fatigue life. When compared to the visual method of interpreting the energy ratio curves from the 40 μs, full bandwidth window, the average improvement is 3.375 measurement sets (8910 cycles).

The voting scheme employed for determining these results requires more than 10% of the windows to detect before considering the specimen to be cracked, which corresponds to a voting threshold of four windows for the 30 window case. It is instructive to consider the effect of changing this limit. Setting the voting threshold to too small a number of windows could result in false alarms, whereas too large of a threshold could significantly delay detection. As an example, Figure 22 shows the average improvement in detection for the eight holes as a function of the voting threshold; a total of 30 windows are considered and the comparison is to the 40 μs, full bandwidth window. The initial portion of the

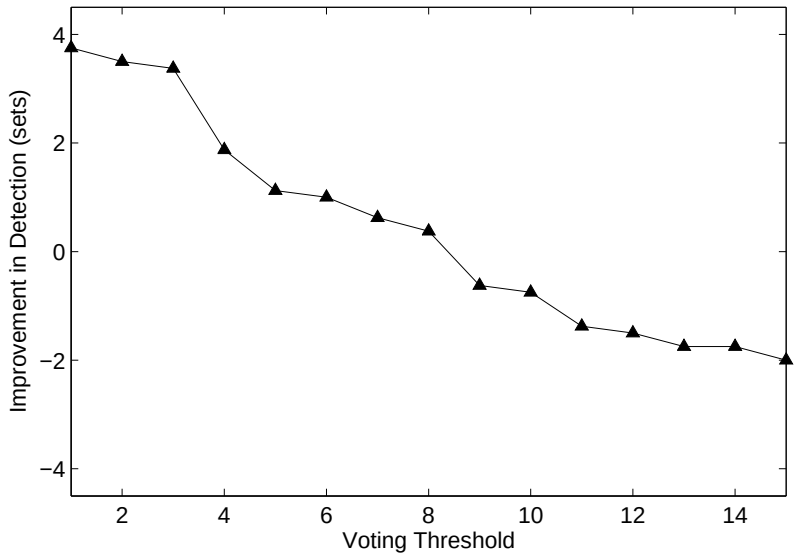

Figure 22: Average improvement from the manual baseline as a function of the number of windows required to report a defect, assuming the reduced time-frequency window implementation with 30 windows.

curve, where one to three windows are required for detection, shows a large improvement in detection, but a closer examination of the results for each hole indicates that this apparent improvement is not real but is because of false alarms for some of the holes. When four windows are required for detection, there is an abrupt drop in the average improvement, which is a result of the elimination of the false alarms. As the number of windows required for detection is increased beyond four, the average improvement decreases monotonically, and beyond eight windows the detection performance is worse than for the 40 μs, full bandwidth window, shown by the negative improvement values in Figure 22. By placing the threshold after the initial abrupt drop in improvement, which corresponds to the 10% requirement, early detection is achieved with all false positives removed for the specimens tested.

CHAPTER 5

STATE ESTIMATION APPROACH

The purpose of this chapter is to provide an overview of the state estimation approach for the SHM framework. The state estimation provides the estimate of the crack size following each additional energy ratio measurement after defect detection. The structure of the chapter is to first provide in Section 5.1 an overview of different state estimation methodologies specifically related to Bayesian estimation theory. Section 5.2 provides an overview of the state estimation approach used for this study, including a summary of the required models to be developed. Finally, a numerical example of the state estimation approach chosen is presented in Section 5.3.

5.1 State Estimation Review

With SHM, the goals are to both track the progression of damage (diagnosis) and predict the remaining life (prognosis) of a structure in near real-time, reducing the chance of failure before maintenance can be performed. For the work presented in this thesis, the remaining life is directly related to damage within the structure, specifically the presence and size of cracks emanating from fastener holes. These crack sizes, considered to be representative of the state of the structure, need to be accurately estimated with quantified uncertainty. Bayesian state estimation techniques can be employed to combine measurement models, which map ultrasonic parameters to crack dimensions, with system models, which propagate cracks with crack growth laws.

5.1.1 Bayesian State Estimation

There are inherent inaccuracies in any measurement or system model. Bayesian estimation optimally corrects these errors using the previous measurement information to estimate the

state of the system, given by the probability function

$$p(x_k|y_{1:k}), \tag{25}$$

where x_k is the state at time k and $y_{1:k}$ is the measurements of the system for all time up to k [57]. The state sequence is assumed to be a Markov random process, meaning

$$p(x_k|x_{1:k-1}) = p(x_k|x_{k-1}). \tag{26}$$

In other words, the distribution of x_k given all previous state values is only dependent on the previous state, x_{k-1}. The measurement at time k, y_k, is also assumed to have some dependence on x_k, but conditionally independent of past measurements; in other words

$$p(y_k|x_k, y_{1:k}) = p(y_k|x_k). \tag{27}$$

Generally, the goal for state estimation is to estimate the conditional pdf of x_{k+1} given $y_{1:k+1}$ from the conditional pdf of x_k given $y_{1:k}$. Using Bayes' theory,

$$p(x_{k+1}|y_{1:k+1}) = p(x_{k+1}|y_{1:k}, y_{k+1}) = \frac{p(y_{k+1}|x_{k+1}, y_{1:k})}{p(y_{k+1}|y_{1:k})} \cdot p(x_{k+1}|y_{1:k}). \tag{28}$$

From the above assumptions, it can be shown that $p(y_{k+1}|x_{k+1}, y_{1:k}) = p(y_{k+1}|x_{k+1})$, allowing for

$$p(x_{k+1}|y_{1:k+1}) = p(x_{k+1}|y_{1:k}, y_{k+1}) = \frac{p(y_{k+1}|x_{k+1})}{p(y_{k+1}|y_{1:k})} \cdot p(x_{k+1}|y_{1:k}), \tag{29}$$

with $p(x_{k+1}|y_{1:k+1})$ defined as the *posterior* distribution and $p(x_{k+1}|y_{1:k})$ as the *prior* distribution. This equation defines the update step, where the prior pdf is updated using an additional measurement and distributions related to the measurement model. The computation of this relationship requires knowledge of the prior pdf. The next step, known as the prediction step, can be written as

$$p(x_{k+1}|y_{1:k}) = \int p(x_{k+1}|x_k)p(x_k|y_{1:k})dx_k, \tag{30}$$

combining the posterior pdf from the previous timestep and a distribution, $p(x_{k+1}|x_k)$, related to the system. This two step process of updating and predicting optimally forms the

Bayesian state estimation solution, but generally these relationships are impossible to solve in closed form. Kalman filtering provides an identical formulation of Bayesian estimation assuming Gaussian noises.

5.1.2 Kalman Filtering

When solving the Bayesian state estimation problem, it is unlikely that a closed form solution will be available. To generate closed form solutions, assumptions have to be made about system and measurement models. A classical solution to the Bayesian estimation problem is the Kalman Filter. For this approach, as presented in [31, 57], the following assumptions are made about the problem:

1. The state evolution equation is linear. It is written in the form

$$x(n) = A(n-1)x(n-1) + w(n), \tag{31}$$

   where A is the state evolution matrix and $w(n)$ is zero mean, Gaussian noise with covariance Q_w.

2. The measurement is linearly related to the state of the system, or

$$y(n) = C^T(n)x(n) + v(n), \tag{32}$$

   where C is the observation matrix and $v(n)$ is zero mean, Gaussian noise with covariance Q_v.

3. Each of the noise functions $w(n)$ and $v(n)$ is independent among its own samples.

It is noted that $\hat{x}(n|i)$ is the best estimate of $x(n)$ given all measurements, $y(1)...y(i)$, up to timestep i, where $n \geqslant i$. The error between this estimate and the actual value of x at time n is given by

$$e(n|i) = x(n) - \hat{x}(n|i), \tag{33}$$

and has an associated error covariance function, $P(n|i)$. Also, the derivation is presented in discrete time following the standard literature for Kalman filters.

For the prediction step of the Kalman filter, since no new measurements are used to estimate $x(n)$, and $w(n)$ is a zero mean process, the state transition matrix gives the best approximation of x,

$$\hat{x}(n|n-1) = A(n-1)\hat{x}(n-1|n-1). \tag{34}$$

The covariance of the error function, $e(n|n-1)$, assuming that the noise is uncorrelated with error, is given by

$$P(n|n-1) = A(n-1)P(n-1|n-1)A^H(n-1) + Q_w(n). \tag{35}$$

For the update step, an additional measurement is used to improve the estimate of the state, $\hat{x}(n|n-1)$. With the constraints that $\hat{x}(n|n)$ is unbiased ($E[e(n|n)] = 0$) and that it minimizes the mean-squared error ($E[||e(n|n)||^2]$), it can be shown that [31]

$$\hat{x}(n|n) = \hat{x}(n|n-1) + K(n) \cdot [y(n) - C(n)\hat{x}(n-1|n-1)], \tag{36}$$

where $K(n)$ is the Kalman gain at time n. The Kalman gain is

$$K(n) = P(n|n-1)C^H(n) \cdot [C(n)P(n|n-1)C^H(n) + Q_v(n)]^{-1}, \tag{37}$$

where the complete derivation is found in [31, 57]. Finally, the error covariance update is

$$P(n|n) = [I - K(n)C(n)]P(n|n-1). \tag{38}$$

These equations provide a conceptually easy way to implement the Bayesian solution for the linear problem. For this study, however, neither the system model nor measurement model are expected to be linear. To use a Kalman filter-related approach, additional approximations have to be made regarding the models, such as model linearization.

5.1.3 Extended Kalman Filtering

The approach with extended Kalman filtering (EKF) is to linearize both of the models locally around the current estimate of the state, removing the nonlinearity of the models

[31]. Compared to the models of the Kalman filter, shown in Eqs. (31) and (32), the state transition function, A, and observation function, C, depend on $x(n)$, the state at time n, or

$$x(n) = A(x(n-1), n-1) + w(n-1). \tag{39}$$

$$y(n) = C^T(x(n), n) + v(n). \tag{40}$$

The noise processes, v and w, are the original zero-mean Gaussian noise terms.

To linearize these models, both are expanded with a Taylor series, where it is assumed that the first order terms will be sufficient for the approximation. A Jacobian of A and C, which captures the first order terms of a Taylor expansion, is formed, where the Jacobian is given by

$$\frac{\delta F}{\delta x} = \begin{bmatrix} \frac{\delta F_1}{\delta x_1} & \frac{\delta F_1}{\delta x_2} & \cdots & \frac{\delta F_1}{\delta x_p} \\ \frac{\delta F_2}{\delta x_1} & \frac{\delta F_2}{\delta x_2} & \cdots & \frac{\delta F_2}{\delta x_p} \\ \vdots & & & \\ \frac{\delta F_q}{\delta x_1} & \frac{\delta F_q}{\delta x_2} & \cdots & \frac{\delta F_q}{\delta x_p} \end{bmatrix}. \tag{41}$$

Using the linearized models from the Jacobian, the procedure can be summarized in two steps. The prediction step is

$$\hat{x}(n|n-1) = A(\hat{x}(n-1|n-1), n-1), \tag{42}$$

$$P(n|n-1) = A_{n-1}P(n-1|n-1)A_{n-1}^H + Q_w(n), \tag{43}$$

where A_{n-1} is defined as

$$A_{n-1} = \left.\frac{\delta A(x, n-1)}{\delta x}\right|_{x=\hat{x}(n-1|n-1)}, \tag{44}$$

and $P(n|n-1)$ is defined to be the error covariance estimate of the Gaussian process.

The update step is

$$\hat{x}(n|n) = \hat{x}(n|n-1) + K(n) \cdot [y(n) - C(\hat{x}(n-1|n-1), n)], \tag{45}$$

$$P(n|n) = [I - K(n)C_n]P(n|n-1), \tag{46}$$

$$K(n) = P(n|n-1)C_n^H \cdot [C_n P(n|n-1)C_n^H + Q_v(n)]^{-1}, \tag{47}$$

where C_n is defined as

$$C_n = \frac{\delta C(x,n)}{\delta x}\bigg|_{x=\hat{x}(n|n-1)}. \tag{48}$$

The remaining topic in regards to the EKF approach is the extent of the nonlinearity of the associated system and measurement models. Given that the EKF framework requires a Taylor series expansion of the models, it is necessary that the nonlinear models be differentiable over the entire domain of the state variable to ensure that the Jacobians of A and C exist. Care must be taken in the implementation of any EKF framework so that the models are indeed differentiable.

5.1.4 Unscented Kalman Filtering

Another method that can be used with nonlinear models is the unscented Kalman filter. The EKF requires the linearization of the models using a Taylor expansion. For highly nonlinear models (i.e., nondifferentiable), this approach is limited as the linearization does not capture the necessary dynamics of the models. The unscented Kalman filter distills the model dynamics with a set of sigma points, which capture the dynamics more accurately than what is possible with a Taylor series expansion [58]. The basic idea with this approach is to create a set of points, called sigma points, and send these points through the nonlinear model to estimate the mean and covariance of the model. As opposed to a Monte Carlo approach, the points are not randomly taken, but are chosen according to a specific, deterministic algorithm, given in [58]. Once the estimate of the mean and covariance have been determined, the traditional Kalman filter steps for update and prediction are used. For highly nonlinear systems, this approach outperforms the EKF in both ease of implementation and accuracy, however, the approach is limited as with all Kalman filter approaches in that it requires the noise distributions to be largely Gaussian. For the case of well-behaved systems, the unscented Kalman filter is comparable to the EKF, where the EKF is more intuitive in its implementation.

5.1.5 Particle Filtering

Particle filtering is a broad label for several Bayesian approaches for state estimation using sequential Monte Carlo methods for on-line learning. As with the EKF approach, the goal is to estimate a state variable, $x(n)$, given measurements, $y(n)$. Using the Bayesian state estimation assumptions, the state evolution distribution is assumed to be a first-order Markov process and the noise terms are required to be identically distributed and independent. The Kalman filter solution is simply a subset of the more general particle filter approach, where the distributions are modeled with linear functions and both noise terms are Gaussian.

As with the Kalman filter approximations, it is necessary to approximate the posterior and prior distributions. These approximations are accomplished using a Monte Carlo-based solution, where numerous derivations exist in the literature. An example is the sequential importance sampling algorithm, which is discussed in detail in [59, 60]. The key idea is to represent the required posterior density function by a set of random samples with associated weights and to compute estimates based on these samples and weights. It is an iterative process for randomly sampling the distribution, computing the relative importance of each sample, and then resampling the distribution using the most important samples. As the number of samples, or particles, becomes very large, this Monte Carlo characterization becomes an equivalent representation to the usual functional description of the posterior and prior pdf, and the particle filter approaches the optimal Bayesian estimate. Once the estimate of the distributions is generated, the Bayesian state estimation approach described before can be used to estimate the state variable.

5.2 State Estimation Approach for SHM Framework

The approach for the presented SHM framework is to use the EKF to approximate the optimal Bayesian solution. The reason for using this methodology is that prior experience has shown that the expected models for the state evolution and measurement technique are nonlinear, but are continuous and differentiable. Further, it is expected that the noise terms

are close to being Gaussian. Of the described techniques, the EKF framework provides the most direct solution for dealing with well-behaved nonlinear models with Gaussian noise terms. A flowchart of the interaction between the nonlinear models is given in Figure 23, highlighting the method for estimating the state of the system from the previous state estimate and a new measurement, $R(n)$.

5.3 Numerical Example

As an illustrative example of the EKF framework described in Section 5.1.3, consider the hypothetical problem of the following well-defined system and measurement models

$$x(n+1) = A(x(n)) + w, \tag{49}$$

$$y(n) = C(x(n)) + v. \tag{50}$$

The state model, $A(x)$, is given by

$$A(x) = x^{1.15}, \tag{51}$$

and its associated noise term, w, is assumed to be a zero-mean Gaussian process with variance

$$Q_w(x) = \sqrt{x}/100. \tag{52}$$

Similarly, the observation model, $C(x)$, is given by

$$C(x) = \exp(-x^2/800), \tag{53}$$

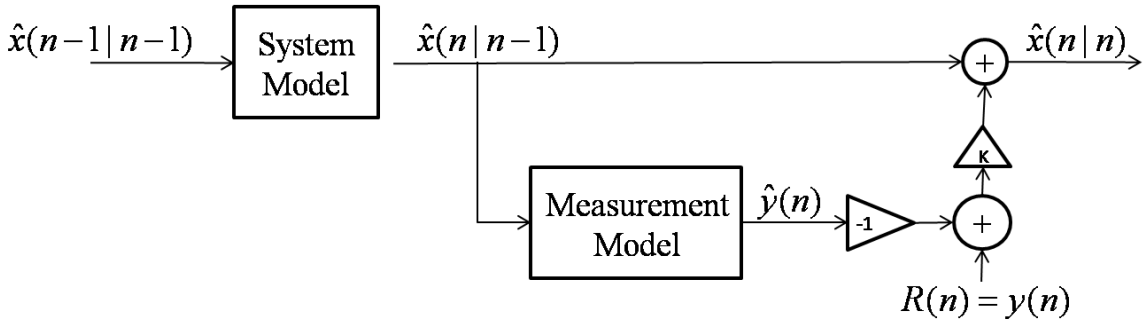

Figure 23: Illustrative flowchart of the process for updating the state estimate using an EKF.

and its associated noise term, v, is assumed to be a zero-mean Gaussian process with variance

$$Q_v(x) = x/1000. \tag{54}$$

The models $A(x)$ and $C(x)$ are obviously nonlinear, suggesting the use of an EKF approach to estimate the state, $x(n)$, given a series of measurements, $y(n)$.

A simulated series of measurements for tracking is generating using the system described. Namely, the initial value of the state is arbitrarily set to be 1.1. This value is evolved with added Gaussian noise, resulting in a simulated state variable series, $x(n)$, shown in Figure 24. This series is then input into the measurement model, $C(x)$, with the associated noise to create a simulated measurement series, $y(n)$, for tracking with the EKF framework. This series is shown in Figure 25. It can be observed that the measurement model response is actually negative at the final values because of the large amount of added Gaussian noise.

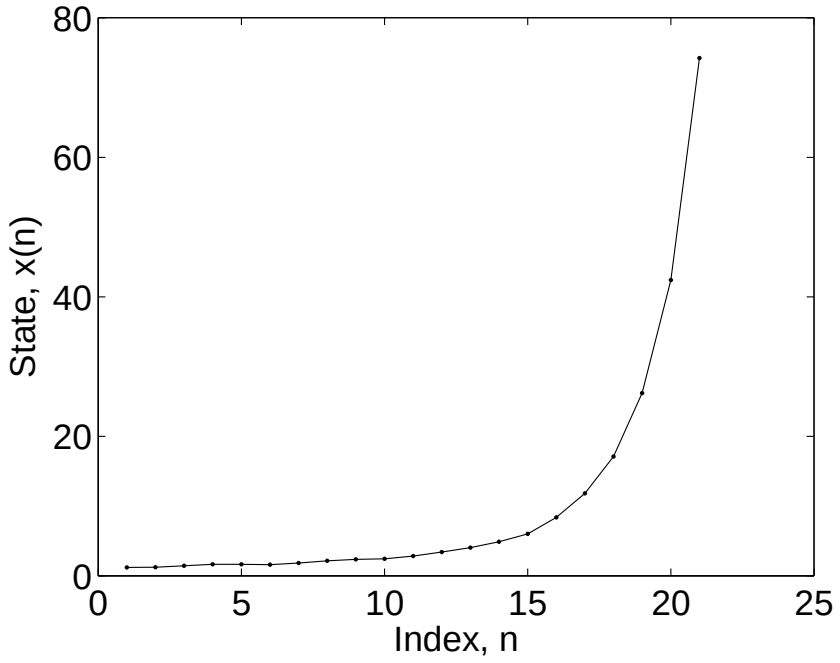

Figure 24: Example state evolution with the illustrative system model $A(x)$, where x(1) = 1.1.

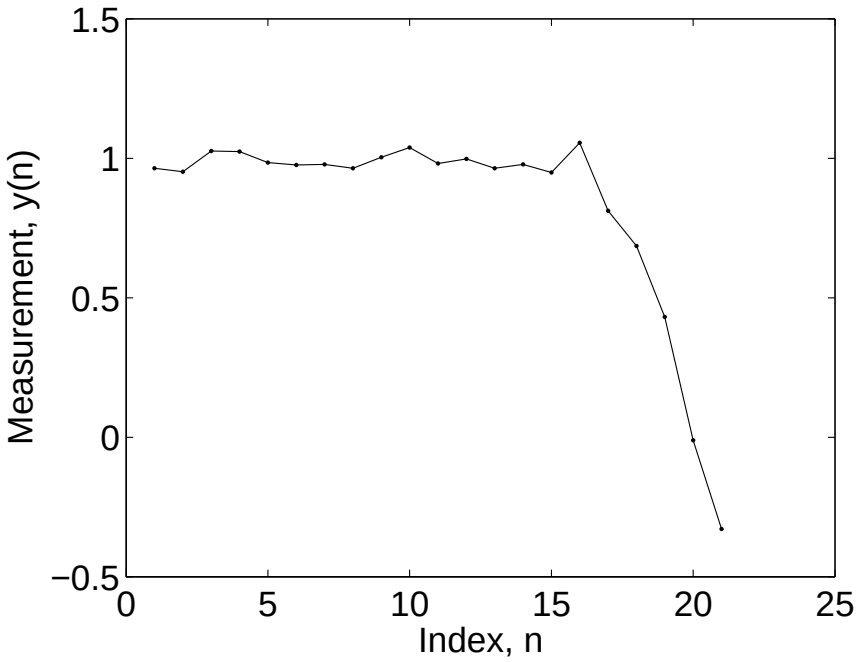

Figure 25: Measurement series response associated with Figure 24 using the illustrative measurement model, $C(x)$.

Using the EKF framework approach defined by Eqs. (39) - (48) and by initializing EKF response at index $n = 1$ as

$$\hat{x}(1) = \widetilde{C}(y(1)), \tag{55}$$

where $\widetilde{C}(y)$ is the inverse of $C(x)$

$$\widetilde{C}(y) = \sqrt{-800\ln(y)}, \tag{56}$$

the EKF estimate of the state is calculated. The response, shown in Figure 26, illustrates the output of the EKF, showing how the filter provides an approximation of the state given the extent of noise.

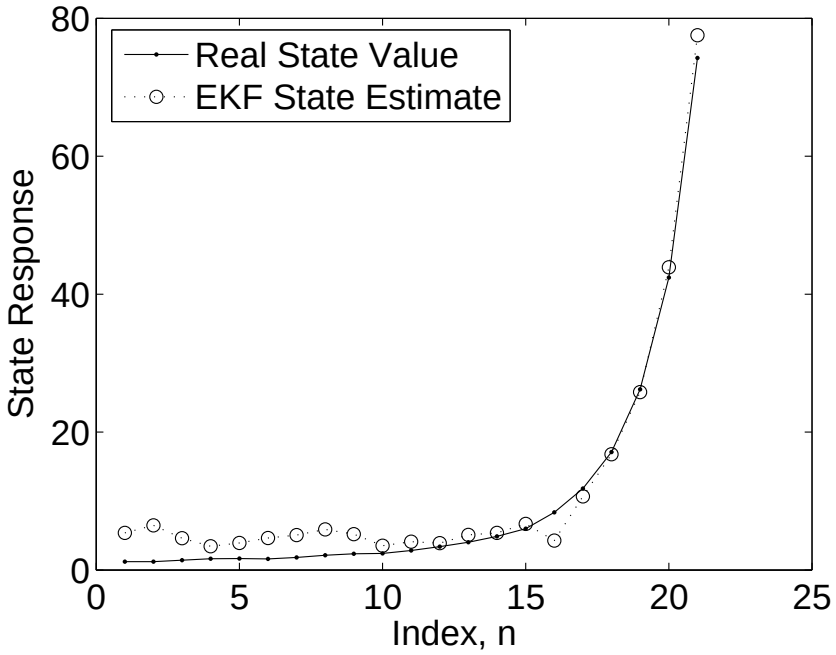

Figure 26: EKF response compared to simulated state values.

CHAPTER 6

MEASUREMENT MODEL

The focus of this chapter is to outline the methodology for relating ultrasonic measurements to crack dimensions. For the problem of interest for this thesis, the defects are small fatigue cracks (<2 mm in depth measured from the surface of the hole), and the objective is to obtain crack size estimates from the ultrasonic response from a statistically valid measurement model that can be used as part of the Bayesian approach outlined in Chapter 5. The methodology for determining the measurement model is to employ Monte Carlo methods to characterize the ultrasonic energy propagating around a fastener hole. As previously described, the ultrasonic technique is based upon cracks opening and closing under varying loads, and utilizes a ratio of ultrasonic energy from the loaded to unloaded specimen. Thus, any cracks that are present interfere with the ultrasonic wave and reduce the energy of the received signal, which is captured by the Monte Carlo method.

The wave propagation is modeled using a ray tracing approach for capturing all possible beam paths between the two transducers. First, a Monte Carlo process is used to randomly generate a large number of rays and thus characterize the received energy with no cracks and no applied load. The wave propagation model is subsequently modified to take into account the effects of external loads on cracks of varying shapes and sizes. Experiments are performed to adjust and verify the model, and a second Monte Carlo process is used to generate a large number of random crack profiles. A relationship between crack dimensions and the ultrasonic energy ratio is then determined, which is then used for crack sizing. The variance is also determined, which permits use of the measurement model for state estimation, and also allows for generation of POD curves for various detection thresholds.

The chapter is organized as follows. A brief overview of current crack sizing methodologies for both NDE and SHM is provided in Section 6.1. Section 6.2 explains the approach for the presented method for relating the ultrasonic energy ratio response to crack dimensions. The experimental process for parameter identification is discussed in Section 6.3. Results are tabulated and discussed in Section 6.4, and the models for the state estimation framework are summarized in Section 6.5.

6.1 Crack Sizing Review

The problem of fatigue cracks initiating from a fastener hole is well known because the hole acts as a stress riser and is thus a likely location for the formation of fatigue induced cracks. Although numerous studies have been performed for detection of damage in the context of SHM, there has been very little work on quantifying the damage that is detected.

There are variety of approaches for crack size determination using established ultrasonic NDE methods. The main difference between NDE and SHM methodologies is that the sensors are fixed in an SHM framework, whereas most NDE methods rely upon articulating of transducers to optimize the response. One common ultrasonic NDE sizing approach involves articulating a transducer near a defect to maximize the pulse-echo response; the estimated size is based upon the received amplitude reflected from the flaw [17]. An alternative method for sizing is to use time-of-flight measurements and relate crack sizes to wave arrival times, which are perturbed by the defect [18]. This approach is extended by Silk, where the time-of-flight diffraction technique sizes defects based on the wave propagation time difference between signals diffracted from the ends of a crack [19]. The sizing capability of these approaches is limited to crack sizes on the order of the ultrasonic wavelength or larger. A complimentary approach is given by Masserey [61] using the frequency response of the transmitted and reflected ultrasonic energy from the crack surface as measured using a laser interferometer. By examining the frequency response shift

of the reflected and transmitted pulses, combined with an analytical expression for the center frequency shift as a function of crack depth, it is possible to size defects much smaller than the incident wavelength. None of these techniques, however, are directly applicable to fastener hole monitoring because of the fixed transducer positions.

For the inspection of fastener holes, typically there is access from only one surface and the fastener is installed in the hole. Sargent [62] proposed an immersion approach using two transducers in a through-transmission configuration; defects are detected using the shadow from the crack rather than a direct reflection. Ihn and Chang [63] present a combined eddy current and Lamb wave approach using a distributed network of sensors mounted around a repaired fastener hole. This technique is able to detect large surface breaking defects within a POD framework, but is not extended to sizing. Lee and Tsuda [20] present a surface wave monitoring method using piezoelectric fiber wave guides placed at varying distances from the fastener hole surface for sizing surface breaking defects. Nagy et al. [10] consider the similar problem of cracks originating from weep holes in fuel tanks using circumferential creeping waves generated by an incident shear wave. This technique offers excellent crack detection, localization, and the potential for sizing of smaller cracks. However, transducer access requirements prevent its direct application to the fastener hole problem.

It is well known that residual stresses compress the crack surfaces and can completely close cracks, reducing the effectiveness of most ultrasonic techniques that rely on larger, open cracks [64]. Rehbein et al. [65] utilize a multi-frequency through-transmission scanning technique combined with a distributed spring model to determine the length of a partially closed crack. Ahmed and Saka [66] propose scanning with a slightly off-angle longitudinal beam to detect small closed cracks. Typically, the closed cracks require load modulation of the specimen to sufficiently open them for detection. Harri et al. [16] propose monitoring cracking during the fatigue process using a multi-sine excitation approach, where the statistical variations of the ultrasonic response to different discrete frequencies

are related to crack size. Cook and Berthelot [67] employ surface waves for *in situ* detection of small surface breaking cracks in steel. Their technique correlates the change in the amplitude of the backscattered signal with the size of the crack, where the sample is loaded to 80% of the maximum load. Kim and Rokhlin [14] apply surface waves to *in situ* sizing of cracks originating from a cavity by modeling the modulation of the ultrasonic reflection from the crack with load. Yan and Nagy [13] extend their work using thermal expansion to open the defects for characterization.

6.2 Methodology

The focus of this section is to present a methodology for estimating the expected ultrasonic energy ratio given the geometry of one or more fatigue cracks originating from a fastener hole. This methodology, which requires additional insight into the wave propagation around the cylindrical hole surface both with and without a crack, forms the basis for the crack sizing strategy. For the development of the measurement model, a "Center Peaked" transducer configuration is assumed. A Monte Carlo approach is taken for modeling the received energy as the sum of the contributions from both sides of the hole. Using this approach, an energy density expression in the plane of expected crack growth through the center of the hole is developed assuming no external loading; the received energy when there are no cracks is assumed to be proportional to the total energy. The effects of externally applied loads, namely acoustoelasticity and Poisson's effect, are then included in the energy density formulation. Next, the effect of cracks, which open under load and block a portion of the received energy, is considered by the energy density expression. Energy ratios can thus be calculated for actual crack profiles and compared to experimentally measured values. A second Monte Carlo approach is taken to randomly generate a large number of crack profiles so that the received energy can be related to crack dimensions, producing both the measurement model, $R = C(x)$, for the EKF and also an inverse measurement model, $x = \widetilde{C}(R)$. Further, the variance of the crack size estimates can be quantified based

on the statistics of the Monte Carlo process and combined with the energy ratio statistics during the fatigue process to create an expression for the measurement model variance for the EKF. Refer to Figure 27 for a description of the development of the measurement models.

6.2.1 Monte Carlo Approach to Ultrasonic Modeling

The statistical approach for modeling the ultrasonic energy density around a hole is a modified ray-based method whereby a large number of randomly generated ray paths are combined to form an aggregate energy density. The multiple ray paths shown in Figure 28(a) illustrate this idea; the rays simulate the beam spread of the transducers. Consider the i^{th} ray propagating at a fixed frequency between the transducers, as illustrated by the bold ray path in the figure; this ray intersects the apex of the hole at a specific y position. This position, y_i, is the distance from the bottom of the hole, and identifies the position of the

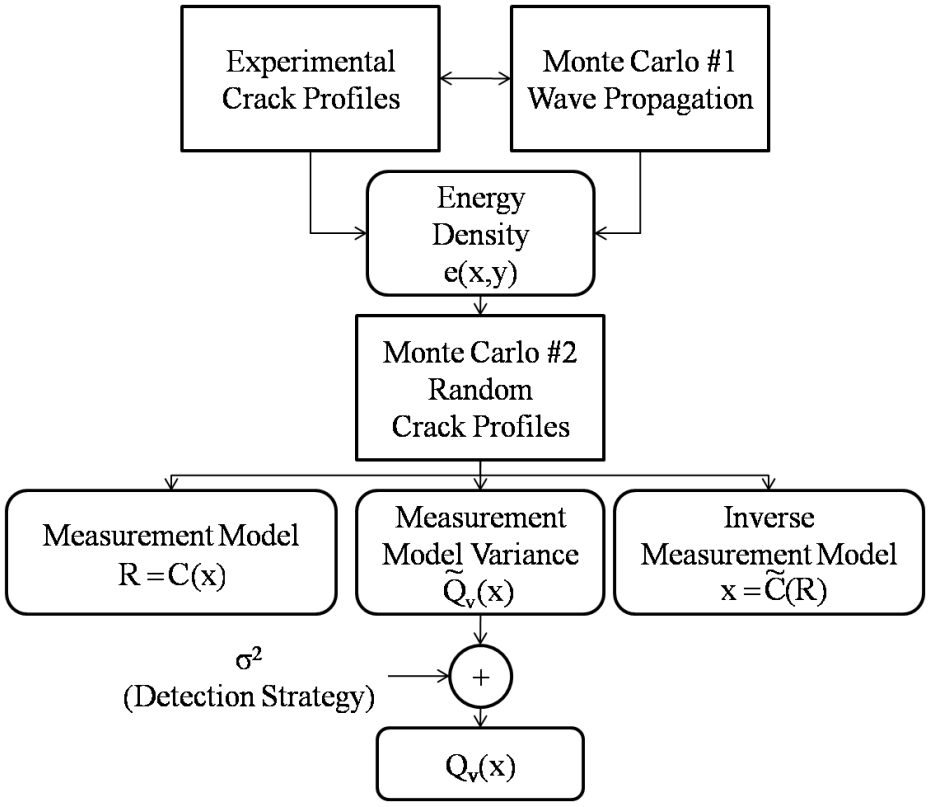

Figure 27: Illustration of the development process for the measurement models.

ultrasonic energy as it decays away from the hole surface in the z direction, as illustrated in Figure 28(b). If $E(y_i, z; f_i)$ is the normalized energy profile for the i^{th} ray at location y_i and with frequency f_i as a function of z, the distance from the surface, the effective energy profile from this ray is

$$\widetilde{E}(y_i, z; f_i) = W_T W_R E(y_i, z; f_i), \tag{57}$$

where W_T and W_R are the transmitter and receiver weights, respectively.

A Monte Carlo process is used to capture the overall distribution of energy in the yz plane cutting through the hole at the 3 and 9 o'clock positions. By dividing the y axis into N uniformly spaced regions, the overall distribution of energy is approximated by summing the individual contributions from each ray,

$$e(y_j, z) = \sum_{y_j < y_i \leq y_{j+1}} \widetilde{E}(y_i, z; f_i). \tag{58}$$

The sum is over all of the ray paths where y_i is within the j^{th} region. This energy density, $e(y, z)$, corresponds to the energy received at the receive transducer from one side of the hole, and is assumed to be the same for the other side. It should be noted that this approximation neglects all interference effects between the different ray paths (i.e., phase

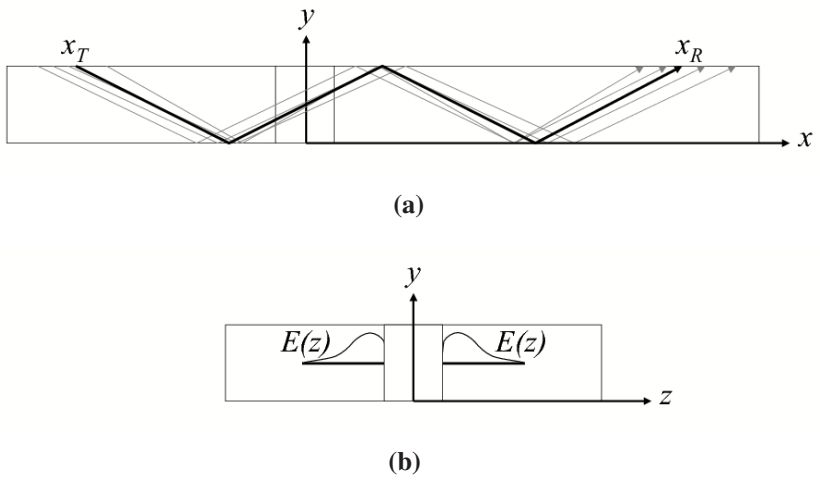

Figure 28: Illustration of energy density formulation. (a) Randomly generated rays, and (b) energy decay away from the surface of the hole.

information).

The final aspect of the energy density approach is determining the weighting parameters W_T and W_R. Each weighting parameter is affected by how close the ray path is to the spatial center of the transducer and how much energy is present at the particular frequency considered. Thus, each weight may be thought of as a product of two terms, W^G and W^F, related to geometry and frequency, respectively. Since the transducers are assumed to be identical and a single frequency is associated with each ray path, the weight corresponding to frequency must be the same for both transducers. Thus, the weight for each iteration (i.e., one ray path) is given by

$$W_T W_R = W_T^G \; W_R^G \; (W^F)^2. \tag{59}$$

6.2.1.1 Energy Decay Function, $E(z)$

Multiple ray paths are generated by the Monte Carlo simulation, and each one corresponds to a shear wave propagating at a particular refracted angle and frequency. These shear waves are incident on the surface of the hole; some of the energy is specularly reflected away from the receiver and is thus not of interest here. The energy that eventually reaches the receiver is first converted into a Rayleigh-like wave that propagates around the hole and continuously re-radiates energy as a propagating shear wave. This wave propagating along a cylindrical surface is referred to as a "leaky" wave by several authors [10, 56]. The energy that "leaks" into a shear wave aligned with the receiver is thus recorded for analysis; i.e., the received energy is assumed to be proportional to the energy contained in the leaky wave passing through the yz plane bisecting the hole.

The propagation of the leaky wave around the hole is similar to the standard Rayleigh wave propagation but with attenuation due to the radiation (leakage) of energy into the specimen as a shear wave. Following the derivations of Viktorov [68] and Rose [53] for the usual Rayleigh wave, the characteristic equation for the Rayleigh wave speed is

$$\eta^6 - 8\eta^4 + 8(3 - 2\zeta^2)\eta^2 - 16(1 - \eta^2) = 0, \tag{60}$$

where $\eta = c_R/c_T$, $\zeta = c_T/c_L$, and c_R, c_T, and c_L are the phase velocities of the Rayleigh, shear and longitudinal waves, respectively. Viktorov approximates η as

$$\eta = \frac{0.87 + 1.12\nu}{1 + \nu}, \tag{61}$$

where ν is Poisson's ratio.

The above derivation of the Rayleigh wave speed is based upon the wave propagating along a planar surface. For this application, however, a Rayleigh-like wave is propagating on the cylindrical surface of the fastener hole. Viktorov [68] presented a complete derivation of the characteristic equations for this situation, but his solution requires searching a complex wavenumber space. Here, the Rayleigh-like wave is approximated using Viktorov's derivation of the change in Rayleigh wave speed with curvature, but does not consider other curvature effects.

The basic mechanism for the curvature correction is to adjust the Rayleigh wave phase velocity by a fractional scale factor, δ,

$$c_R' = c_R(1 - \delta). \tag{62}$$

The parameter δ is given by

$$\begin{aligned}\delta = {} & \tfrac{1}{D}\left[1 + \tfrac{s_R}{q_R} + \tfrac{k_R}{2s_R}\left(1 - \tfrac{s_R^2}{q_R^2}\right)\right] e^{2\operatorname{arcth}\frac{q_R}{k_R} - 2\operatorname{arcth}\frac{s_R}{k_R}} \\ & + \tfrac{1}{D}\left[1 + \tfrac{s_R}{q_R} + \tfrac{k_R}{2s_R}\left(1 - \tfrac{s_R^2}{q_R^2}\right)\right] e^{-2\operatorname{arcth}\frac{q_R}{k_R} + 2\operatorname{arcth}\frac{s_R}{k_R}} \\ & - \tfrac{1}{D}\tfrac{2s_R^2}{k_t^2}\left(\tfrac{k_t^2}{k_l^2} - 1\right),\end{aligned} \tag{63}$$

where

$$\begin{aligned}D = k_R R_c \Bigg[& \left(1 - \tfrac{s_R}{q_R}\right)\left(e^{2\operatorname{arcth}\frac{q_R}{k_R} - 2\operatorname{arcth}\frac{s_R}{k_R}} - e^{-2\operatorname{arcth}\frac{q_R}{k_R} + 2\operatorname{arcth}\frac{s_R}{k_R}}\right) \\ & + \tfrac{4k_R s_R}{k_t^2}\left(\tfrac{k_t^2}{k_l^2} - 1\right)\Bigg],\end{aligned} \tag{64}$$

and,

$$r_R = \sqrt{4 s_R q_R}, \quad q_R = \sqrt{k_R^2 - k_L^2}, \quad s_R = \sqrt{k_R^2 - k_T^2}. \tag{65}$$

The arcth(z) function is defined as

$$\operatorname{arcth}(z) = \frac{1}{i}\cot^{-1}(-iz). \tag{66}$$

The parameter R_c in Eq. (64) is the radius of curvature and $k_i = 2\pi f/c_x$ for $x = R, L, T$. Aldrin further expanded this derivation to include the effect of the angle of incidence on the effective surface curvature [56],

$$\hat{R}_c = \frac{R_c}{\cos^2(\frac{\pi}{2} - \theta)}, \tag{67}$$

where R_c is the actual hole radius, $\hat{R}_c$ is the effective radius of curvature, and θ is the incident angle. Thus, the dependence of the Rayleigh wave velocity on a cylindrical surface can be calculated. Figure 29 illustrates the change in the speed of a 5 MHz Rayleigh wave as a function of propagation angle for a 4.82 mm diameter hole using the values for the shear and longitudinal wave speeds of 7075-T651 aluminum given in Table 1 of Chapter 3.

Following Rose [53], it is possible to express the z component of displacement as a function of distance z away from the hole surface in terms of the shear, longitudinal and Rayleigh wave speeds. This displacement is given as

$$u_z(x, z, t) = q_R(r_R e^{-q_R z} - 2e^{-s_R z}) \sin[k_R(x - c_R t)]. \tag{68}$$

Here x is the direction of propagation and z is normal to the propagation surface. By taking

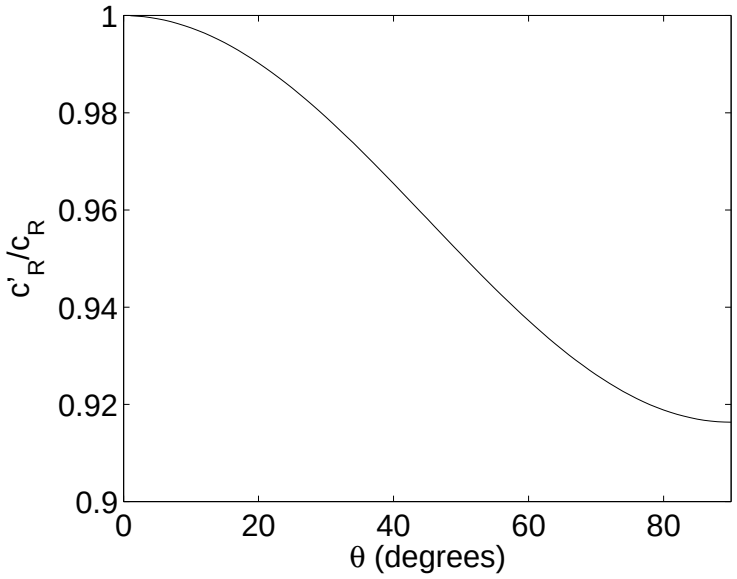

Figure 29: The effect of angle of propagation (θ) on the velocity of a 5 MHz Rayleigh wave propagating on the surface of a 4.82 mm diameter hole.

the peak value of u_z away from the hole surface,

$$\bar{u}_z(z) = q_R(r_R e^{-q_R z} - 2e^{-s_R z}), \tag{69}$$

and combining this result with the strain-energy definition given by Achenbach [69], the concentration of ultrasonic energy as a function of z is given by

$$E(z) = \frac{\lambda}{2}[\bar{u}_z(z)]^2, \tag{70}$$

where λ is a Lamé constant. Thus, an expression for the Rayleigh wave energy decay as a function of distance from a cylindrical surface can be computed. Examples are shown in Figure 30 for several different frequencies of interest .

6.2.1.2 Geometric Weighting

Each iteration of the Monte Carlo process randomly creates a ray by generating the two position variables, x_T^r and x_R^r, which define the x coordinates of the transmission and reception points, respectively, where the r superscript denotes their random nature. Rather than

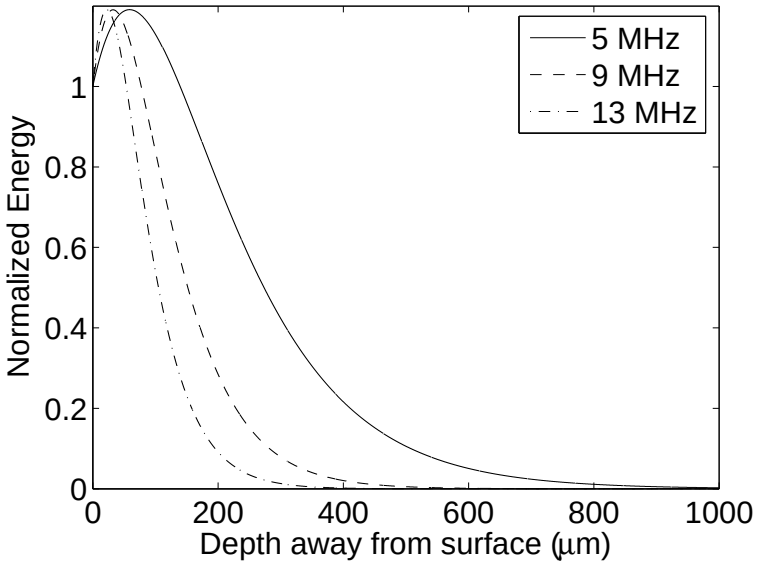

Figure 30: Rayleigh wave energy decay with depth for various frequencies for a wave propagating in 7075-T651 aluminum.

model the transducers as point sources, it is assumed that each transducer has a finite footprint over which ultrasound enters the material; this footprint is modeled with a Gaussian weighting function in the x direction. The center points of the transducers are x_T and x_R, which are the nominal mounting locations x_1 and x_2, respectively, from Eqs. (15) and (17). Thus, the Gaussian distributions have known means of x_T and x_R. Since the transducers are assumed to be identical, the standard deviations of the two Gaussian functions are the same unknown variable σ_x. The weighting terms W_T^G and W_R^G are thus given by

$$W_T^G = \frac{1}{\sigma_x \sqrt{2\pi}} e^{-\frac{(x_T^r - x_T)^2}{2\sigma_x^2}} \quad \text{and} \quad W_R^G = \frac{1}{\sigma_x \sqrt{2\pi}} e^{-\frac{(x_R^r - x_R)^2}{2\sigma_x^2}}. \tag{71}$$

Rather than applying the weights W_T^G and W_R^G directly, they are used as pdfs for picking the ray path endpoints x_T^r and x_R^r as a part of the Monte Carlo generation of large numbers of rays.

6.2.1.3 Frequency Weighting

Received signals are broadband since they are generated using an impulsive excitation. When operating in a pitch-catch configuration, the frequency response of the received ultrasonic pulse is centered at approximately 9 MHz, and the measured bandwidth (where the noise ceiling is 15 dB down) is from 4.4 MHz to 13.2 MHz. The measured frequency response from a direct through-transmission arrival (no hole present) is shown in Figure 31, and the best Gaussian fit to this spectrum has a mean, $\overline{f}$, and standard deviation, σ_f, of 9.04 MHz and 1.45 MHz, respectively; this Gaussian function is also shown in the figure for comparison. For each iteration of the Monte Carlo process, the frequency for the ray being propagated is randomly selected from a uniform distribution between 3 and 15 MHz, and the frequency weighting, W^F, for the ray is given by this best fit Gaussian function.

6.2.2 Load Effects

The energy density generated from the Monte Carlo approach as summarized in Eq. (58) neglects the beam path and wave speed changes caused by applied loads. The beam path is

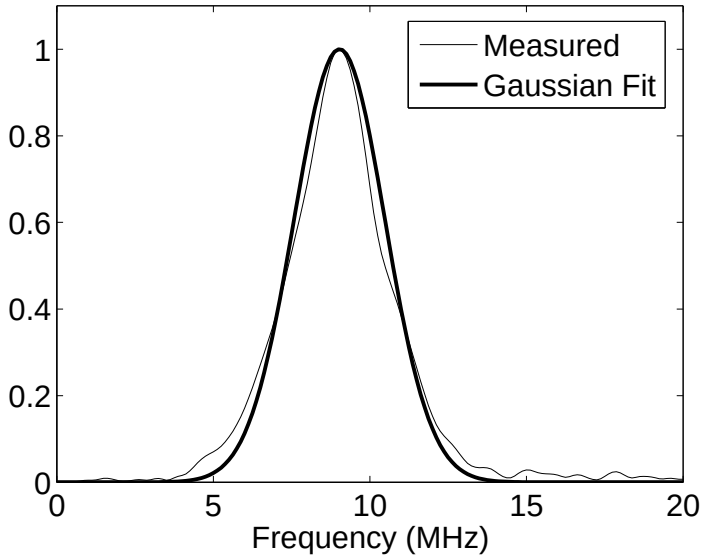

Figure 31: Comparison between the measured transducer frequency response and the Gaussian fit.

perturbed because of geometry changes, and the wave speeds are changed because of the acoustoelastic effect. The consequences of both changes are analyzed here.

6.2.2.1 Geometry Effects

The uniaxial loading from the fatigue spectrum results in an elongation of the specimen in the loading direction and a contraction in the perpendicular directions (Poisson effect). For the purposes of this study, the local effects of plastic deformation around the hole are ignored. The change in specimen geometry results in different values for the transducer positions x_T and x_R and specimen thickness h. These geometrical changes shift the energy along the surface of the hole in the y direction and thus affect the overall energy response.

Following the derivation by Bao et al. [43], if ϵ is the strain in the direction of loading, changes in transducer mounting positions x_T and x_R are given by $\Delta x_T = \epsilon x_T$ and $\Delta x_R = \epsilon x_R$, resulting in a greater separation between the two transducers. Poisson's ratio, ν, determines the change in specimen thickness, which is $\Delta h = -\epsilon \nu h$, where the negative sign indicates

the contraction transverse to the loading direction. By defining x'_R, x'_T and h' as the strain-affected variables, the new refracted angle for this iteration is

$$\theta' = \arctan\left(\frac{x'_R - x'_T}{4h'}\right). \tag{72}$$

If the transducers are mounted such that the center of the ultrasonic energy is propagating at the optimal refracted angle, then this shift in angle will result in a loss of energy at the receiver since there will be a mismatch between the optimal and actual refracted angles.

6.2.2.2 Acoustoelastic Effects

The acoustoelastic effect refers to the change in acoustic wave velocities in a material as a function of applied stress. The theory of acoustoelasticity is based on a continuum theory of small disturbances superimposed on an elastically deformed body. There is a long history of theoretical and experimental work on acoustoelasticity with an early version of the modern theory developed by Hughes and Kelly in 1953 [70]. For a specific experiment, an acoustoelastic constant K is defined that linearly relates the change in wavespeed c to applied stress σ,

$$\frac{\Delta c}{c} = K\sigma. \tag{73}$$

The constant K is dependent upon the specific wave mode, propagation direction, and stress orientation, and is a function of second and third order elastic constants.

Consider a coordinate system with the x axis aligned along the direction of propagation of the shear wave. Of interest for this work are both vertically polarized shear waves (SV waves) and longitudinal waves (L waves) since they determine the Rayleigh wave speed. For both SV and L waves, it is assumed that the wave propagates in a uniaxial stress field, neglecting the stress concentration in the vicinity of the hole. The resulting form of K for both waves is [43]

$$\frac{\Delta c}{c} = [K_1 \sin^2(\theta) + K_2 \cos^2(\theta)]\sigma = K(\theta)\sigma, \tag{74}$$

where θ is the refracted angle, and K_1 and K_2 are functions of the second and third order elastic constants, listed in Table 1. It can be seen that K_1 is the acoustoelastic constant

for the wave propagating in the direction of applied stress ($\theta = 90°$), and that K_2 is the acoustoelastic constant for the wave propagating perpendicular to the direction of applied stress ($\theta = 0°$). For the SV wave, expressions for K_1 and K_2 are [43]

$$K_1^{SV} = \frac{4\mu(\lambda+\mu) + \mu m + \frac{1}{4}\lambda n}{2\mu^2(3\lambda+2\mu)}, \tag{75}$$

$$K_2^{SV} = \frac{\mu(\lambda+2\mu) + \mu m + \frac{1}{4}\lambda n}{2\mu^2(3\lambda+2\mu)}, \tag{76}$$

with the SV superscript denoting the SV wave. Using the values in Table 1 for the elastic constants, the values for K_1^{SV} and K_2^{SV} are $-1.57\text{x}10^{-11}$ Pa and $-3.458\text{x}10^{-11}$ Pa, respectively.

The expressions for K_1 and K_2 for the longitudinal wave acoustoelastic effect are derived by Muir et al. [71], and are

$$K_1^{L} = \frac{4\lambda^2 + 15\lambda\mu + 10\mu^2 + 2l\mu + 4m\lambda + 4m\mu}{2\mu(3\lambda+2\mu)(\lambda+2\mu)}, \tag{77}$$

$$K_2^{L} = \frac{-\lambda^2 - 2\lambda\mu - m\lambda + l\mu}{\mu(3\lambda+2\mu)(\lambda+2\mu)}, \tag{78}$$

where the superscript L denotes the longitudinal wave. Using the values in Table 1 for the elastic constants, the values for K_1^L and K_2^L are $8.4107\text{x}10^{-11}$ Pa and $-6.2882\text{x}10^{-11}$ Pa, respectively.

The most obvious consequence of the acoustoelastic effect is an overall time shift in received signals; that effect is not of interest here since it does not affect the received energy. The importance of the acoustoelastic effect here is its effect on the energy decay away from the hole, which is estimated by considering changes in the Rayleigh wave speed. As shown in Section 6.2.1.1, the Rayleigh wave speed, c_R, is determined by the η parameter and the shear wave speed. By including the acoustoelastic effect, an expression for the speed of a Rayleigh wave in a stressed medium propagating along the surface of the hole at an angle θ is given by

$$c_R = \eta[c_T(1 + K(\theta)\sigma)], \tag{79}$$

where the shear wave speed, c_T, is that of the unloaded specimen. As outlined in Eqs. (60) through (70), the Rayleigh wave energy decay away from the hole depends on the shear, longitudinal and Rayleigh wave speeds. Thus, for a given direction of propagation, changes in c_R, c_T, and c_L caused by the external loading result in different decay profiles for the ultrasonic energy.

6.2.3 Calculated Energy Ratio

To approximate the effect of cracks on the energy density, the approach is to assume that fatigue cracks block the transmission of all ultrasonic energy incident on the cross-sectional area of the open crack. It is initially assumed that the cracks are fully opened with the reference loading of 10,000 lbs. It is also assumed that with no tensile loading, the residual stresses around the crack surfaces will press the crack surfaces together, effectively closing the crack and enabling complete transmission of the incident energy. This assumption is valid for the small cracks considered here, but very large cracks remain partially open when the load is removed.

To calculate the energy ratio response associated with a given open crack geometry, two energy integrals are calculated [47]. The first is the received energy associated with the unloaded specimen, which is taken to be the maximum energy possible. The unloaded response at the receiver is given by

$$E_{unloaded} = \int_{G_1} e_1(y,z)\mathrm{d}A + \int_{G_2} e_2(y,z)\mathrm{d}A = 2\int_{G} e(y,z)\mathrm{d}A, \tag{80}$$

where G_1 and G_2 define the specimen geometry on the two sides of a single hole and $e_1(y,z)$ and $e_2(y,z)$ are the energy density expressions for the two sides of the crack under no external loading. It is also assumed that the energy densities and areas of integration are the same for both sides of the hole.

A second energy integral corresponds to the loaded specimen, where it is assumed that the applied stress is sufficient to fully open any cracks present. The energy that arrives at the receive transducer is determined by reducing the unloaded energy, $E_{unloaded}$, by the

energy blocked by the cracks,

$$E_{loaded} = E_{unloaded} - \int_{H_1} e(y,z)dA - \int_{H_2} e(y,z)dA, \tag{81}$$

where H_1 and H_2 define the open crack areas on each side of the fastener hole. Following the experimental methodology of Section 3.2.1, the calculated energy ratio values are determined from the ratio of the loaded energy to the unloaded energy, or

$$R'_{calc} = \frac{E_{loaded}}{E_{unloaded}}. \tag{82}$$

This value is subsequently normalized by

$$R_{calc} = \frac{R'_{calc}}{R'_{nocrack}}, \tag{83}$$

where $R'_{nocrack}$ is defined as with R'_{calc} except the crack areas H_1 and H_2 are zero.

6.2.4 Monte Carlo Approach to Crack Sizing

To enable crack sizing using the measured energy ratio, it is necessary to have a measurement model that relates a given energy ratio response to a crack dimension such as length, depth, or area [72]. A second Monte Carlo process is implemented to generate a large number of crack profiles, and the resulting energy ratios are calculated based upon the energy density of Eq. (58). The mean energy ratio as a function of a crack dimension is interpolated for crack sizing.

Each iteration of this Monte Carlo process creates a separate random crack profile for each side of the hole. The crack profiles are formed through the union of half ellipses, where the number of ellipses and their aspect ratios, depths, and positions are randomly generated. The depth and aspect ratio distributions are defined as uniform random variables. The range of depths is from 0 mm to 3.0 mm, where the upper bound is set based on observations of the maximum crack size that still allowes the crack to completely close under no load. The range of aspect ratios is from two to four where the aspect ratio is the ratio of crack surface length to depth. Thus, an aspect ratio of two corresponds to a

semi-circular crack. A Gaussian distribution is used for the crack position (in the thickness direction, y), with a mean of $h/2$ and standard deviation of 800 μm. The distribution for the number of cracks is set to be consistent with observations of a large number of fatigued specimens and is shown in Figure 32. Note that some crack combinations were rejected as being physically unlikely, such as a large crack on one side of the hole and no crack on the other.

6.3 Experimental Model Determination

The remaining step for defining the energy density is to estimate the parameter σ_x related to the size of the transducer beamspread, based on experimental data. Following the procedures of Chapter 3, a series of eight two-hole coupons were fatigued and monitored ultrasonically. As with the model assumptions, a "Center Peaked" configuration was used for the transducer mounting. The fatigue process consistently resulted in detectible cracking around a single hole with no evidence of cracking on the other, yielding a total of eight data points. Each of the specimens was fatigued to a predefined stop condition based on

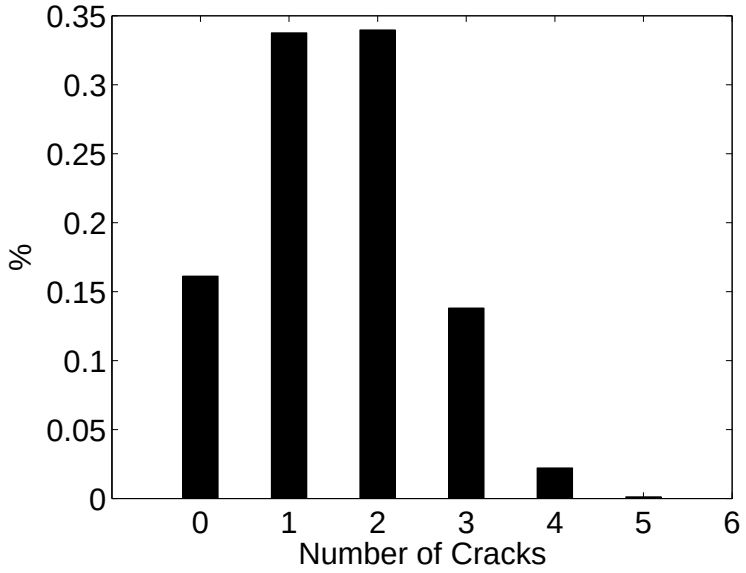

Figure 32: The distribution assumed for the number of cracks on each side of the hole when generating random crack profiles.

the drop in energy ratio. The intent was to obtain a variety of final crack sizes for estimating σ_x. Since the focus of this work is small crack performance, energy ratio drops of less than 50% are desired. Table 7 summarizes the final energy ratio measurement for each experiment, along with the final crack dimensions. It should be noted that the energy ratio curves before detection can exhibit small upward or downward slopes; an example of slight upward slope is shown in Figure 33. This trend is corrected by re-normalizing the energy ratio response given in Eq. 14 by $R(n_1)$, where n_1 is the number of fatigue cycles just prior to detectible damage.

6.3.1 Model Parameter Determination

The approach for estimating σ_x was to first digitize the final crack profiles from the eight holes with cracks. Any isolated cracks with depths less than 100 μm, which is smaller than half of the wavelength of a 10 MHz Rayleigh wave, were excluded from consideration. The primary reason for not considering cracks with depths less 100 μm was that it was

Table 7:

Measured energy ratios and crack dimensions.

Hole #	R	Location	Cum. Length (mm)	Max. Depth (mm)	Area (mm^2)
1	0.664	Outboard	3.14	0.465	1.026
		Inboard	3.42	0.433	1.065
2	0.631	Outboard	2.77	0.644	1.150
		Inboard	3.60	0.247	1.300
3	0.525	Outboard	2.43	0.666	1.143
		Inboard	3.22	0.581	1.253
4	0.716	Outboard	3.15	0.646	1.396
		Inboard	3.54	0.234	3.028
5	0.549	Outboard	2.65	1.265	2.500
		Inboard	4.38	0.503	3.028
6	0.864	Outboard	2.16	0.325	0.473
		Inboard	2.37	0.114	0.493
7	0.916	Outboard	0.22	0.116	0.021
		Inboard	0.54	0.514	0.058
8	0.878	Outboard	1.04	0.364	0.280
		Inboard	1.24	0.177	0.291

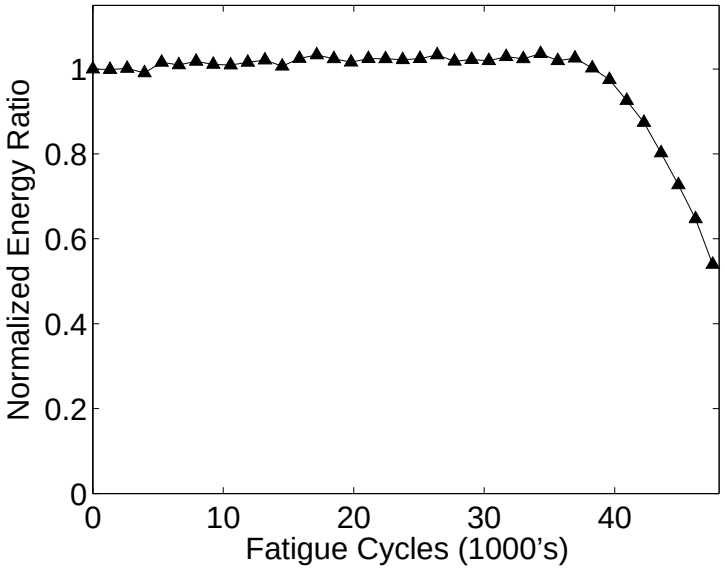

Figure 33: Energy ratio curve from hole #3, exhibiting a slight upward slope in the energy ratio curve before detection.

not possible to consistently identify such small defects given the resolution of the digitized crack images. Also, while a significant portion of the ultrasonic energy is within 100 μm of the hole surface, experience applying the ultrasonic monitoring strategy has shown an inability to detect isolated cracks with depths smaller than 100 μm.

Energy ratios are calculated as described in Section 6.2.3 using the measured crack profiles as the H_1 and H_2 areas of Eq. (81). The calculated energy ratios are compared to the measured energy ratios, and the σ_x yielding the minimum mean of the absolute errors is selected via an exhaustive search. The search in σ_x did not yield a true minimum, but as σ_x increased, the error decreased steadily and then leveled off at σ_x = 4.83 mm, which is taken as the final value. This is shown in Figure 34. This value is somewhat larger than expected, given that the transducer length is about 10 mm axially, in the direction of fatigue loading. A likely explanation is that the Gaussian assumption for the weighting is not correct; the actual distribution is most likely skewed because of the wedge and cannot have the long tails of a Gaussian. Regardless, this σ_x is reasonable because most of the area of the Gaussian falls within the transducer footprint.

Referring to the second and third columns of Table 8, the measured and calculated energy ratios can be compared. The mean absolute error is 0.060 with a standard deviation of 0.044 and maximum error of 0.15, and there is a small but significant overall negative bias; i.e., the calculated energy ratios are, on average, lower than the measured values. A plausible explanation for this bias is related to the assumption that cracks are fully open under load. Specifically, the energy ratio calculations assume that the cracks completely block transmission of the ultrasonic energy over their entire surfaces. In reality, the crack surfaces are not completely separated, even under load, particularly near the constrained crack boundaries. To approximate this effect, each discrete crack shape is slightly down-scaled before calculating the energy ratio response. For a crack profile of $g(y)$, beginning at $y = 0$ with total length L, the scaled crack profile, $g'(y)$, is

$$g'(y) = A(y;\alpha) \cdot g(y), \tag{84}$$

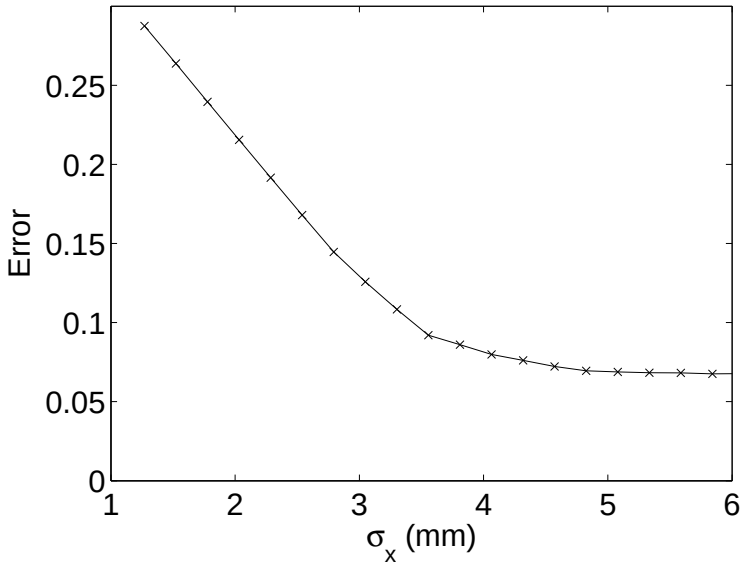

Figure 34: Measurement errors associated with various values of σ_x.

Table 8:

Comparison of measured and calculated energy ratios.

Hole Number	Energy Ratio (Measured)	Energy Ratio (Calculated)	Energy Ratio (Corrected)
1	0.664	0.606	0.649
2	0.631	0.679	0.720
3	0.525	0.544	0.597
4	0.716	0.641	0.677
5	0.549	0.620	0.667
6	0.864	0.810	0.828
7	0.916	0.765	0.795
8	0.878	0.873	0.883

with $A(y;\alpha)$ defined as

$$A(y;\alpha) = \begin{cases} 0, & y < 3\alpha L/4, \\ \frac{\alpha}{2}\left[1 + \cos\left(\frac{2\pi(y-3\alpha L/4)}{\alpha L/2} + \pi\right)\right], & 3\alpha L/4 < y < \alpha L, \\ 1-\alpha, & \alpha L < y < L - \alpha L, \\ \frac{\alpha}{2}\left[1 + \cos\left(\frac{2\pi(y-L+\alpha L)}{\alpha L/2}\right)\right], & L - \alpha L < y < L - 3\alpha L/4, \\ 0, & y > L - 3\alpha L/4. \end{cases} \tag{85}$$

The parameter α is the fractional reduction in the length and depth of the crack because of closure effects; $\alpha = 0$ corresponds to the fully opened crack. It is found that $\alpha = 0.1$ removed the bias in the estimator. A measured crack profile and its numerically reduced profile are shown in Figure 35, demonstrating how a portion of the crack surface is excluded from the energy density integral. With $\alpha = 0.1$, the mean absolute error of the calculated energy ratio is 0.062 with a standard deviation of 0.045 and a maximum absolute error of 0.12; refer to the last column of Table 8. Figure 36 shows the measured, calculated and crack closure corrected energy ratios for the eight holes. The corrected energy ratio method with $\alpha = 0.1$ is used for the remainder of the paper.

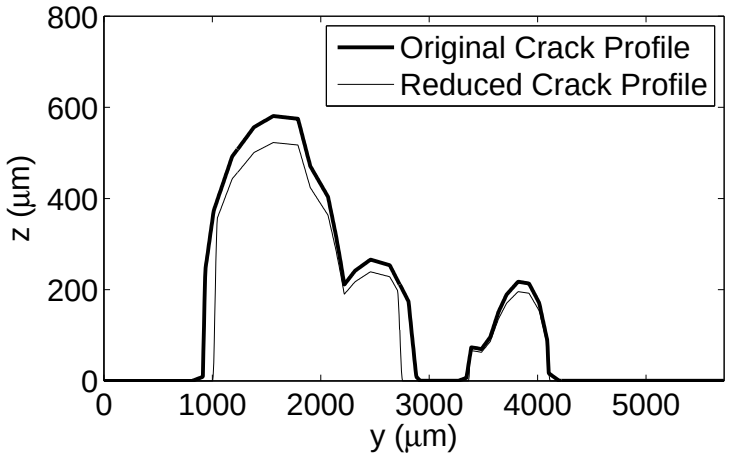

Figure 35: Actual crack profile and its numerically reduced profile to simulate crack closure effects.

6.3.2 Energy Density

The energy density for an external load of 10,000 lbs (164 MPa) is generated using σ_x=4.83 mm with 1.5 million iterations, where each iteration corresponds to a random ray path. The resulting density is smoothed with a 2-D moving average filter to remove any artifacts from

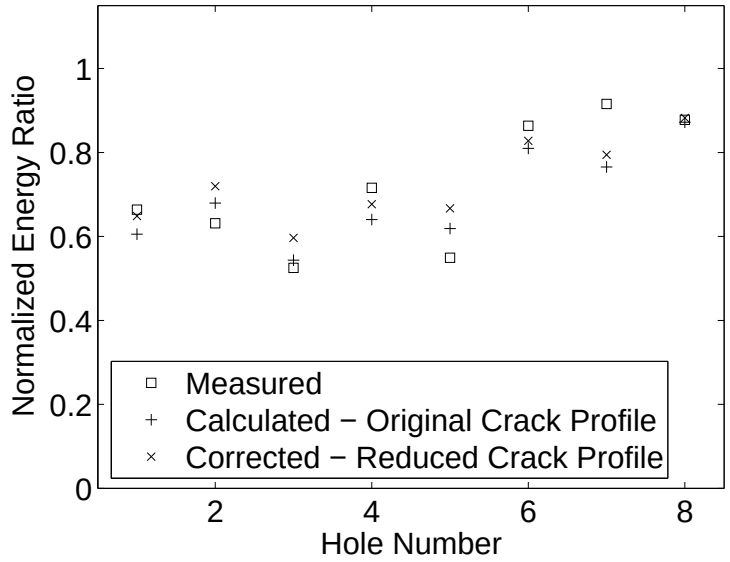

Figure 36: Comparison between measured, calculated, and corrected energy ratios. The correction is to consider crack closure effects.

the Monte Carlo process. The processing time is approximately 3.5 minutes on a standard PC in a MATLAB development environment. The energy density at 10,000 lbs loading is plotted in Figure 37(a). More insight, however, can be gained by plotting the contours that define the regions of 50%, 90%, and 99.9% energy, shown in Figure 37(b). As can be seen from the 99.9% contour line, the bulk of the energy is concentrated to within approximately 500 μm of the hole surface, whereas there is significant energy along the entirety of the hole surface. This result confirms the expectation that the ultrasonic method is sensitive to cracks along the entire length of the hole surface, but somewhat less so towards the top and bottom surfaces. It also confirms that depth sensitivity past 500 μm is limited, meaning that equal length cracks with depths greater than 500 μm will result in essentially the same ultrasonic response.

6.4 Results and Discussion

6.4.1 Crack Sizing Results

The primary result of this work is the capability of the ultrasonic method for sizing fastener hole fatigue cracks. A total of 200,000 crack profiles were randomly generated and processed with the energy density expression of Section 6.3.2. Results were generated for relating the calculated energy ratios to the following three crack dimensions:

1. Total surface crack length from both sides of the hole.

2. Average of the maximum crack depth on both sides of the hole.

3. Total crack surface area on both sides of the hole.

Also, the $\pm 2\sigma$ bounds are computed for each case. Figure 38 shows the mean and $\pm 2\sigma$ bounds for each crack dimension along with the measured data points.

The estimates of the crack dimensions for the eight experiments are generated from the measured energy ratios using the curves of Figure 38, and the actual and estimated values are shown in Table 9. As can be seen, there is reasonable agreement between the measured

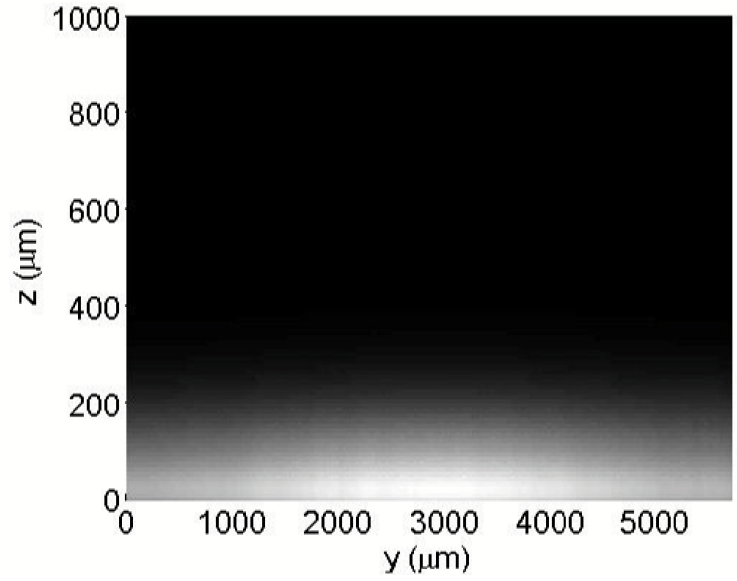

(a)

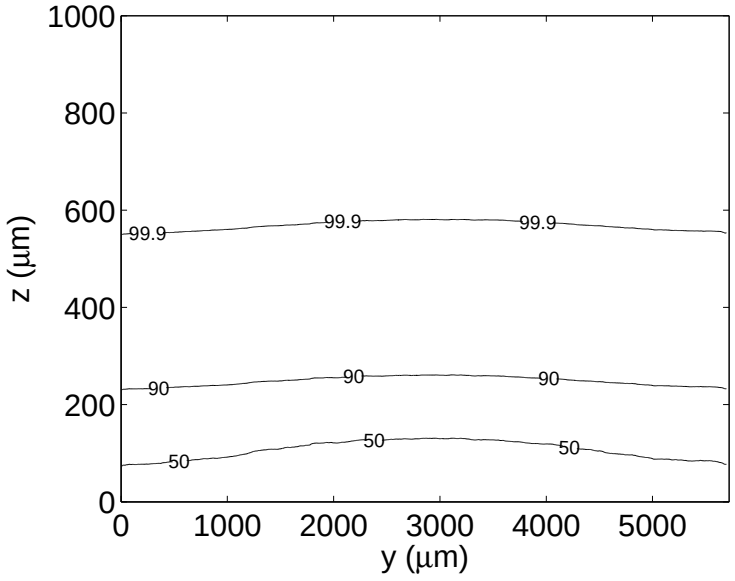

(b)

Figure 37: Ultrasonic energy density in the plane of expected crack growth. (a) Intensity map, and (b) lines of constant energy density.

and predicted crack dimensions, with an average measured error of 1.56 mm, 0.228 mm, and 0.729 mm^2 for total crack length, average depth and total area, respectively. For the depth and area measurements, the measured values generally fall within two standard deviations of the estimated values, indicating that the statistics have been realistically captured by the Monte Carlo process. For the length estimates, most of the data points fall outside of the $\pm 2\sigma$ bounds, indicating that there are additional sources of variation that have not been modeled. The depth and area estimates, including the standard deviations, are thus sufficiently accurate for the SHM state estimation framework.

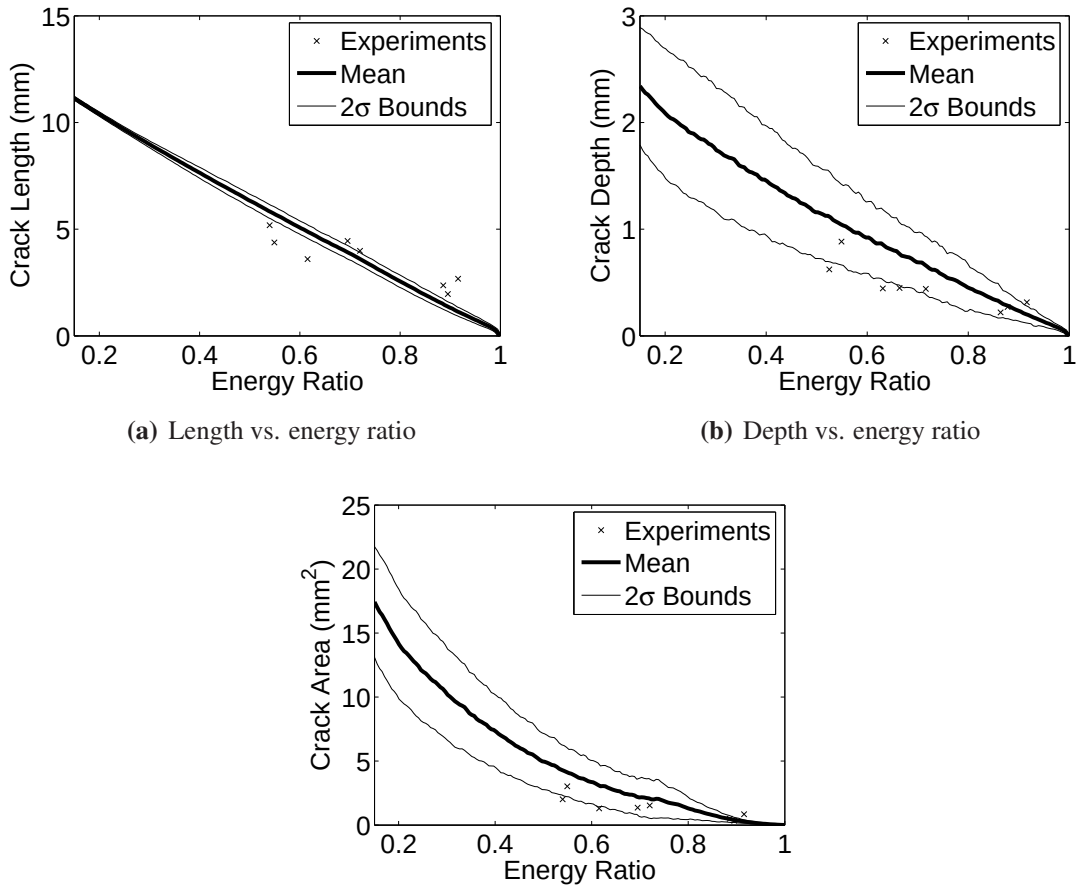

(a) Length vs. energy ratio

(b) Depth vs. energy ratio

(c) Area vs. energy ratio

Figure 38: Crack dimension versus energy ratio with $\pm 2\sigma$ bounds.

Two probable causes for differences between the modeled and measured crack sizes are transducer positioning errors and overly simplified wave propagation assumptions. Specifically, it is assumed that the transducers are mounted such that the energy is equally divided between the two sides of the hole. In practice, this perfect balance is never achieved, and one side of the hole will always have a higher relative energy compared to the other. In terms of the wave propagation physics, the energy-based approach is obviously an approximation; the next step would be to consider phase information when summing the rays. Also, a more complicated derivation for a Rayleigh-like wave on a cylindrical surface is presented by Viktorov [68], where only the change in c_R is included here. The full derivation would result shift the energy deeper into the material.

6.4.2 Probability of Detection

The other key result of this work is probability of detection (POD) curves, which are shown in Figure 39 for average depth and total area. These POD curves ignore the variations during the measurement process related to the material microstructure and transducer coupling changes. Energy ratio thresholds of 0.98, 0.95 and 0.90 are plotted, where the actual detection threshold is influenced by the noise of the energy ratio curve. The two extremes, 0.98

Table 9:

Comparison of actual and estimated crack dimensions.

	Length (mm)		Depth (mm)		Area (mm^2)	
Hole #	Measured	Estimated	Measured	Estimated	Measured	Estimated
1	6.55	4.29	0.449	0.768	2.091	2.506
2	6.37	4.70	0.445	0.855	2.450	2.964
3	5.64	6.02	0.624	1.118	2.396	4.603
4	6.68	3.66	0.440	0.660	2.838	2.097
5	7.03	5.72	0.884	1.042	5.528	4.118
6	4.53	1.76	0.220	0.315	0.966	0.649
7	0.76	1.13	0.315	0.201	0.078	0.271
8	2.28	1.59	0.271	0.283	0.571	0.532

and 0.9, are best and worst case values, respectively, as observed during numerous fatigue tests, and the 0.95 energy ratio value corresponds to a typical detection threshold. Assuming a threshold of 0.95, there is an 80% probability of detecting a crack with a depth of 0.13 mm, or an area of 0.15 mm^2; length results are not presented because of the obviously erroneous standard deviations.

6.5 Summary of State Estimation Models

There are three models related to the ultrasonic measurements required for the state estimation framework: (1) energy ratio versus crack depth, (2) energy ratio variance versus crack depth, and (3) crack depth versus energy ratio. A crack growth equation is used for the system model development, which is function of crack depth. As such, the three models will all be generated using the crack depth simulation results alone. All three models are developed using the 200,000 iteration process described in Section 6.2.4, and the curve fitting is done with the Curve Fitting toolbox of MATLAB.

6.5.1 Energy Ratio Response versus Crack Depth

The first model presented, $C(x)$, is the energy ratio response as a function of crack depth. This model acts as the observation function for the state estimation framework. Using the

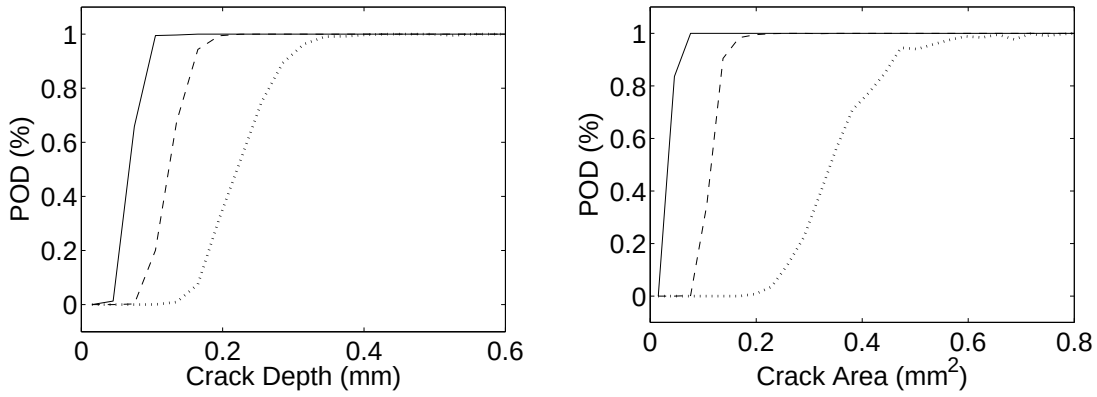

(a) Depth POD Curve **(b)** Area POD Curve

Figure 39: POD curves with energy ratio thresholds of 0.98 (solid line), 0.95 (dashed line) and 0.90 (dotted line).

statistics from the 200,000 iterations, the mean energy ratio response versus crack depth is fitted using a first-order Gaussian. The reason for using a Gaussian for the curve fit is to ensure that the derivative exists for the entire domain of interest. The equation for the Gaussian is given as,

$$C(x) = 1.276 \cdot \exp[-((x + 1.211)/2.455)^2], \tag{86}$$

where x is the crack depth in millimeters. Figure 40(a) illustrates each iteration of the Monte Carlo process and the associated mean energy ratio response versus crack depth. Figure 40(b) compares the mean value curve with the response given by Eq. (86).

6.5.2 Energy Ratio Response Variance versus Crack Depth

The next model, $Q_v(x)$, is the expected energy ratio variance for a given crack size measurement, which is utilized during the Kalman gain calculation. The measurement model variance is calculated in two parts. First, the Monte Carlo results from before provide an initial estimate of the variance, defined by the variable, $\widetilde{Q}_v$. The variance as function of crack depth is calculated from the Monte Carlo statistics and the resulting curve is shown

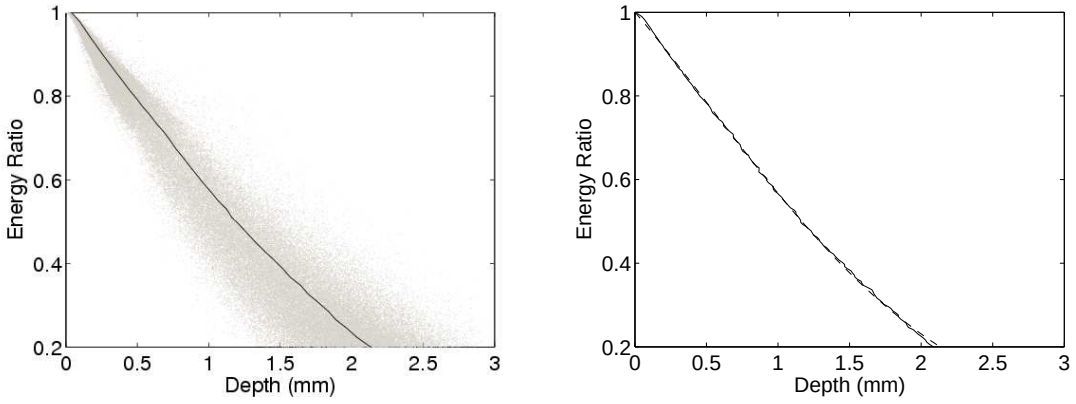

(a) Monte Carlo simulation **(b)** Comparison between mean and curve fit

Figure 40: Results from the Monte Carlo simulation for estimating the measurement model, $C(x)$, where (a) illustrates the mean value curve and (b) compares the mean value curve (solid line) and the curve fit given by Eq. (86) (dashed line).

in Figure 41, presented as a standard deviation for ease of interpretation. Unlike the measurement model, $C(x)$, it is not important that the expression for $\widetilde{Q}_v$ be differentiable. As such, the curve fit is a piecewise spline interpolation.

There is the requirement, however, that this crack shape noise obeys a Normal distribution. Figure 42 shows the histogram of energy ratio results for the Monte Carlo process for a crack depth of approximately 1 mm. Further, a Gaussian with mean and standard deviation defined for a 1 mm deep crack from Figures 40(a) and 41 is shown for comparison. As can be seen, the distribution of energy ratio response is close to a Gaussian.

This initial estimate of the variance, $\widetilde{Q}_v$, does not take into account any measurement noise during data acquisition. The second part of the measurement noise is approximated by defining Q_v as

$$Q_v = \widetilde{Q}_v + \sigma^2, \tag{87}$$

where $\widetilde{Q}_v$ is shown in Figure 41 and σ is the standard deviation of the undamaged energy ratio response, calculated during defect detection.

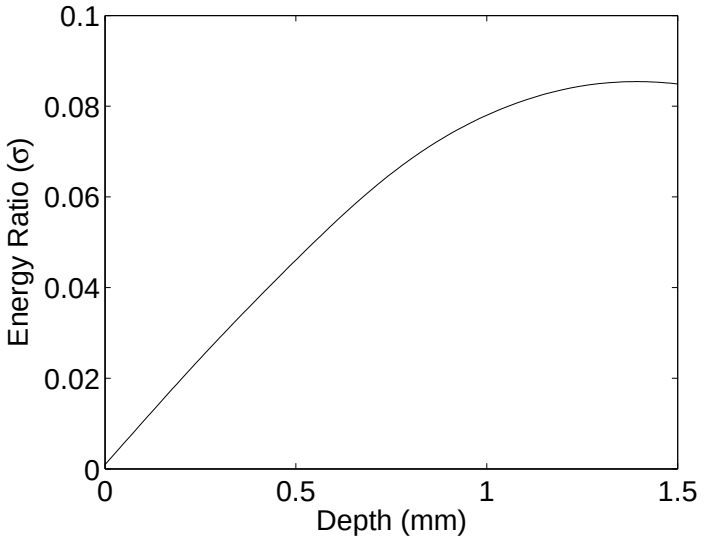

Figure 41: The standard deviation, $\sqrt{\widetilde{Q}_v}$, of the energy ratio response versus crack depth.

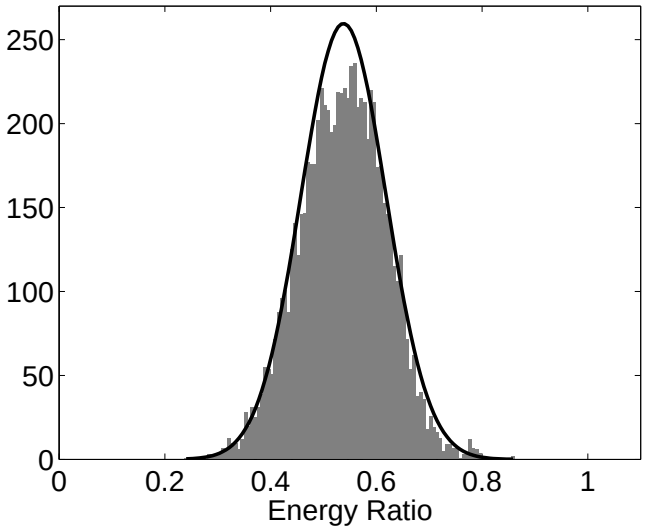

Figure 42: Histogram of energy ratio values at a depth of 1 mm from Monte Carlo results. Also shown is a Gaussian curve with mean and standard deviation defined from Figure 40(b) and Figure 41.

6.5.3 Crack Depth versus Energy Ratio Response

The final model, $\widetilde{C}(R)$, relates the crack depth to a given energy ratio measurement; it is the inverse model of $C(x)$. This last model is used to initialize the Kalman filter, and it also functions as the measurement-only approach for comparison. The mean crack depth as function of energy ratio response is calculated based on the Monte Carlo results. As with Q_v, $\widetilde{C}(R)$ does not need to be differentiable. Thus, linear interpolation of the data is used as the model. Figure 43 summarizes the $\widetilde{C}(R)$ model.

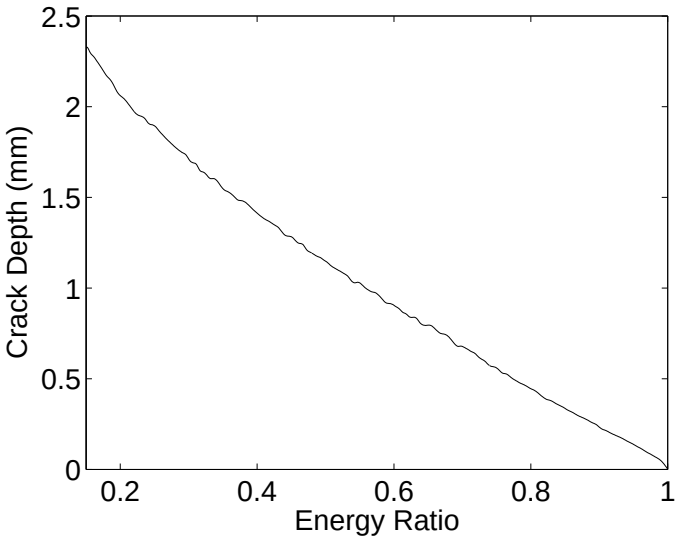

Figure 43: The mean crack depth versus energy ratio response, $\widetilde{C}(R)$, for EKF initialization and comparison purposes.

CHAPTER 7

SYSTEM MODEL

This chapter describes the details of the fatigue crack propagation model used with the state estimation approach. A brief overview of the history of fatigue crack growth models is provided in Section 7.1. Section 7.2 explains the approach for defining the system model, $A(x)$. The method for determining the statistics of the system model is discussed in Section 7.3. The approach for estimating the remaining structural life based on the crack propagation models is found in Section 7.4.

7.1 Crack Growth Equation Review

The development of the original crack growth equation originated in the 1960s and '70s with Paris's empirical derivation of the relationship between fatigue loading levels and crack growth rates [3]. Following Paris's study, this work is extended by several authors to more accurately account for differences in the fatigue process, such as variable amplitude loading and the effect of overloads. In recent years, more computationally-based approaches, such as the FASTRAN model [73], have been developed for dealing with complex geometries and fatigue spectrums. The importance of the crack growth model in an SHM framework is that any monitoring system can only provide information about the current state of a structure, making it necessary to combine damage growth models with anticipated usage to assess the remaining structural life [1].

7.1.1 Paris's Crack Growth Equation

In the early 1960s, P. C. Paris empirically derived a relationship between the cyclic crack growth rate, $\mathrm{d}a/\mathrm{d}N$, and the stress intensity ranges, ΔK, encountered during the fatigue process [3, 42]. This relationship serves as the foundation for almost all subsequent crack

growth models. Stress intensity, or K, quantifies the governing variable for crack growth, and is a combination of crack length, loading, and sample geometry, and is expressed as

$$K = FS\sqrt{\pi a}, \tag{88}$$

where a is crack length, S is the nominal stress assuming no cracking, and F is a dimensionless function of specimen and crack geometry. The stress intensity range for a fatigue cycle, ΔK, is the difference in stress intensity of the high nominal stress, S_{max}, and low nominal stress, S_{min}, for that cycle. For the derivation by Paris, a battery of fatigue tests were run at various ΔK values for a single geometry while monitoring the incremental crack sizes. The results of these tests allowed for a crack growth rate ($\mathrm{d}a/\mathrm{d}N$) versus ΔK curve to be produced; an example is shown in Figure 44.

At intermediate values of ΔK, shown as Region 2 of Figure 44, there is a straight line relationship on the log-log plot. This relationship can be written as

$$\frac{\mathrm{d}a}{\mathrm{d}N} = C(\Delta K)^m, \tag{89}$$

and is commonly known as "Paris's Law." This power law combines the stress intensity range with two material constants, C and m, to define the crack growth rate. The derivation

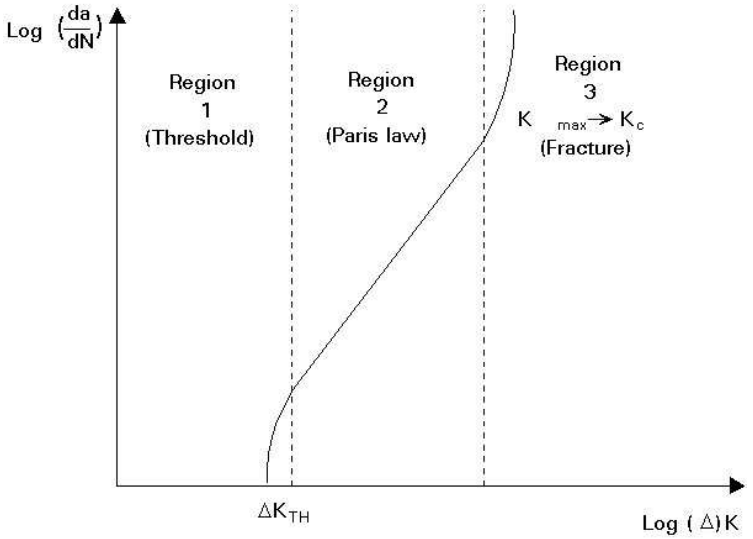

Figure 44: Paris's Law relationship [74].

of the material constants is done empirically for each type of material being fatigued, and the equation applies for the intermediate values of ΔK. For low values of ΔK, defined by a threshold ΔK_{th} for the material, crack growth typically does not occur because the loading is so small that the specimen is not actually being damaged. The upper extreme of the $\mathrm{d}a/\mathrm{d}N$ versus ΔK relationship is where the fatigue loading is near the fracture toughness of the specimen, K_c. In this regime, the sample is in a brittle failure mode, breaking almost immediately. While the fatigue process does not normally begin at this value, as the sample is fatigued it is likely that as the crack grows increasingly large, the ΔK values will approach K_c. Thus, the Paris's Law relationship does not effectively track the late crack growth just before failure.

Another important feature of Paris's equation is that it is geometry independent. The effect of geometry is captured in the ΔK parameter, specifically with the F correction factor. The purpose of the F value is to quantify the stress concentration because of the specimen geometry. There are several handbooks of geometry correction factors for modeling the effect of most practical engineering geometries [75]. This geometry independence is crucial for the applicability of Paris's Law to a wide variety of testing conditions and sample geometries. Without this geometry independence, the usefulness of the relationship would be severely limited, requiring each fatigue test proposed to develop individual $\mathrm{d}a/\mathrm{d}N$ versus ΔS derivations, an expensive and time consuming procedure.

7.1.2 Modifications of Paris's Equation

Continuing the original development of the crack growth equation by Paris et al. [3], later authors expanded Paris's work to account for several experimental factors. Specifically, the original crack growth equation is developed assuming constant amplitude fatigue and a simple sample geometry. A brief review of available crack growth equations is provided here, with the understanding that there are many more possible modifications.

One parameter that Paris's equation does not account for is R, the ratio of fatigue loads

for each cycle,

$$R = K_{min}/K_{max}. \tag{90}$$

Paris's equation assumes that R=0 (i.e., every cycle starts at zero applied stress). As shown in Figure 45, by changing the value of R, the da/dN versus ΔK curve is shifted. The effect of R varies based on the material being fatigued, where brittle, low-strength alloys exhibit a stronger dependence on R [74]. Also, for low-growth rate tests, where the ΔK parameter is near the ΔK_{th} threshold value, the value of R may have a strong effect. In an effort to account for the effect of R, several modifications of the Paris's Law relationship have been proposed.

The Walker equation is a widely used approximation that incorporates the R value [42]. E.K. Walker proposed that an effective stress intensity, $\overline{\Delta K}$, can be estimated by

$$\overline{\Delta K} = K_{max}(1 - R)^{\gamma}, \tag{91}$$

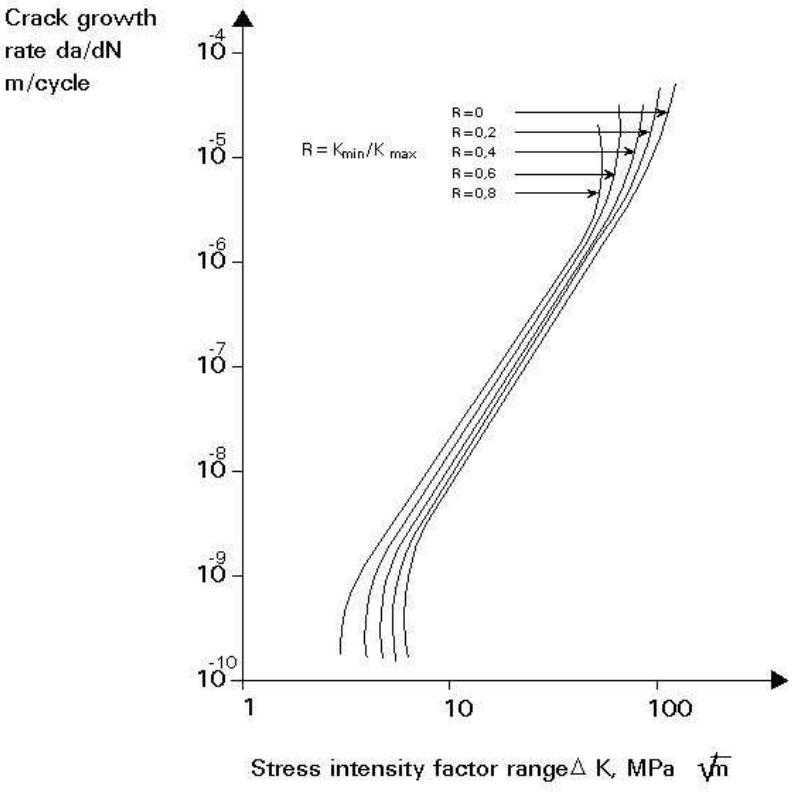

Figure 45: Effect of mean stress on crack growth rate [74].

where γ is a material constant. After substituting this expression into the original Paris relationship, the crack growth to stress intensity range relationship is reformulated as

$$\mathrm{d}a/\mathrm{d}N = C_1(\Delta K)^m, \tag{92}$$

where C_1 is a new material constant including R and γ, and m is unchanged from the original Paris's Law formation. The C_1 parameter is

$$C_1 = \frac{C}{(1-R)^{m(1-\gamma)}}, \tag{93}$$

where C and m are the Paris's Law parameters; it adjusts Paris's Law to incorporate the effect of R, thus improving the ability of the crack growth model to include the effects of high cycle fatigue and application to brittle alloys.

Additional modifications of Paris's Law attempt to account for crack growth as the value of ΔK approaches the upper extreme near the fracture toughness of the material [42]. One derivation, known as the Forman equation, includes the fracture toughness, K_c in its representation. The Forman equation is given by

$$\mathrm{d}a/\mathrm{d}N = \frac{C_2(\Delta K)^{m_2}}{(1-R)K_c - \Delta K}. \tag{94}$$

As K_{max}, the maximum stress intensity for a cycle, approaches the fracture toughness, K_c, the denominator approaches zero, resulting in the crack growth rate becoming large. This effect predicts the accelerated crack growth toward the end of the fatigue life.

Additional methods attempt to account for the effect of residual stress around crack surfaces [73, 76, 77]. The residual stresses around a crack surface press the crack surfaces together, which results in a retardation of the crack growth rates. Specifically, ΔK is redefined not as the difference between the maximum and minimum stresses, but as

$$\Delta K = K_{max} - K_{open}, \tag{95}$$

where K_{open} is the stress intensity necessary to separate the crack surface and it is assumed that $K_{min} > K_{open}$. If the maximum stress intensity for a cycle is below this opening stress intensity, no crack growth will occur.

Several authors have accounted for this effect in their crack growth equation. Patankar et al. [76] developed a state space realization of a fatigue crack growth model accounting for the crack opening stress. As with most fatigue crack growth models, their approach is based on the Paris relationship, described by Eq. (89). Their governing equation of crack growth is given as,

$$a_{k+1} - a_k = h(\Delta K_k^{eff}), \tag{96}$$

where a is the crack length and k is the time index. The effective stress range at time k, ΔK_k^{eff}, is defined to be related to the difference between the maximum applied remote stress, S_k^{max} and the crack opening stress, S_k^o. The difficulty for their approach is that the opening stress is dependent on stress history, and cannot be readily determined. For their formulation, the two state variables are crack depth and the crack opening stress. The crack length, a, is assumed to be measurable and the crack opening stress, S^o, though not necessarily measurable, can be determined from the finite stress history. An additional empirical relationship is developed for relating the stress history to the opening stress, S_k^o, where the details of their third order correction can be found in [76]. Also, their approach accounts for the effect of stress overloads. While the crack opening stress remains predictable for most situations, a stress overload causes the opening stress to increase temporarily. The opening stress will settle back to the original, pre-overload conditions after additional cycling. This effect results in a temporary retardation of the crack growth process.

Finally, crack growth equations have been developed that more realistically model the cracks themselves. Specifically, Paris's original equation and its early derivatives treat a crack as a void in the sample, effectively lowering the cross-sectional area of the specimen. The advantage of this approach is that a closed form solution is able to be realized. In reality, however, there are additional effects, such plasticity near the crack tip and the 3-dimensionality of the crack shape. Computational models attempt to model these effects, where an example is the FASTRAN model (see Newman [73, 77] for a description), which is a plasticity-induced crack-closure model, to more accurately depict the crack growth.

The FASTRAN closure model employs a modified Dugdale strip-yield model that accounts for plasticity around the crack tip [78]. The cross-sectional area of the specimen is divided among several regions based on the conditions of the material, such as plasticity or crack opening. This computational model, while more accurate in its representation of the fatigue crack growth, requires more processing time and is unable to be expressed in closed form.

7.2 System Model for Crack Propagation

The next modeling aspect is determining an appropriate model for fatigue crack propagation for the SHM framework. It is desirable that this model be differentiable and based on established mechanics theories. Also, to make the model function in near real-time for state estimation, a simple model of fatigue crack growth is preferred. As such, the original Paris's power law is used as the system model. Paris's equation from before is restated as

$$\frac{dx}{dN} = C(\Delta K)^m, \tag{97}$$

where the increment crack length, x, is related to the material constants, C and m, and the stress intensity, ΔK. The material constants C and m for 7075-T6 Al are $2.71 \times 10^{-8} MPa\sqrt{mm}$ and 3.7, respectively, with the resulting incremental growth rates in units of mm/cycles [42]. The stress intensity range, ΔK, is given by

$$\Delta K = F\Delta S\sqrt{\pi x}, \tag{98}$$

where ΔS is the applied stress range for that cycle and F is a geometry correction factor related to the crack shape and specimen geometry. A variety of geometry correction factors exist in literature for cracks propagating from a notched specimen, such as through-thickness cracks [42], half circular crack [79], and elliptical cracks [75, 79]. For the system model, the F parameter is defined as [80]

$$F = F(x) = \frac{Q \cdot k_t}{\sqrt{1 + 4.5 \cdot x/r}}, \tag{99}$$

which assumes a circular notch of radius r with symmetric elliptical cracks and stress concentration factor, k_T. For the specimen described in Chapter 3, the stress concentration

factor is approximately 2.52 [42]. The reason for choosing this geometry correction factor is that it allows for the entire range of expected crack geometries by varying a shape variable, Q. The Q variable approximates the effect of different elliptical crack shapes [80], with $Q = 0.65$ corresponding to a half circular crack and $Q = 1.12$ corresponding to a through-thickness crack (elliptical crack with very large aspect ratio). Further, the geometry correction factor assumes cracks centered along the thickness direction, which is valid given the fatigue experience for this configuration. The system model, $A(x)$, and local linearization, A_{n-1}, for the EKF framework are then defined as

$$x_{n+1} = A(x_n) = x_n + \sum_{i=1}^{N} C(\Delta K_i)^m, \tag{100}$$

$$A_{n-1} = x_n - x_{n-1}, \tag{101}$$

where the summation is over the N fatigue cycle intervals between measurements. The same series of 8 experiments used for the development of the measurement models, summarized in Chapter 3, define the parameters of the system model. The value of Q used for the system model is 0.85 and was defined by minimizing the average absolute error between the final EKF response and measured crack depth for the eight experiments used in the system model development, discussed in Chapter 8.

7.3 System Model Statistics

The remaining aspect to quantify is the statistical variance of the system model. The original Paris's equation described in Section 7.1.1 is a deterministic equation. Practical experience, however, is that variations exist between experiments. For the purpose of approximating this variance, the two most likely causes of experimental differences in Paris's equation are randomized, specifically the material constants and geometry correction factor. A Monte Carlo simulation is employed to estimate the crack depth variance for each timestep of the EKF framework. For a given crack depth and fatigue spectrum, several iterations of the crack growth curves with unique parameters are computed, where the variance, Q_w, is calculated based on the final crack depths.

Randomizing the material constants of Paris's equation is proposed by Ray and Patankar [81], where they generated the multiplicative material constant, C, from a log-normal random distribution, Ω. Based on their results, the expected value and variance of the Ω distribution are given by

$$E[\Omega] = C, \tag{102}$$

$$VAR[\Omega] = 7.91X10^{8}C^{2}/\Delta S^{2m}, \tag{103}$$

with ΔS the stress intensity range, and C and m the material constants from before. Since the experiments for this study utilize spectrum loading, the ΔS for computing the variance is taken to be the average ΔS during the entire 2640 cycle spectrum. For each iteration of the Monte Carlo simulation, the multiplicative constant is generated from this distribution.

The second variability between experiments is related to the crack shapes. Based on experience from many fatigue tests, the likely crack shapes are somewhere between half circular and through-thickness cracks. Referring back to Eq. (99), the shape variable, Q, is generated from a Normal distribution with mean and variance such that it falls almost entirely within 0.65 and 1.12 [80], spaning the entire range of crack shapes. For each iteration, Q is randomly generated from the Normal distribution with mean and standard deviation set to 0.885 and 0.0783, respectively.

Using the above methodology for computing the crack growth parameters, a total of 500 iterations are used to compute Q_w at each timestep of the EKF framework. As an example, consider a crack depth of approximately 0.2 mm fatigued by 1320 cycles of the provided spectrum. Figure 46(a) illustrates the range of expected crack growth curves, where Q_w is the variance of the final crack depth for each curve. Also, Figure 46(b) shows the histogram of the final crack depths compared with a Gaussian curve with mean and variance defined from the final crack depths of Figure 46(a). While not exactly Gaussian, it is assumed to be close enough for the EKF framework.

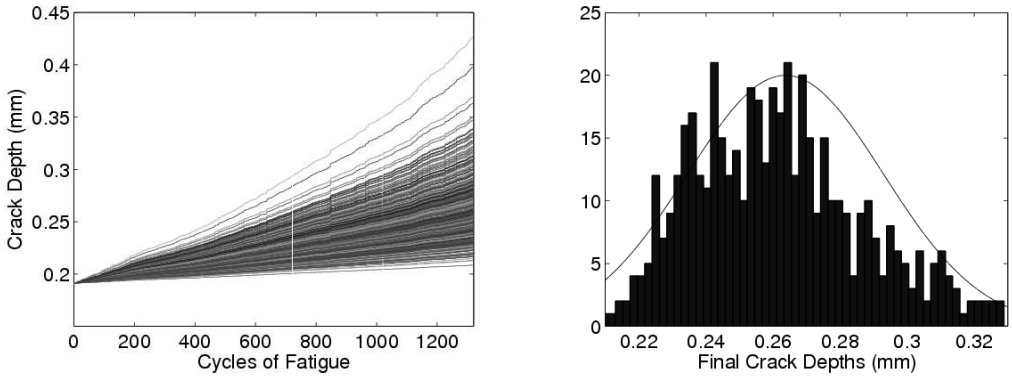

Figure 46: For an initial crack size of 0.2 mm and 1320 cycle spectrum, a) an example crack growth curves for computing the final crack depth variance, Q_w and b) the histogram of the final crack depths with a Gaussian curve for comparison.

7.4 Prognosis of Remaining Life

In parallel to the state estimation framework for tracking the fatigue damage in the specimen, an estimate of the remaining fatigue life is generated using the crack growth model. This approach is an illustration of an established methodology for like prediction. A Monte Carlo simulation of expected crack growth curves is performed to estimate the distribution of fatigue time to reach a critical crack size, similar to the approach described by Hoffman and Hurtado [39]. Based on fatigue experience for the straight through-hole with no fastener, once the crack is at the surface of the specimen and approximately 2 mm deep from the edge of the hole, failure is eminent. Assuming a semi-circular crack front, this corresponds to a maximum crack depth of approximately 4.86 mm (h/2 + 2 mm). The number of cycles it would take for the crack to reach this depth is the prediction of the remaining fatigue life.

The process for computing the life prognosis is based on the system model variance described in Section 7.3. For each prognosis estimate, the Kalman filter output is assumed to be the exact crack depth at that time. A Monte Carlo simulation is produced by statistically varying the material constant C and shape parameter Q to produce a series of crack growth curves from the start point defined from the Kalman filter. Example crack growth curves

are shown in Figure 47, showing 100 iterations of the Monte Carlo simulation starting at 0.1 mm, where each curve stops after reaching 4.86 mm. A total of 2500 iterations of this process are performed and a distribution of the cycles to reach the critical crack depth is computed, shown in Figure 48. Finally, the mean and standard deviation of the cycle count at the critical crack size are given as the life prediction estimate, where the mean is 22443 cycles and standard deviation is 8102 cycles for this derivation. Typically, instead of mean and standard deviation, the prognosis estimate is given by defining a confidence threshold, C, of the density curve shown in Figure 48. The prognosis estimate is given as the number of remaining fatigue cycles where $C\%$ of the density curve is to the right of the prognosis estimate.

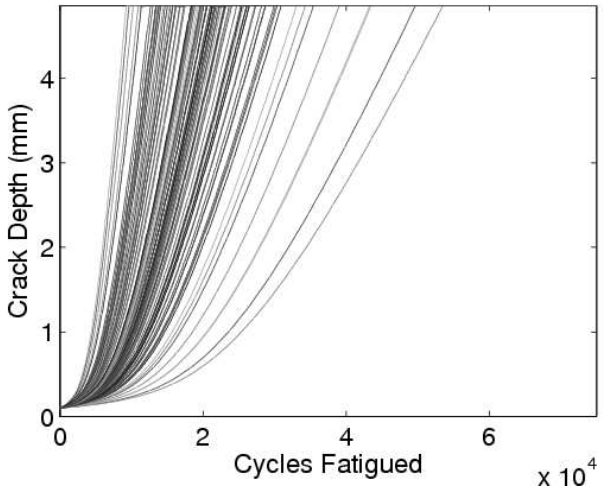

Figure 47: Example crack growth curves from the Monte Carlo simulation for an initial crack depth of 0.1 mm.

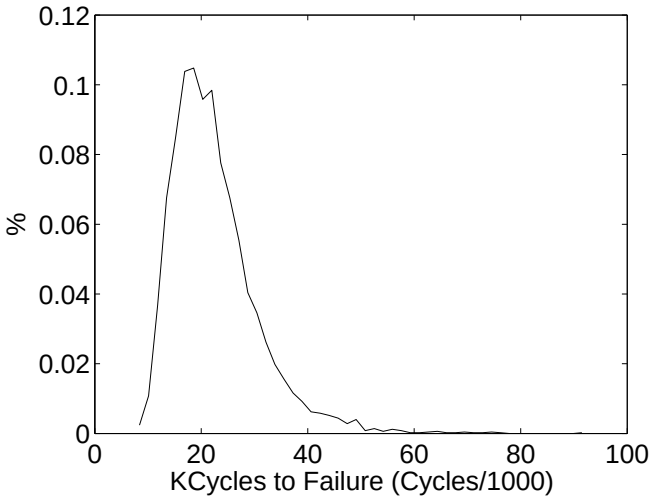

Figure 48: Example distribution of remaining cycles till failure for an initial crack depth of 0.1 mm.

CHAPTER 8

RESULTS

The purpose of this chapter is to present the experimental results of integrated damage detection, tracking, and prognosis resulting from the SHM framework. A series of eight fatigue experiments are used to test the framework, the same experiments used in the development of the measurement model and summarized in Table 3. The organization of this chapter is to first summarize the SHM framework modules in Section 8.1, restating the final results from the preceding chapters. Section 8.2 presents the experimental energy ratio curves and illustrates the results from the detection strategy. Section 8.3 presents the crack sizing results using only the measurement model from Chapter 6. Section 8.4 outlines an example of state estimation tracking of the crack size for one fatigue experiment. State estimation tracking for all experiments are found in Section 8.5. Finally, the final prognosis of the remaining structural life is summarized in Section 8.6.

8.1 SHM Framework Modules

During the development of the thesis in the preceding chapters, several models and algorithms are created for integration into the full SHM framework. This section outlines their final form. Also, any specific parameters left undefined are addressed.

8.1.1 Crack Detection

As described in Chapter 4, a detection strategy is developed to automatically process the energy ratio curves using a crack detection algorithm combined with windowing of the ultrasonic waveforms. However, the experiments used in the development of the strategy utilized a “Balanced Arrival” transducer configuration. The SHM framework experiments used in this section employed a “Center Peaked” configuration. The importance of this

difference in configuration is that there is only one arrival for consideration for the SHM framework experiments instead of two, reducing the effectiveness of the time-frequency windowing described in Chapter 4. As such, only the crack detection algorithm, found in Section 4.2, is employed to determine the first indication of damage from the energy ratio curves, and multiple time-frequency windows are not used.

Further, for experiments used in the development of the crack detection algorithm of Section 4.2, a measurement interval of 2640 cycles is employed. The data in this Chapter, however, has a measurement interval of 1320 cycles, or twice as often. The reason for this change is simply to provide more data points for the state estimation tracking. The original parameter values for the crack detection algorithm of $N = 6$ and $S = 2$ measurement sets are thus not applicable. It was found that values of $N = 16$ and $S = 2$ give reasonable results compared to visual examination of the energy ratio curves. The difference in the N parameters is because of the change in measurement interval. Also, the original value for N was constrained by very early detection of cracking; for some experiments, N could not be larger than 6 for the data in Chapter 4 as the defects are detectible after the 7^{th} data set.

8.1.2 Crack Size Tracking

Chapters 5 - 7 describe the state estimation approach for real-time crack sizing during the fatigue process. A standard EKF is employed as the statistical approach for combining the ultrasonic measurements and the crack growth laws. The models associated with the EKF are provided below, along with an additional model relating energy ratio measurements to crack depths directly.

8.1.2.1 Measurement Models

Chapter 6 describes three models for relating the ultrasonic measurements to crack dimensions. Specifically, the model of the energy ratio response versus crack depth, $C(x)$, required for the EKF implementation, is shown in Figure 49(a). Also, the variance of the measurement model ignoring microstructural noise during experimentation, $\widetilde{Q}_v$, is shown

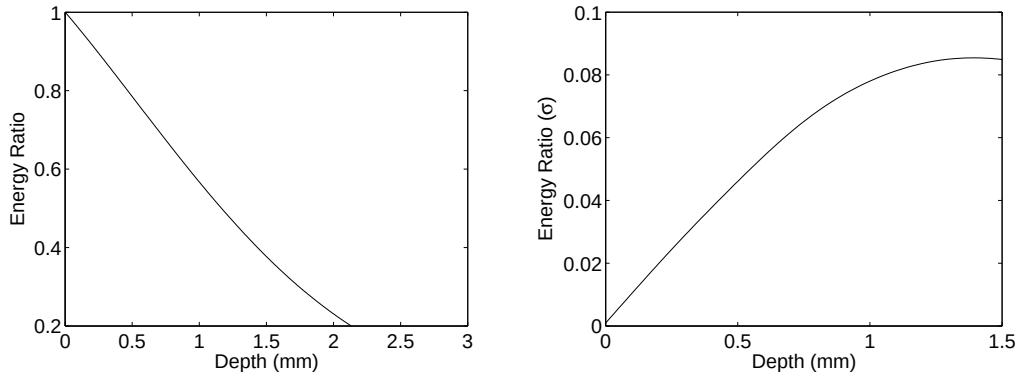

Figure 49: Measurement models necessary for the state estimation framework: (a) crack depth versus energy ratio response, $C(x)$, and (b) measurement model standard deviation versus energy ratio response, $\sqrt{\widetilde{Q}_v}$

in Figure 49(b). These two models are combined with the ultrasonic measurements for integration with the EKF framework.

In addition to the measurement model, $R = C(x)$, an inverse model is provided to relate the energy ratio response to crack depths directly, $x = \widetilde{C}(R)$. The importance of this model is twofold. First, a measurement-only estimate of the crack depth is given via this additional model to compare with the output from the state estimation. Also, the additional model is used to initialize the EKF framework prior to tracking. This model is shown in Figure 50.

8.1.2.2 Crack Propagation Models

Chapter 7 describes the necessary system models related to the crack growth equations. Specifically, a simple Paris's equation formulation provides the estimate of crack growth given an assumed fatigue spectrum. Since the measurement interval is 1320 cycles, the system model, $A(x)$, and its derivative are given by

$$x_{n+1} = A(x_n) = x_n + \sum_{i=1}^{1320} C(\Delta K_i)^m, \tag{104}$$

$$A_{n-1} = x_n - x_{n-1}, \tag{105}$$

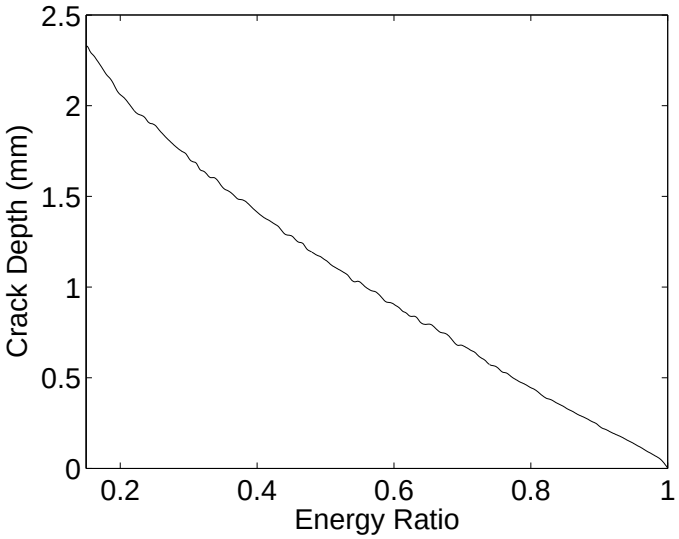

Figure 50: The mean crack depth versus energy ratio response, for Kalman filter initialization and comparison purposes.

where C and m are the material fatigue constants and ΔK is the stress intensity, given by

$$\Delta K = F\Delta S\ \sqrt{\pi x}, \tag{106}$$

$$F = F(x) = \frac{Q \cdot k_T,}{\sqrt{1 + 4.5 \cdot x/r}}. \tag{107}$$

The value of Q for the experiments is determined based on the EKF responses. For $Q = 0.85$, the best results are achieved for the SHM framework.

The statistical variation associated with the system model, $A(x)$, is produced by randomizing the crack shape parameter, Q, and the material constant, C. After each timestep of the EKF framework, the variation associated with each system model output, $\hat{x}(n|n)$ is computed with 500 iterations of the randomized system model.

8.1.3 Fatigue Life Prognosis

The approach for determining the fatigue life prognosis is described in Chapter 7, where the methodology is to create a Monte Carlo simulation of possible crack growth curves until they reach a critical crack depth of 4.86 mm. Based on these curves, a distribution of the expected cycles till failure can be produced assuming repetitions of the fatigue spectrum.

The provided prognosis estimate is the mean value and standard deviation of the fatigue cycles remaining.

8.2 Detection Results

Summarized in Table 3 in Chapter 3, a total of eight experiments are available for characterizing the performance of the final SHM framework. The energy ratio curves from each of the eight experiments are shown in Figure 51. As can be seen in the figure, the experiments are stopped at a variety of final crack sizes based on the last energy ratio response. Additionally, it should be noted that the energy ratio curves before detection typically exhibit small upward or downward slopes in response. This slope is related to the changes in the coupling between the transducer and sample surface during the fatigue process. This trend is corrected by renormalizing the energy ratio curve by the average energy ratio response pre-crack detection; the renormalized curves are shown in Figure 51. Finally, the results of the crack detection algorithm are highlighted, where the first indications of cracking are within one measurement set of visually estimated detection points.

8.3 Measurement Model Results

For comparison purposes, each energy ratio curve is first processed using only the measurement model, $\widetilde{C}(R)$. For each ultrasonic measurement, an estimate of the crack depth is computed. The resulting measurement model response is shown in Figure 52. Also, the measured crack depth is provided for each experiment, where this depth is the average maximum depth from both sides of the hole. As observed, the crack size results do track the growth of the crack, but the final crack estimates are not always accurate. Also, the noise of the measurement process carries over into the measurement model response, where there is an observable amount of variance in the crack depth estimates.

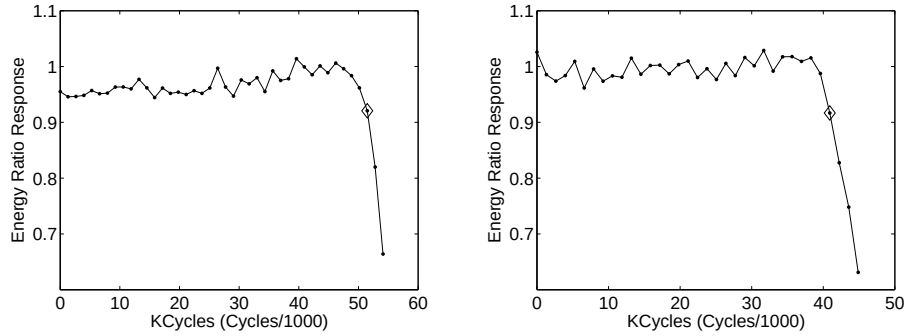

(a) Experiment 1

(b) Experiment 2

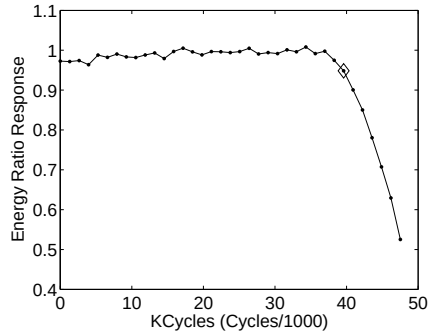

(c) Experiment 3

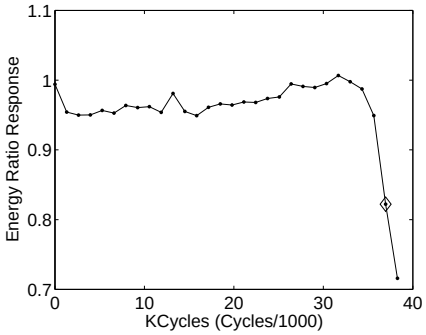

(d) Experiment 4

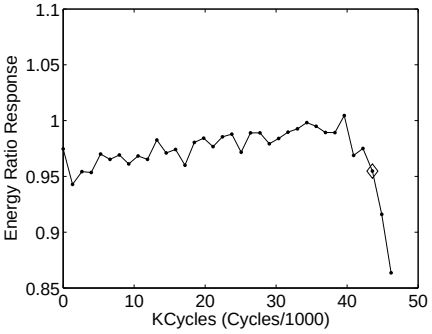

(e) Experiment 5

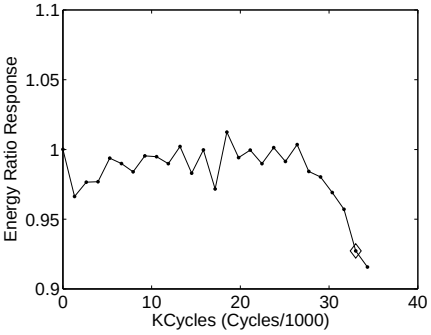

(f) Experiment 6

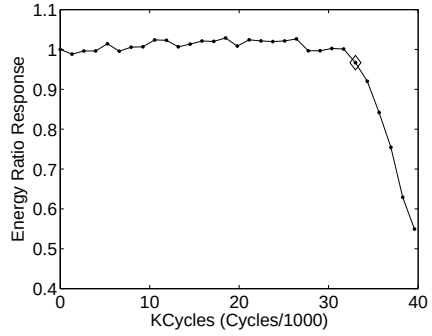

(g) Experiment 7

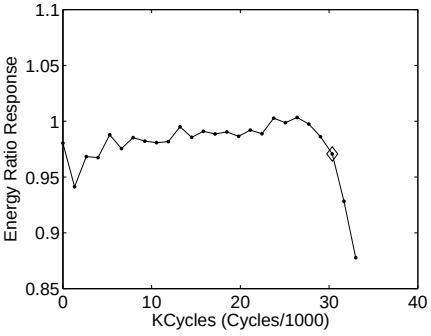

(h) Experiment 8

Figure 51: Energy ratio curves from the eight experiments. Also, the measurement set corresponding to defect detection is highlighted with the ◊ marker.

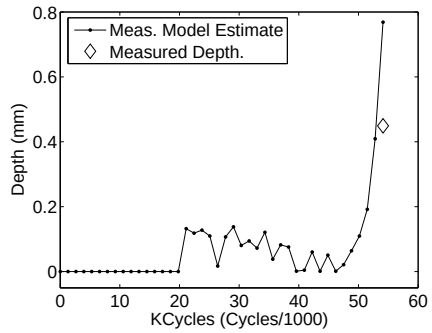

(a) Experiment 1

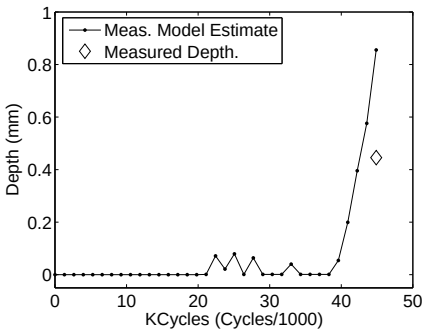

(b) Experiment 2

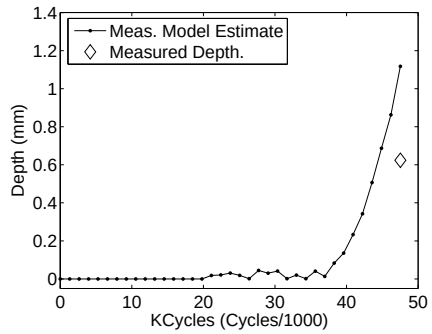

(c) Experiment 3

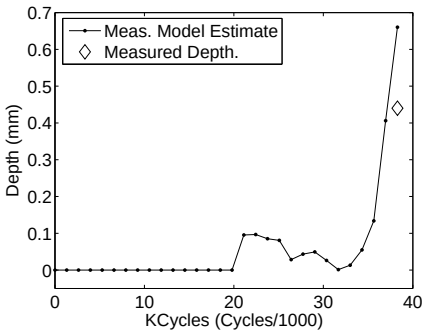

(d) Experiment 4

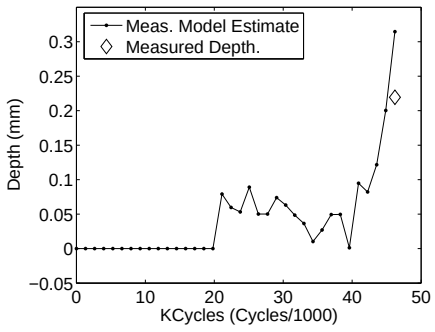

(e) Experiment 5

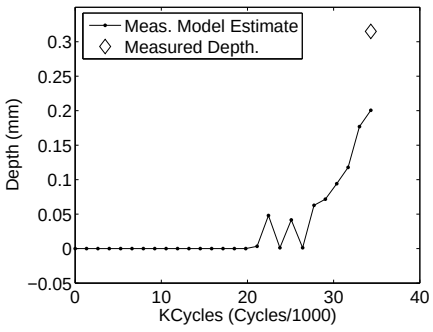

(f) Experiment 6

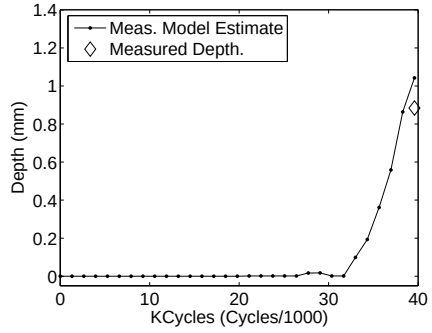

(g) Experiment 7

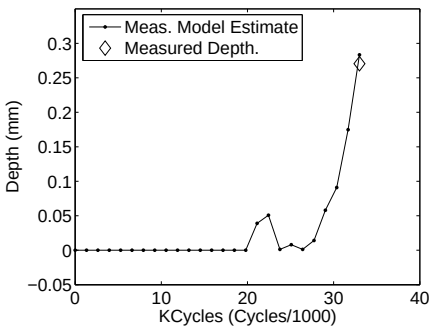

(h) Experiment 8

Figure 52: Crack depth estimates using only the measurement model $\widetilde{C}(R)$. Measured final crack depth is shown with the $\diamond$ marker.

8.4 Crack Depth Tracking Example

The focus of this section is to present a detailed example of the EKF framework. Specifically, the interaction between the ultrasonic measurements and the crack growth equation approximations is examined for a single experiment. Referring back to the energy ratio curve from experiment 1 shown in Figure 51(a), the detection strategy yields $n_{detect} = 39$ (i.e., cracking is detectible during the 39^{th} measurement set (51480 Cycles)). The initialization of the Kalman filter is given by

$$\hat{x}(n_{detect} - 1|n_{detect} - 1) = \widetilde{C}(R(n_{detect} - 1)), \tag{108}$$

$$P(n_{detect} - 1|n_{detect} - 1) = \widetilde{C}(R(n_{detect} - 1))^2, \tag{109}$$

which uses the previous measurement set, $n_{detect} - 1$, to estimate the initial crack depth and statistics.

Following the initialization, there are three remaining data points to estimate crack dimensions using the EKF framework (n_{detect}, n_{detect} + 1, and n_{detect}+2). Figure 53(a) illustrates the first timestep of the EKF. As can be seen, there is an observed difference between the measurement and system model responses. However, since the crack size is relatively small and has an associated small measurement model variance (Figure 49(b)), the EKF framework weights the measurement model response much higher than the system model response. The net result is that the EKF response is within 1 μm of the measurement model response for this first step of the EKF.

For the next timestep, shown in Figure 53(b), the crack size estimates are larger. The measurement model variance associated with this larger crack size is also larger, which produces an EKF estimate closer to the system model response than the measurement model response. The trend continues for the third and final ultrasonic measurement, shown in Figure 53(c), where the EKF response is even closer to the system model response compared to the previous timestep. If more ultrasonic measurements had been available, the trend would continue as the measurement model variance increases.

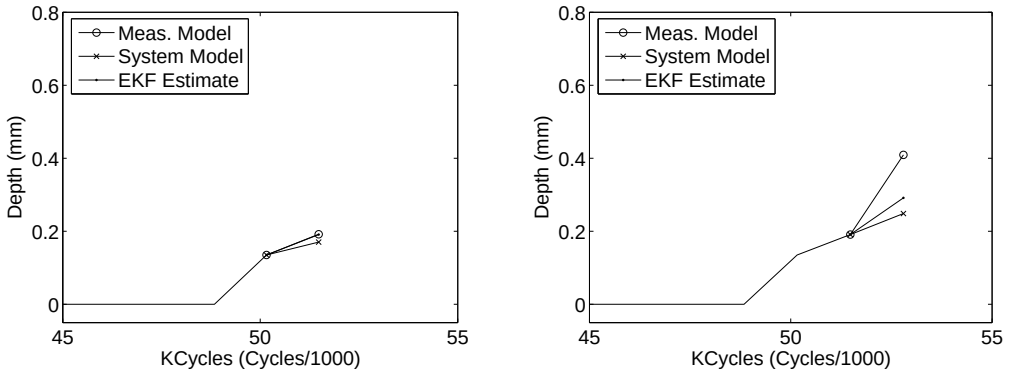

(a) n_{detect} **(b)** $n_{detect} + 1$

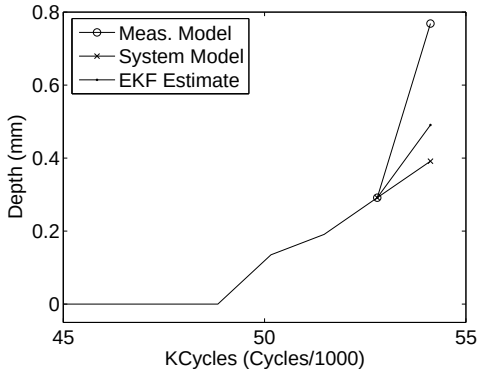

(c) $n_{detect} + 2$

Figure 53: Crack estimation evolution combining the measurement model estimate and system model estimate to produce the final EKF response.

In parallel with the crack size estimation after each timestep, the prognosis strategy is used to generate estimates of the remaining fatigue life. The remaining life estimates after each of the three timesteps are summarized in Table 10. As expected, the remaining cycles of fatigue for each estimate are reduced after each timestep. Further, the standard deviation of each estimate is reduced after each step, indicating an improved confidence in the remaining structural life. It should be noted that while the estimate of the remaining life is decreasing, the differences between each successive prognosis estimate are larger than the 1320 measurement interval. Also, these values are unverified as the experiment is not taken to complete failure, but interrupted to ensure a small crack depth. The prognosis estimates are presented to show capability rather than to verify life prediction.

Table 10:

Prognosis estimates of remaining fatigue life after each EKF estimate for experiment 1

timestep	Remaining Life (Mean)	Remaining Life (σ)
n_{detect}	19032	6987
$n_{detect} + 1$	17129	6237
$n_{detect} + 2$	15036	5531

8.5 Tracking Results

This section summarizes the performance of the state estimation methodology from estimating crack sizes for each of the experiments. For each experiment, the EKF framework response is compared to the results using the inverse measurement model, $\widetilde{C}(R)$. Estimates using only crack growth laws are not provided because small differences in the initial crack depth assumption produce large differences in the total fatigue life.

Of the eight experiments, six showed improved tracking performance using the EKF framework, where the measured crack depth is the average maximum depth from both sides of the hole. These experiments, shown in Figure 54, demonstrated an average absolute error in estimating the actual crack depth of approximately 0.13 mm, while the purely measurement approach had an mean absolute error of 0.28 mm. Also, because of measurement noise during the fatigue process, there are an appreciable number of false positives prior to detection by the crack detection algorithm. Further, only the final crack dimension is known, so it is not possible to quantitatively assess the EKF performance prior to the final measurement. For the remaining two experiments, shown in Figure 55, the inverse measurement model approach provided equal or better results compared to the EKF method, where experiment 7 shows almost no difference between the two methodologies and the inverse measurement model approach is clearly superior for experiment 8.

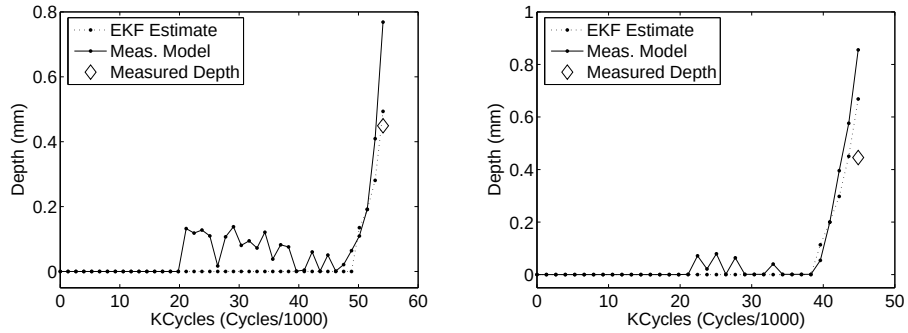

(a) Experiment 1 **(b)** Experiment 2

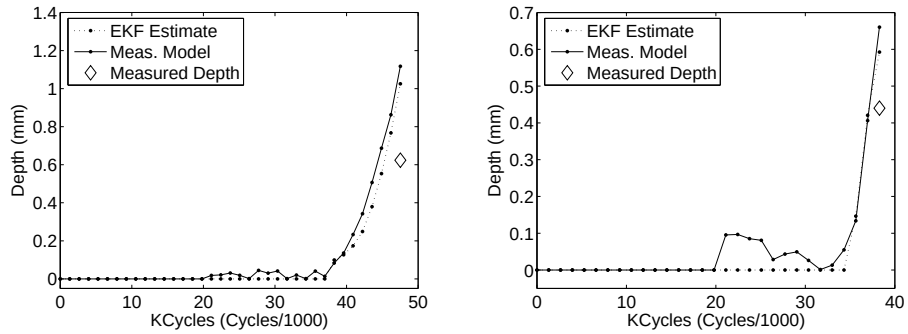

(c) Experiment 3 **(d)** Experiment 4

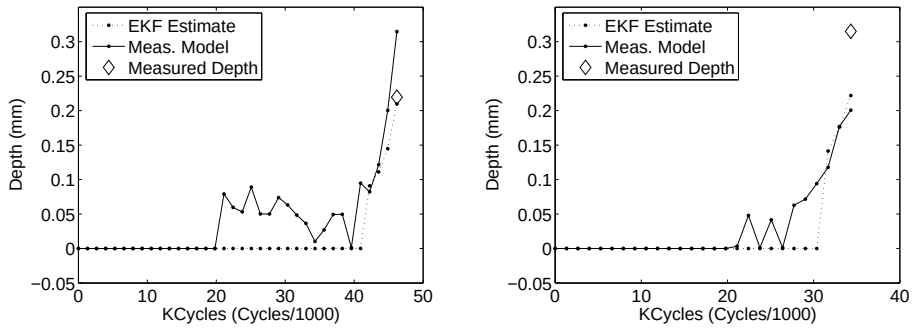

(e) Experiment 5 **(f)** Experiment 6

Figure 54: The experimental results showing improved crack sizing with the EKF framework (dotted) compared to the measurement model (solid). The measured maximum crack depth for each experiment is also shown (◊)

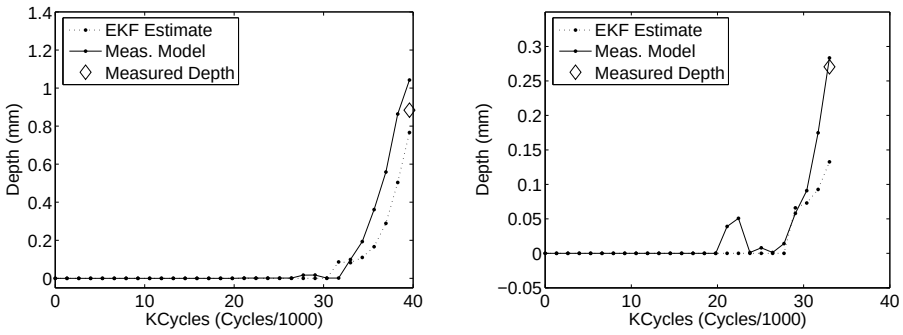

(a) Experiment 7 **(b)** Experiment 8

Figure 55: The experimental results showing inferior crack sizing with the EKF framework (dotted) compared to the measurement model (solid). The measured maximum crack depth for each experiment is also shown (◊)

8.6 Prognosis of Remaining Life

The final aspect of the SHM framework is the prognosis of remaining life. Table 11 details the final remaining life estimates assuming no additional ultrasonic measurements for each of the experiments. It is desirable during the experiments to capture the small crack performance, which produces large remaining life estimates (>10,000 cycles). It would have been possible to continue the fatigue process and record ultrasonic waveforms for each of these specimens, but the experiments were fractured to digitize crack surfaces. The remaining life estimates, however, are unverified as none of the experiments were taken to failure. Further estimation and validation of remaining life is beyond the scope of this thesis.

Table 11:

Prognosis estimates of remaining fatigue life in cycles

Experiment #	Remaining Life (Mean)	Remaining Life (σ)
1	14962	5315
2	13756	5093
3	11650	4101
4	14049	4993
5	18479	6726
6	18090	6264
7	13118	4878
8	20832	7477

CHAPTER 9

CONCLUSIONS AND FUTURE WORK

9.1 Conclusions

This thesis presents a framework for *in situ* ultrasonic monitoring using state estimation methodologies and tests it on the problem of estimating sizes of fastener hole fatigue cracks in metallic components. Unique in this work is the combining of time history data with damage propagation laws for both diagnosis and prognosis in the context of structural health monitoring (SHM). In contrast, a more conventional nondestructive inspection approach for detecting and sizing these fatigue cracks produces estimates of their sizes and locations, but these methods are unsuited for real-time monitoring applications. Sensor positions for nondestructive inspection techniques are variable, whereas for SHM, the sensors are permanently attached at fixed locations. Further, inspection techniques only provide an estimate of the crack size at the current time, and are not able to take advantage of either the time history of crack size estimates or models of damage progression. SHM is an emerging field that can provide this time history information by using permanently attached sensors, and this thesis shows how the time history data can be effectively used to improve both detection and sizing of fastener hole fatigue cracks. A natural extension of this methodology is estimation of remaining structural life, or prognosis, which is also shown here.

As a first demonstration of using the time history of the data, a detection framework was developed for automatically classifying the presence of fatigue damage using an empirical algorithm in conjunction with time and frequency information extracted from ultrasonic waveforms. A cost function was created for determining which time and frequency regions of the original ultrasonic waveforms contained relevant information regarding crack detection. It was found that because of the complex interaction between the crack surfaces and

the ultrasonic energy, there are multiple time and frequency regions that provide improvements over the full time and complete bandwidth ultrasonic waveforms. Applying a data fusion strategy to results from the best time and frequency windows led to substantially earlier detection of fatigue damage in the life of the structure.

Further use of time history data requires a well-characterized measurement model. An ultrasonic measurement model was developed that relates the ultrasonic response to fatigue crack dimensions, and also characterizes the measurement uncertainty. This measurement models employs a ray-tracing approach that, while not exact in terms of the wave propagation, was relatively simple and very fast compared to computationally intensive finite element approaches. Experiments were performed to verify the modeling approach, and the majority of the data fell within the $\pm 2\sigma$ bounds for crack depths as defined by the statistics of the measurement model. Thus, this model serves as a reasonable method for relating the ultrasonic waveforms to crack dimensions.

While the measurement model provides the capability to size fatigue cracks directly from the ultrasonic waveforms, more accurate size estimates can be achieved by incorporating the physics of crack growth. A sizing methodology was created that combines the measurement model with a classical crack growth relationship. The sizing methodology employs a state estimation approach, specifically an extended Kalman filter, in order to approximate the optimal solution given the noises associated with the measurement response and the variations in the crack growth process. Care must be taken to ensure that the crack growth and measurement models accurately represent the target application. It was found that the state estimation approach to crack sizing gives a better estimate of experimental crack profiles when compared to the purely measurement-based approach of the measurement model. The implication is that by combining the mechanisms for the progression of damage with the ultrasonic measurements, more accurate estimates of the degree of damage can be achieved.

The two main distinguishing characteristics of SHM as compared to nondestructive

evaluation (NDE) are the availability of time history data and the inability to move sensors. Optimization of any SHM method should incorporate both of these characteristics from the outset, as is done in the work reported here, rather than treating each data point as an individual inspection result. Explicitly incorporating damage growth mechanisms is one fundamental way of ensuring that time history data are analyzed in a way that produces results consistent with known patterns of damage progression. This approach moves the field of SHM away from the mentality of single measurements and toward its inclusion as an integral part of an overall life prediction/prognosis strategy.

9.2 Recommendations for Future Work

Several assumptions were made during the development of the SHM framework to simplify the development process and facilitate a proof-of-concept demonstration. This section summarizes recommendations for future work to bring the SHM methodology presented here closer to implementation on an aircraft.

9.2.1 Crack Growth Assumptions

During the creation of the system model based on crack growth equations, assumptions were made *a priori* regarding the likely shape of the crack emanating from the fastener hole surface. This shape effect was captured by the geometry correction factor, where the value was selected based on the experimental results. A more robust procedure for estimating the crack shape may be possible using the ultrasonic measurements, allowing the value to be determined for each experiment. A related approach for online parameter estimation was given by Orchard [82], where he used a state estimation approach to estimate the remaining structural life of a component and an outer loop to correct this estimate by modifying the model parameters. Application of this approach could result in an improvement in the overall estimation of the presented methodology, particularly the life prediction estimates where the measurements do not come into play.

9.2.2 Fastener Effects

Although results shown here are for open holes, the eventual application is for built up structures with fasteners, which could adversely affect performance of the algorithm in several ways. A fastener with an interference fit would tend to keep cracks open when loads are removed, particularly through-thickness cracks. Cracks could still be detected because of the resulting overall loss of energy, but they would most likely be much larger than those detected by a drop in the normalized energy ratio. A fastener could also affect detection of cracks by causing variable contact between the fastener and the inside diameter of the hole, resulting in both random variations of the normalized energy ratio curve and reduced energy loss with load because of waves propagating through the fastener. The presence of a built-up structure could have a similar effect where variable back surface contact could result in both received signal variations and leakage of energy into the material being fastened. Regardless of the specific fastener type and built-up geometry, the expected net effect is a reduction in detection sensitivity when fasteners are installed.

Also, during the development of the measurement model and crack growth relationship, it was assumed that the fastener hole geometry was a simple through-thickness hole with no counterbore-countersink. The primary concern with the counterbore-countersink geometry relates to the wave propagation around the surface of the fastener hole. Specifically, the presented methodology is easily adaptable to damage detection and tracking below the counterbore-countersink, but damage originating within counterbore-countersink geometry could be more difficult to detect. Further, the crack initiation would likely occur near the counterbore-countersink, reducing the effectiveness of the SHM framework presented. Possible approaches to these issues include,

1. Adjusting the receiver position to preferentially monitor the region of the fastener directly below the counterbore-countersink,

2. Modifying the measurement model to take into account the fixed effects of the counterbore-countersink geometry on the wave propagation, and

3. Modeling the fastener as a random damping of the ultrasonic energy for the measurement model.

9.2.3 Application to Additional Data

The SHM framework presented in this thesis should be verified using additional experimental data. During the development of the SIPS procedures, extensive fatigue testing was performed using a variety of fastener hole and transducer configurations. However, only a subset of these experiments were used in the development of the thesis. The detection strategy described here was applied and shown to be successful at detecting fatigue cracks on built-up wing panel structures with fasteners installed. The state estimation framework presented here could be extended to include this additional data by developing new measurement and system models appropriate for the built-up geometry.

9.2.4 Measurement Model Approximations

Crack estimates from the measurement model were acceptable for the SHM framework, but there were non-trivial errors in the final crack size estimates. The likely causes for differences between the modeled and measured crack sizes are transducer positioning errors and overly simplified wave propagation assumptions. Specifically, it was assumed that the transducers were mounted such that the energy is equally divided between the two sides of the hole. In practice, the mounting is never perfect and one side of the hole will have a higher relative energy compared to the other. Also, a more complicated derivation for a Rayleigh-like wave on a cylindrical surface was presented by Viktorov [68], where only the change in wavespeed was included here. The full derivation would result in a slight shift in the energy density away from the hole surface. Solutions to these two issues could be to statistically capture the effect of variable transducer locations by weighting one side

of the hole over the other during the energy ratio calculation, and implementing the full cylindrical wave solution presented by Viktorov to capture the reduced energy decay with depth.

9.2.5 Alternate Transducers

During the development of this framework on the SIPS program, an additional receive transducer was designed and compared to the ones described in Chapter 3. Specifically, the new transducer has dual elements side-by-side, which allows for each side of the hole to be monitored individually. The simultaneous monitoring of both sides of the hole provides the ability to not only detect the presence of cracking, but also to independently monitor each side of the hole. This configuration may also have the potential to detect larger defects; once the defects saturate the standard through-transmission monitoring, the pulse-echo signals from each transducer element of the receiver could be used to track the crack growth. This transducer configuration could readily be integrated into the SHM framework shown here, where instead of a single energy ratio curve for tracking, one is available for each side of the hole.

9.2.6 Analysis of Experimental Noise

The probability of detection curves generated in Chapter 6 assumed no experimental noise related to the fatigue process. The exclusion of this noise was necessary to decouple the noise related to uncertainty in the crack profile from the noise experienced during the fatiguing process. This decoupling allowed the measurement noise to be adaptively updated during real-time state estimation. A thorough analysis of the fatigue process noise would be valuable for improving the accuracy of the probability of detection curves by incorporating this noise. Also, false alarm rates could be estimated, which was not done for the work shown here.

9.2.7 Prognosis

Prognosis, or prediction of remaining life, as described in Chapters 7 and 8, was based on the assumption that the most recent crack size estimate from the extended Kalman filter was the correct value. This crack size was used as the starting point for the prognosis estimate, where a distribution of possible crack growth curves was created starting at this single value. A more realistic methodology would be to generate a distribution of initial points based on the state estimation output and the confidence of this estimate. Also, different distributions than a Gaussian, such as the Weibull distribution, should be considered for fitting the prognosis estimates.

APPENDIX A

PUBLICATIONS

A.1 Completed Works

A.1.1 Journal Articles

1. A. C. Cobb, J. E. Michaels and T. E. Michaels, "An Automated Time-Frequency Approach for Ultrasonic Monitoring of Fastener Hole Cracks," NDT&E International, Vol. 40, pp. 525-536, 2007.

A.1.2 Conference Proceedings

1. J. E. Michaels, A. C. Cobb and T. E. Michaels, "A Comparison of Feature-Based Classifiers for Ultrasonic Structural Health Monitoring," Proceedings of SPIE, *Health Monitoring and Smart Nondestructive Evaluation of Structural and Biological System III*, Vol. 5394, T. Kundu (Ed.), SPIE, pp. 363-374, 2004.

2. J. E. Michaels, T. E. Michaels, B. Mi, A. C. Cobb and D. M. Stobbe, "Self-Calibrating Ultrasonic Methods for In Situ Monitoring of Fatigue Crack Progression," *Review of Progress in Quantitative Nondestructive Evaluation*, Vol 24B, D.O. Thompson and D.E. Chimenti (Eds.), American Institute of Physics, pp. 1765-1772, 2005.

3. A. C. Cobb, J. E. Michaels, B. Mi and T. E. Michaels, "Ultrasonic Monitoring of Fastener Holes Using Load Modulated Energy Algorithms for Early Detection of Fatigue Cracks," *Review of Progress in Quantitative Nondestructive Evaluation*, Vol 25B, D.O. Thompson and D.E. Chimenti (Eds.), American Institute of Physics, pp. 1664-1671, 2006.

4. J. E. Michaels, T. E. Michaels, A. C. Cobb and G. J. Kacprzynski, "Ultrasonic Sensing and Life Prediction for the DARPA Structural Integrity Prognosis System," *Review of Progress in Quantitative Nondestructive Evaluation*, Vol. 26B, D. O. Thompson and D. E. Chimenti (Eds.), American Institute of Physics, pp. 1453-1460, 2007.

5. A. C. Cobb, J. E. Michaels and T. E. Michaels, "The Effect of Transducer Placement on the Monitoring of Fatigue Cracks Emanating from Fastener Holes," *Review of Progress in Quantitative Nondestructive Evaluation*, Vol. 26B, D. O. Thompson and D. E. Chimenti (Eds.), American Institute of Physics, pp. 1516-1523, 2007.

6. J. E. Michaels, T. E. Michaels and A. C. Cobb, "Ultrasonic monitoring of structural 'hot spots' during full scale fatigue tests," *Proceedings of the 6th International Workshop on Structural Health Monitoring*, F.-K. Chang (Ed.), DEStech Publications, Inc., Lancaster, PA, pp. 1576-1583, 2007.

7. A. C. Cobb, J. E. Michaels and T. E. Michaels, "A Bayesian Approach for Estimating Sizes of Fatigue Cracks near Fastener Holes," *Review of Progress in Quantitative Nondestructive Evaluation*, Vol. 27, Presented July 2007, Golden, Colorado, Proceedings in press.

A.2 Work in Process

A.2.1 Journal Articles

1. A. C. Cobb, J. E. Michaels, T. E. Michaels and P. Haldipur, "A Model-Assisted and Probabilistic Approach for In Situ Ultrasonic Measurement of Fastener Hole Fatigue Cracks," Paper Submitted to IEEE Transactions on Instrumentation and Measurement, February 2008.

A.2.2 Conference Proceedings

1. A. C. Cobb, J. E. Michaels and T. E. Michaels, "Experimental verification of a Kalman Filter approach for estimating the size of fastener hole fatigue cracks," SPIE Smart Structures and Materials + Nondestructive Evaluation and Health Monitoring, March 2008.

REFERENCES

[1] J. Achenbach and S. Kulkarni, "Structural health monitoring of fatigue damage," in *Proceedings of Structural Health Monitoring* (F.-K. Chang, ed.), pp. 427–435, DEStech, 2005.

[2] J. Papazian, R. Silberstein, G. Welsh, D. Grundy, C. Craven, L. Evans, N. Goldfine, J. Michaels, T. Michaels, Y. Li, and C. Laird, "Sensors for monitoring early stage fatigue cracking," *International Journal of Fatigue*, vol. 29, pp. 1668–1680, 2007.

[3] P. Paris and F. Erdogan, "A critical analysis of crack propagation laws," *Journal of Basic Engineering*, pp. 528–534, 1963.

[4] D. Balageas, C.-P. Fritzen, and A. Guemes, *Structural Health Monitoring*. ISTE Ltd, 2006.

[5] D. E. Adams, *Health Monitoring of Structural Materials and Components*. John Wiley & Sons Ltd, 2007.

[6] M. Derriso and S. Olson, "The future role of structural health monitoring applications," in *Proceedings of Structural Health Monitoring* (F.-K. Chang, ed.), pp. 17–25, DEStech, 2005.

[7] R. B. Thompson and D. O. Thompson, "Ultrasonics in nondestructive evaluation," *Proceedings of the IEEE*, vol. 73, no. 12, pp. 1716–1755, 1985.

[8] J. Krautkrämer and H. Krautkrämer, *Ultrasonic Testing of Materials*. Springer-Verlag, 2nd ed., 1975.

[9] J. L. Rose, "A baseline and vision of ultrasonic guided wave inspection potential," *Journal of Pressure Vessel Technology*, vol. 124, pp. 273–282, 2002.

[10] P. B. Nagy, M. Blodgett, and M. Golis, "Weep hole inspection by circumferential creeping waves," *NDT&E International*, vol. 27, no. 3, 1994.

[11] S. Baby, T. Balasubramanian, and R. Pardikar, "Ultrasonic sizing of embedded vertical cracks in ferritic steel welds," *Theoretical and Applied Fracture Mechanics*, vol. 40, pp. 145–151, 2003.

[12] C. Yew, K. Chen, and D. L. Wang, "An experimental study of interaction between surface waves and a surface breaking crack," *The Journal of the Acoustical Society of America*, vol. 75, pp. 189–196, 1984.

[13] Z. Yan and P. Nagy, "Thermo-optical modulation of ultrasonic surface waves for NDE," *Ultrasonics*, vol. 40, pp. 689–696, 2002.

[14] J.-Y. Kim and S. Rokhlin, "Surface acoustic wave measurements of small fatigue cracks initiated from a surface cavity," *Int. Journal of Solids and Structures*, vol. 39, pp. 1487–1504, 2002.

[15] J. Aldrin, J. Knopp, D. Judd, J. Mandeville, and E. Lindgren, "In-situ surface acoustic wave monitoring of fatigue crack initiation and propagation," in *Review of Progress in Quantitative Nondestructive Evaluation* (D. O. Thompson and D. E. Chimenti, eds.), vol. 18, pp. 2225–2233, Kluwer Academic and Plenum, 1999.

[16] K. Harri, P. Guillaume, and S. Vanlanduit, "On-line monitoring of cracks using ultrasonic 'multisine' surface waves," *Proceedings of ECNDT*, 2006.

[17] J. L. Rose and H. Schlemm, "Equivalent flaw size measurements and characterization analysis," *Materials Evaluation*, vol. 34, no. 1, pp. 1–8, 1976.

[18] K. Date, H. Shimada, and N. Ikenaga, "Crack height measurement - an evaluation of the accuracy of ultrasonic timing methods," *NDT International*, vol. 15, pp. 315–319, 1982.

[19] M. G. Silk, "The transfer of ultrasonic energy in the diffraction technique for crack sizing," *Ultrasonics*, vol. 17, pp. 113–120, 1979.

[20] J.-R. Lee and H. Tsuda, "Monitoring of crack at an open hole using built-in fibre wave piezoelectric transducers," *Measurement Science Technology*, vol. 17, pp. 2643–2649, 2006.

[21] J. Rose, P. Karpur, and V. Newhouse, "Utility of split-spectrum processing in ultrasonic nondestructive evaluation," *Materials Evaluation*, vol. 46, no. 1, pp. 114–122, 1988.

[22] J. Aussel, "Split spectrum processing with finite impulse response filters of constant frequency-to-bandwidth ratio," *Ultrasonics*, vol. 28, pp. 165–177, 1990.

[23] P. Karpur and M. T. Resch, "Improved detectability of fatigue microcracks by split spectrum processing of backscattered Rayleigh waves," in *Review of Progress in Quantitative Nondestructive Evaluation* (D. O. Thompson and D. E. Chimenti, eds.), vol. 10A, (New York), pp. 757–764, Plenum Press, 1991.

[24] X. Li, N. Bilgutay, and R. Murthy, "Spectral histogram using the minimization algorithm - Theory and applications to flaw detection," in *IEEE Transactions on Ultrasonics, Ferroelectronics, and Frequency Control*, vol. 39, pp. 279–284, 1992.

[25] C. Cudel, M. Grevillot, J. Myer, L. Simonin, and S. Jacquey, "Detecting echoes of different spectral characteristics in absorbing media by variable moving bandwidth SSP minimization," *Ultrasonics Symposium*, vol. 1, pp. 785–788, 2002.

[26] M. Grevillot, C. Cudel, J. Myer, and S. Jacquey, "Two approaches to multiple specular echo detection using split spectrum processing: moving bandwidth minimization and mathematical morphology," *Ultrasonics Symposium*, vol. 37, no. 6, pp. 417–422, 1999.

[27] P. Rizzo and F. D. Scalea, "Ultrasonic inspection of multi-wire steel strands with the aid of the wavelet transform," *Smart Materials and Structures*, vol. 14, no. 4, pp. 685–695, 2005.

[28] R. Murthy, N. Bilgutay, and K. Kaya, "Detection of ultrasonic anomaly signals using wavelet decomposition," *Materials Evaluation*, vol. 55, no. 11, pp. 1274–1279, 1997.

[29] E. Oruklu and J. Saniie, "Ultrasonic flaw detection using discrete wavelet transform for NDE applications," *IEEE Symposium*, vol. 2, pp. 1054– 1057, 2004.

[30] F. Bettayeb, S. Haciane, and S. Aoudia, "Improving the time resolution and signal noise ratio of ultrasonic testing of welds by the wavelet packet," *NDT&E International*, vol. 38, no. 6, pp. 478–484, 2005.

[31] M. Hayes, *Statistical Digital Signal Processing and Modeling*. John Wiley and Sons, Inc., 7th ed., 1996.

[32] J. P. Lynch, "Detection of structural cracks using piezoelectric active sensors," in *Proceedings of the ASCE Engineering Mechanics Conference (EM2004)*, 2004.

[33] Y. Lu and J. E. Michaels, "Discriminating damage from surface variations via feature analysis for ultrasonic structural health monitoring systems," in *Review of Progress in Quantitative Nondestructive Evaluation*, vol. 27.

[34] J. E. Michaels, A. C. Cobb, and T. E. Michaels, "A comparison of feature-based classifiers for ultrasonic structural health monitoring," in *Proceedings of SPIE, Health Monitoring and Smart Nondestructive Evaluation of Structural and Biological Systems III* (T. Kundu, ed.), vol. 5394, pp. 363–374, SPIE-The International Society for Optical Engineering, 2004.

[35] H. Hagiwara and A. Mita, "Local damage assessment of a building using support vector machine," in *Earthquake Resistant Engineering Structures IV*, pp. 235–244, 2003.

[36] K. Worden and A. Lane, "Damage identification using support vector machines," in *Smart Materials and Structures*, vol. 10, pp. 540–547, Institute of Physics Publishing, 2001.

[37] K.-R. Muller, S. Mika, G. Ratsch, K. Tsuda, and B. Scholkopf, "An introduction to kernel-based learning algorithms," *IEEE Transactions on Neural Networks*, vol. 12, no. 2, pp. 181–201, 2001.

[38] T. J. Case and R. C. Waag, "Flaw identification from time and frequency features of ultrasonic waveforms," *IEEE Transactions on Ultrasonics, Ferroelectronics, and Frequency Control*, vol. 43, no. 4, pp. 592–600, 1996.

[39] P. Hoffman and J. Hurtado, "Airframe integrity based on bayesian approach," in *International Committee on Aircraft Fatigue*, 2005.

[40] X. Wang, M. Modarres, and P. Hoffman, "Probabilistic-based P-3 airframe integrity management," in *Aging Aircraft Conference*, 2007.

[41] F. Grooteman, "A stochastic approach to determine lifetimes and inspection schemes for aircraft components," *International Journal of Fatigue*, vol. 30, pp. 138–149, 2008.

[42] N. E. Dowling, *Mechanical Behavior of Materials*. New Jersey: Prentice-Hall, Inc., tenth ed., 1993.

[43] B. Mi, J. E. Michaels, and T. E. Michaels, "An ultrasonic method for dynamic monitoring of fatigue crack initiation and growth," *Journal of the Acoustical Society of America*, vol. 119, no. 1, pp. 74–85, 2006.

[44] D. Stobbe, "Acoustoelasticity in 7075-T651 aluminum and dependence of third order elastic constants on fatigue damage," Master's thesis, Georgia Institute of Technology, Atlanta, GA.

[45] "http://www.engineersedge.com/aluminum_tempers.htm/," February 2008. Aluminum Temper Descriptions.

[46] "http://www.mts.com/," February 2008. MTS System Corporation.

[47] J. E. Michaels, T. E. Michaels, and B. Mi, "An ultrasonic angle beam method for in situ sizing of fastener hole cracks," *Journal of Nondestructive Evaluation*, vol. 25, no. 1, pp. 3–16, 2006.

[48] J. E. Michaels, T. E. Michaels, B. Mi, A. C. Cobb, and D. M. Stobbe, "Self-calibrating ultrasonic methods for in-situ monitoring of fatigue crack progression," in *Review of Progress in Quantitative Nondestructive Evaluation* (D. O. Thompson and D. E. Chimenti, eds.), vol. 24B, (New York), pp. 1765–1772, American Institute of Physics, 2005.

[49] J. E. Michaels, T. E. Michaels, A. C. Cobb, and G. J. Kacprzynski, "Ultrasonic sensing and life prediction for the DARPA structural integrity prognosis system," in *Review of Progress in Quantitative Nondestructive Evaluation* (D. O. Thompson and D. E. Chimenti, eds.), vol. 26B, (New York), pp. 1453–1460, American Institute of Physics, 2006.

[50] "http://www.activewireinc.com/," February 2008. ActiveWire, Inc.

[51] M. G. Silk, "Determination of crack penetration using ultrasonic surface waves," *NDT International*, vol. 9, no. 6, pp. 290–297, 1976.

[52] J. David and N. Cheeke, *Fundamentals and Applications of Ultrasonic Waves*. Boca Rato, Florida: CRC Press, 2002.

[53] J. L. Rose, *Ultrasonic Waves in Solid Media*. Cambridge University Press, 1999.

[54] R. Polikar, L. Udpa, S. Udpa, and T. Taylor, "Frequency invariant classifcication of ultrasonic weld inspection signals," *IEEE Transactions on Ultrasonics, Ferroelectronics, and Frequency Control*, vol. 45, no. 3, pp. 614–625, 1998.

[55] J. Michaels, A. Cobb, and T. Michaels, "A comparison of feature-based classifiers for ultrasonic structural health monitoring," in *Proceedings of SPIE, Health Monitoring and Smart Nondestructive Evaluation of Structural and Biological Systems III* (T. Kundu, ed.), vol. 5294, pp. 363–374, American Institute of Physics, 2004.

[56] J. Aldrin, J. Knopp, D. Judd, J. Mandeville, and E. Lindgren, "Spiral creeping waves in ultrasonic angled-beam shear wave inspection of fastener holes in multilayer structures," in *Review of Progress in Quantitative Nondestructive Evaluation* (D. O. Thompson and D. E. Chimenti, eds.), vol. 25A, pp. 187–194, American Institute of Physics, 2005.

[57] T. K. Moon and W. C. Stirling, *Mathematical Methods and Algorithms for Signal Processing*. Pearson Education, 1st ed., 2000.

[58] S. Julier and J. Uhlmann, "A new extension of the Kalman filter to nonlinear systems," in *Proceedings of SPIE, Signal Processing, Sensor Fusion, and Target Recognition VI* (I. Kadar, ed.), vol. 3068, pp. 182–193, 1997.

[59] C. K. Wikle and L. M. Berliner, "A Bayesian tutorial for data assimilation," *Physica D*, vol. 230, pp. 1–16, 2007.

[60] M. Arulampalam, S. Maskell, N. Gordon, and T. Clapp, "A tutorial on particle filters for online nonlinear/non-Gaussian Bayesian tracking," *IEEE Transactions on Signal Processing*, vol. 50, no. 2, pp. 174–188, 2002.

[61] B. Masserey and E. Mazza, "Ultrasonic sizing of short surface cracks," *Ultrasonics*, vol. 46, pp. 195–204, 2007.

[62] J. Sargent, "Ultrasonic imaging of cracks around fastener holes," *Insight*, vol. 39, no. 11, pp. 790–794, 1997.

[63] J.-B. Ihn and F.-K. Chang, "Detection and monitoring of hidden fatigue crack growth using built-in piezoelectric sensor/acuator network: II. Validation using riveted joints and repair patches," *Smart* M*aterials and* S*tructures*, vol. 13, pp. 621–630, 2004.

[64] R. Clark, W. Dover, and L. Bond, "The effect of crack closure on the reliability of NDT predictions of crack size," *NDT International*, vol. 20, pp. 269–275, 1987.

[65] D. K. Rehbein, R. B. Thompson, and O. Buck, "Ultrasonic size determination of cracks with large closure regions," in *Special Applications and Advanced Techniques for Crack Size Determination* (J. J. Ruschau and J. K. Donald, eds.), (Philadelphia), pp. 104–113, ASTM, 1995.

[66] S. R. Ahmed and M. Saka, "A new ultrasonic angle-beam technique for sensitive evaluation of closed cracks," *NDT&E International*, vol. 33, pp. 261–271, 2000.

[67] D. A. Cook and Y. H. Berthelot, "Detection of small surface breaking fatigue cracks in steel using scattering of Rayleigh waves," *NDT&E International*, vol. 34, pp. 483–492, 2001.

[68] I. Viktorov, *Rayleigh and Lamb Waves*. New York: Plenum Press, 1967.

[69] J. D. Achenbach, *Wave Propagation in Elastic Solids*. Amsterdam: Elsevier Science Publishers, 8th ed., 1999.

[70] D. Hughes and J. Kelly, "Second-order elastic deformation of solids," *Physical Review*, vol. 92, no. 1, pp. 1145–1149, 1953.

[71] D. D. Muir, J. E. Michaels, and T. E. Michaels, "An ultrasonic angle beam method for determining third order elastic constants via acoustoelasticity measurements," in *Review of Progress in Quantitative Nondestructive Evaluation* (D. O. Thompson and D. E. Chimenti, eds.), (New York), American Institute of Physics, 2007.

[72] A. C. Cobb, J. E. Michaels, and T. E. Michaels, "A Bayesian approach for estimating sizes of fatigue cracks near fastener holes," in *Review of Progress in Quantitative Nondestructive Evaluation* (D. O. Thompson and D. E. Chimenti, eds.), (New York), American Institute of Physics, 2007.

[73] J. Newman, "Fastran II - A fatigue crack growth structural analysis program.," *NASA Technical Memorandum*, no. 104159, 1992.

[74] "http://www.kuleuven.ac.be/bwk/materials/teaching/," April 2007. Fracture Mechanics Lecture Notes.

[75] Y. Murakami, ed., *Stress Intensity Factors Handbook*. Oxford, UK: Pergamon Press, 1987.

[76] R. Patankar, A. Ray, and A. Lakhtakia, "A state-space model of fatigue crack growth," *Internation Journal of Fracture*, no. 90, pp. 235–249, 1998.

[77] J. Newman, A. Brot, and C. Matias, "Crack growth calculations in 7075-t7351 alloy under various load spectra using an improved crack-closure model," *Engineering Fracture Mechanics*, no. 71, pp. 2347–2363, 2004.

[78] C. Glancey and R. Stephens, "Fatigue crack growth and life predictions under variable amplitude loading for a cast and wrought aluminum alloy," *Internation Journal of Fatigue*, no. 28, pp. 53–60, 2006.

[79] R. C. Shah, "Stress intensity factors for through and part-through cracks originating at fastener holes," in *Mechanics of crack growth, ASTM STP 590*, pp. 429–459, ASTM, Philadelphia, 1976.

[80] P. Lucáš, "Stress intensity factor for small notch-emanated cracks," *Engineering Fracture Mechanics*, vol. 26, no. 3, pp. 471–473, 1987.

[81] A. Ray and R. Patankar, "A stochastic model of fatigue crack propagation under variable-amplitude loading," *Engineering Fracture Mechanics*, vol. 62, pp. 477–493, 1999.

[82] M. E. Orchard, *A Particle Filter-Based Framework for On-line Fault Diagnosis and Failure Prognosis*. PhD thesis, Georgia Institue of Technology, November 2007.